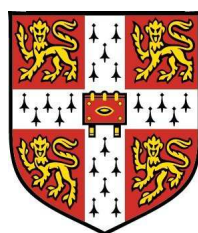# Syngas Production from Heavy Liquid Fuel Reforming in Inert Porous Media

Cambridge University

Department of Engineering

This dissertation is submitted for the degree of

Doctor of Philosophy by:

Andrea Pastore

Fitzwilliam College

1st of July, 2010

Declaration

This dissertation is the result of my own work and includes nothing which is the outcome of work done in collaboration except where specifically indicated in the text. The dissertation contains approximately 35,000 words, 70 figures and three tables.

Andrea Pastore

Hopkinson Laboratory, Cambridge

July, 2010

I would like to dedicate this thesis to my family, to my girlfriend and to all my friends.

Acknowledgements

Firstly, I would like to thank my supervisor Prof. Epaminondas Mastorakos for his support, invaluable help, trust and efforts to obtain funding for my research and staying in Cambridge. I would also like to thank my advisor Dr. Scott for helping with his valuable advice and support on the experimental aspects of my project. A special thank also to Dr. Balachandran for his support before the beginning of this PhD and to Voller Energy plc for the financial sustainment during these 3 years. I am also very grateful to the gentlemen of the workshop: Michael, Robert, Peter, Sam, Ken and John for the excellent job and suggestions for my experimental rig. I also want to thank all the colleagues and friends I met in the Engineering Department who supported me during these years: Moncef, Christos, Antonios, Andy, Giorgio, Teresa, Alex, Giulio, Davide, Cheng, Camille, Rob, Teresa, Frank, Sam, Simon, Thibault, Ronan, Johannes, Simon, Marta, Larry, Chris, Jason, James, Christoph and Robin. I want to acknowledge the invaluable moral support from Udine, from my family and my old friends. I would also like to express my gratitude to the Cambridge Volleyball Club, which allowed me to spend some very exciting and sportful time during my staying in Cambridge. Finally, a very special thank to my Bettina, who made my last year in Cambridge so fantastic and special.

Abstract

In the effort to introduce fuel cell technology in the field of decentral-
ized and mobile power generators, a hydrocarbon reformer to syngas
seems to be the way for the market uptake. In this thesis, a po-
tential technology is developed and investigated, in order to convert
commercial liquid fuel (diesel, kerosene and biodiesel) to syngas. The
fundamental concept is to oxidise the fuel in a oxygen depleted envi-
ronment, obtaining hydrogen and carbon monoxide as main products
of the reaction. In order to extend the flammability limit of hydro-
carbon/air mixtures, the rich combustion experiments have been car-
ried out in a two-layer porous medium combustor, which stabilises a
flame at the matrix interface and recirculates the enthalpy of the hot
products in order to enhance the reaction rates at ultra-rich equiva-
lence ratio. This thesis demonstrates the feasibility of the concept, by
exploring characteristic parameters for a compact, reliable and cost
effective device.

Specifically, a range of equivalence ratios, thermal loads and porous
materials have been examined. n-heptane was successfully reformed
up to an equivalence ratio of 3, reaching a conversion efficiency (based
on the lower heating value of H_2 and CO over the fuel input) up to
75% for a packed bed of alumina beads. Thermal loads from P=2
to 12 kW at φ=2.0 demonstrated that heat losses can be reduced to
10%.

Similarly, diesel, kerosene and bio-diesel were reformed to syngas in
a Zirconia foam burner with conversion efficiency over 60%. The
effect of different burners, thermal loads and equivalence ratios have

also been assessed for these commercial fuels, leading to equivalent conclusions.

A preliminary attempt to reduce the content of CO and hydrocarbons in the reformate has been also performed using commercial steam reforming and water-gas shift reaction catalysts, obtaining encouraging results. Finally, soot emission has been assessed, demonstrating particle formation for all the fuels above φ=2.0, with biodiesel showing the lowest soot formation tendency among all the fuels tested.

List of Publications

Two journal papers and two conference papers have been published about the results described in this thesis:

- A. Pastore and E. Mastorakos. "Rich n-heptane and Diesel Combustion in Porous Media", *Experimental Thermal and Fluid Science*, 34:359-365, 2010.

- A. Pastore and E. Mastorakos. "Syngas Production from Liquid Fuels in a Non-Catalytic Porous Burner", *Fuel*, Article in Press, 2010.

- A. Pastore and E. Mastorakos. "Syngas Production from Diesel Non-Catalytic Partial Oxidation in Inert Porous Media", Proceedings of the 4th International Conference on Application of Porous Media, Istanbul, 2009.

- A. Pastore and E. Mastorakos. "Non-Catalytic Multi-Fuel Reformer for Syngas Production for Fuel Cell Applications", AiChE Spring Meeting, San Antonio, 2010.

Contents

List of Tables

List of Figures

Chapter 1

Introduction

1.1 Background and Motivation

Energy consumption has dramatically increased during the last 30 years, by almost doubling the energy demand estimated in million tonnes of oil equivalent [11]. The electricity generation and the transportation system are mainly based on the combustion of fossil fuels, generally defined as oil, coal and natural gas, as shown in Fig. 1.1.

There are several issues to be considered about fossil fuel consumption. First of all, the greenhouse gas emission, due to hydrocarbon combustion, has obviously followed the rising trend of fossil fuel utilization since the current energy infrastructure is considered as the main source of anthropogenic emissions. It is clear that CO_2 is the main pollutant, being one of the main products, together with water, in complete combustion processes. The concentration of carbon dioxide present in the environment is regulated by the carbon flow, which is constituted by the flux from the atmosphere to the land and oceans through natural processes such as plant photosynthesis. Unfortunately, this process can absorb only partially the CO_2 emitted by human activities: of the 6.1 billion metric tons of carbon monoxide absorbed per year, 3.2 billion metric tons are added annually unbalancing the absorption/emission ratio [11]. Secondly, oil, coal and natural gas are not renewable resources and, even though new extraction sites are often discovered, an alternative solution has to be found [12]. Numerous alternative fu-

Figure 1.1: U.S. Primary Energy Flow by Source and Sector [1].

els have been investigated, such as biodiesel, methanol, ethanol, hydrogen, boron, liquefied petroleum gas (LPG), Fischer-Tropsch fuel and solar fuels.

One of these is hydrogen, the most abundant of the chemical elements, constituting roughly 75% of the universe's elemental mass. Unfortunately, elemental hydrogen is relatively rare on Earth, but it may be produced by using the process of water electrolysis or by hydrocarbon reforming. In this sense, hydrogen cannot be defined as a fuel, but it is an energy carrier, because it must be produced from other naturally occurring species at significant cost in energy. The first process seems to be the most promising for a clean environment solution, through the utilization of nuclear, solar power or other renewable sources to provide the energy needed in water bond separation. Nowadays, water electrolysis is limited by the cost and the emissions involved in upstream electricity generation. The second option might be an intermediate step, characterised by centralised hydrogen generation with carbon capture and storage (CCS) [13]. If the Fuel Cell Vehicle (FCV) system uses the H_2 produced by this process, the CO_2 emission in the transportation field could be decreased to 70-80% of the traditional CO_2 emission from the gasoline- or diesel-based IC engine vehicle systems [14]. Both

possibilities, resulting in hydrogen production and its subsequent utilization in energy applications, result in reducing drastically the carbon footprint of the processes. Hydrogen might be used for power generation or as a transport fuel, for example in association with fuel cells. As an energy carrier, it could be also a suitable substitute for electricity; examples of H_2 as an alternative energy carrier from solar or nuclear plant are given by [15], by claiming, for instance, that in the case of fusion reactors of 30 GW or even 100 GW, hydrogen in pipelines is the most economically viable solution. Moreover, unlike electricity, hydrogen can be stored and accumulated.

In the future, hydrogen might also be used for power generation and in transport by fuelling gas turbines and IC engines, thanks to its high LHV (120.1 MJ/kg) and its high flammability (from 4% to 75% of volume in air). Moreover, it has a high flame speed (order of magnitude higher than gasoline), a high effective octane number, and no toxicity or ozone-forming potential [16]. The product of hydrogen combustion with air is water vapor and negligible pollution when the peak temperature is limited. Nevertheless, the heating value per unit volume is lower compared to hydrocarbons, because of the low density of H_2 (89.9×10^{-6} kg/m^3 STP). Another drawback linked with the low H_2 density is the movement: the power required to pump hydrogen is around 4.5 times higher than for natural gas per unit of delivered energy [17]. Hydrogen can be stored on-board a vehicle as a compressed gas, as a liquid in cryogenic containers, or as a gas bound with certain metals in metal hydrides. Liquid hydrogen is not a cheap solution, since the electricity required for hydrogen liquefaction at -253°C and 1 atm is about 35-43 MJ/kg H_2. Also refuelling stations are extremely expensive at the moment and decentralised hydrogen production, even if it is the best choice for the market uptake, is less efficient than large-scale centralised production and it makes CCS impractical [17]. However, the estimation of the energy supply and demand in 2030 calls for an investment which is comparable to the estimated cost of the power system replacement for the hydrogen production and distribution [17].

Currently, the cheapest and most popular sources of H_2 are natural gas reforming (48% of the total hydrogen produced) and coal gasification (18% of the total hydrogen produced) without CCS, and it is used primarily in the chemical and refinery industries [16; 17; 18]. Since hydrogen production from renewable

and nuclear energy needs more research and development, the hydrocarbon dependence will remain still predominant for a long period. In this context, this research focuses on the reforming of logistic heavy liquid fuel to syngas, in order to obtain hydrogen for a mobile power generator system, for example in an integrated fuel processor/fuel cell device.

One of the most promising hydrogen applications is the one connected to fuel cells [19; 20]. The major advantages of fuel cells can be summarized by the following characteristics [21]:

- High energy conversion efficiency;

- No emissions, or extremely low emissions of pollutants;

- Low noise pollution;

- Process simplicity for conversion of chemical to electrical energy.

The most attractive fuel cell feature is its independence from the intrinsic efficiency limitation of thermal processes recognised by Carnot [22] and the almost complete absence of emissions. Modern IGCC power stations operate at efficiencies of about 50% [23], limited by the top temperature of the cycle and the typical overall fuel efficiency of gasoline-powered cars is around 12% and 15% for diesel-powered cars [24]. Fuel cells are electrochemical devices and in theory, devices could be constructed with an efficiency of 80-90% [25]. It must be noted that higher energy efficiency itself leads to a reduction in emissions. The absence of mechanical steps also leads to other advantages such as the minimum requirement of rotating accessories pumps and motors demonstrating a low level of noise and vibrations.

1.2 Fuel reforming

1.2.1 Basic concepts

While waiting for the hydrogen economy led by water electrolysis through renewable energy sources - as the ultimate hydrogen economy prediction for the

long term - the transitional approach seems to be the reformation of the available hydrocarbon fuels to fuel cell quality hydrogen [26]. Distributed hydrogen production would be attractive in the early stages of a hydrogen economy. Thus, small-scale reformers are the key technology for this first step [27]. In November 2000, DaimlerChrysler unveiled the NECAR 5 prototype automobile, which utilizes methanol as a fuel with a fuel processor and a 75-kW fuel cell. Similarly, fuel cells coupled to fuel reformers can be convenient generators for residential homes, commercial buildings and building sites [2]. Nevertheless, the net efficiency of the fuel cell system is reduced by using fuel processing for hydrogen production in multiple stages (sulfur removal, fuel reforming, syngas clean-up), but it will still show a significant efficiency advantage [2].

Eventually, when fuel cells and hydrogen demand will build up, a switch can be made to central hydrogen production, by using fossil sources with CO_2 sequestration and finally by the use of low carbon primary sources. Since the infrastructure for producing and distributing fossil fuels is well established, the research and development to introduce fuel cell and hydrogen utilisation in the transport and residential power generation market is focused on this area [28]. This is the main reason driving the research described in this document, which describes the development and performance of a liquid fuel processor.

1.2.2   Small-scale reforming

An on-board/on-site fuel processor should meet the following requirements:

- Hydrogen production levels smaller than those in chemical plants;

- Severe constraints on size and weight;

- Ability to cycle through frequent start-ups and shutdowns;

- Hydrogen production rate should be responsive to changes in demand;

- Strict cost target.

The reformate from a fuel processor generally contains 40-80% H_2 in volume on a dry basis [26] depending on the reforming technique and fuel adopted. From
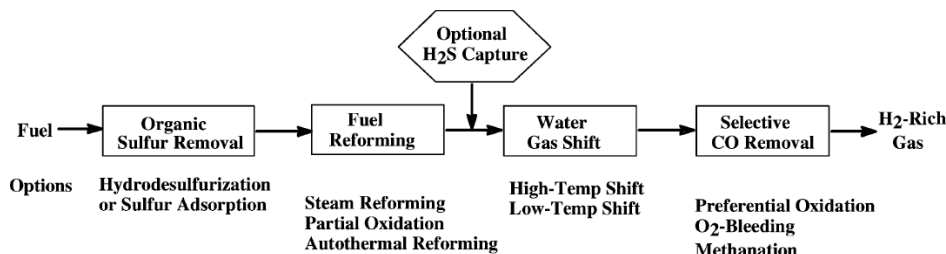
Figure 1.2: Steps in reforming process. Source [2].

the same reference, the authors underline that the fuel cell anode operates with 80-85% H_2 utilisation. They propose that the balance of the unconverted H_2 can be oxidized and its heat can be recovered. For example, they suggest that this recovered heat can be used to preheat the incoming water to produce steam or to preheat fuel and air prior to injection into the reactor. The main steps and options for on-site and on-board processing of liquid and gaseous hydrocarbons are shown in Fig. 1.2.

The potential candidates for on-site and on-board reforming are gasoline, diesel and jet fuels together with natural gas and carbon-neutral resources like bio-fuels, since they all have existing infrastructure of manufacturing and distribution. However, the problem associated with heavy fuel processing is mainly the low H/C ratio, high energy consumption in fuel evaporation, the high temperature at fuel reforming and the ease of carbon deposition and soot emission [29]. In the next sub-sections, the three main different fossil fuel reforming methods will be covered, namely, steam reforming, partial oxidation and autothermal reforming.

1.2.3   Steam reforming

Steam reforming (SR) is the most common technique to produce hydrogen in the chemical process industry. One of the earliest steam reforming processes was developed in Germany by IG Farbenindustrie in 1926 [30]. An example of an early commercial steam reformer is a laboratory-scale device from Johnson-Matthey, developed in the 1970s, which could produce high-purity hydrogen using a Pd diffuser to purify the product gas [31].

6

In catalytic steam reforming, the fuel reacts with steam in the presence of a catalyst, producing hydrogen and carbon monoxide. A global reaction can be written as:

$$C_mH_n + mH_2O = mCO + (n/2 + m)H_2 \qquad (1.1)$$
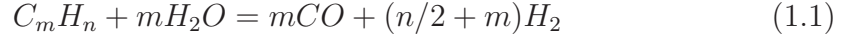
The steam reforming reaction is strongly endothermic and reactors are limited by heat transfer, rather than by reaction kinetics [32]. Therefore steam reactors are in general designed to promote heat exchange and hence they tend to be large and heavy, which is an acceptable drawback since the heat inertia of this system, rapid start and dynamic response are not usually part of the prerogatives of steam reforming. Size and weight are not desirable for a reformer involving transient duty cycles. Consequently, steam reformers are well suited for long periods of steady state operation, showing high concentration of hydrogen in the reformate. Another advantage for SR is that high pressure reformate can be generated by pumping liquid fuel and water without the need to compress air. Active catalysts should maximize hydrogen selectivity and inhibit coke formation as well as CO production [26]. The catalyst utilization in steam reforming is summarized by [33]. The authors report the wide use of nickel based catalysts, which are prone to coke formation and sulfur poisoning. The production of coke accelerates the degradation of the catalyst, until the catalyst is disintegrated and reforming becomes impossible. Similarly, it is reported that sulfur poisons nickel-based catalysts by forming metal sulfides and preventing reactants from adsorbing at the surface. Consequently, the alternative is the implementation of noble metal catalyst i.e. ruthenium, rhodium-based, which improves the tolerance to sulfur and limiting coke formation but also increases dramatically the cost of the reactor [34].

The steam to carbon ratio (S/C) plays an important role. Steam prevents solid carbon formation on the catalyst, it pushes the equilibrium towards the products, leading to a higher H_2 production and finally it acts as diluent reducing the local gradients in the reforming catalyst. However, high S/C ratios involve an increase in reactor size and the production and superheating of steam is at the expense of the fossil fuel to be reformed, lowering the global efficiency of the process [35].

As discussed previously, most of the hydrogen produced comes from natural gas steam reforming [17], but alcohol fuels are becoming an attractive alternative

because of the possible production of ethanol and methanol from biomass. Specifically, methanol steam reforming can be carried out at 250°C [36], whereas ethanol must be reformed above 300°C [37], by using the proper catalyst for each feedstock. Ethanol is the most attractive, since it is less toxic than methanol. However, even methanol steam reforming is tremendously attractive, as the increasing number of publications and extensive research demonstrate [38; 39; 40; 41] and [31]. The advantage of methanol SR over the other reforming techniques consists in the low CO production, a feature which cannot be translated to other hydrocarbon fuels. Compared to heavier fuels, methanol does not contain carbon to carbon bonds, it has a low boiling point (65°C), it has a high H/C ratio (4:1) and it can be converted to hydrogen at lower temperature than other fuels with the aid of a sufficiently active catalyst. Nevertheless, the main drawbacks of these two alcohol fuels are the low energy density (about half of the non-oxygenate hydrocarbons) and the lack of infrastructure for their distribution.

The definition of thermal efficiency for the steam reforming process is not trivial and it mainly depends on the heat source for driving the endothermic reaction. Specific choices must be taken: the heat can be provided by using supplemental fuel or recycled product gases. It seems quite clear that reformers do not complete the global reaction, but make some CO and CH_4 as products. Moreover, practical systems cannot separate all the H_2 from the reformate stream, so there is some residual that can be used as fuel. It makes sense to burn the reformate mixture instead of wasting its heating value, as experimentally demonstrated by [42]. Some examples of steam reformers coupled to fuel cells from the literature are shown in Table 1.1.

In conclusion, the challenges in steam reforming are mainly the design of the heat transfer system and, above all, the choice of the catalyst for the specific hydrocarbon to be reformed.

Table 1.1: Examples of steam reformers integrated with fuel cells.

Firing rate	Fuel	Efficiency [a]	Gas cleaning system	Fuel cell	Ref.
1 kW	NG, LPG	77% (full load)	PROX	2.5 kW PEMFC	[43]
2-8 kW	NG, LPG	67%	Pd membrane	5 kW PEMFC	[44]
-	FT diesel	58%	WGS and PSA	4 kW PEMFC	[45]
300 W	Methanol	56.7%	PROX	150 W PEMFC	[46]
-	NG	64.9%	Pd membrane	5 kW PEMFC	[47]

[a]based on H_2 LHV

1.2.4   Partial oxidation

Partial oxidation (POX) of hydrocarbons, characterised by a limited supply of oxidiser, is an exothermic reaction. Thus, compared to steam reformers, simpler reactors can be developed, since internal heat exchangers are not necessary. The first studies about partial oxidation started in 1946, where experiments were undertaken with Ni catalyst. The authors assumed a complete combustion of methane with oxygen and a subsequent reaction of CO_2 and H_2O with the unreacted methane yielding eventually syngas [48]. On the contrary, other authors [49] concluded that carbon monoxide and hydrogen are formed as primary reaction products. Another early significant work on partial oxidation is [50]. Working with reactors at high temperatures (750°C) and short residence time (0.1 s), a methane and oxygen conversion to syngas above 90% over precious metal catalyst was achieved. Hydrocarbon feedstocks are oxidized to produce hydrogen and carbon monoxide according to:

$$C_mH_n + (0.5)mO_2 = mCO + (0.5)nH_2 \qquad (1.2)$$
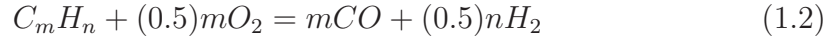
The main advantage of the partial oxidation technique is the small size of the reactor and the rapid response to changes. However, the main disadvantages lie with the low $H_2 : CO$ ratio and the danger of handling premixed air/fuel mixtures [34]. Moreover, if the fuel is oxidised by air, a high fraction of nitrogen dilutes the hydrogen content of the reformate. The partial oxidation reforming technique can be divided in two subcategories: CPOX (catalytic partial oxidation) and TPOX (thermal partial oxidation) since catalysts are not vital for POX, because of the high temperature involved. The partial oxidation reforming technique is the only one of the three that can be performed without the aid of a catalyst.

1.2.4.1   Catalytic POX

In the CPOX the hydrogen yield can be enhanced compared to the TPOX by using a properly designed catalyst [51]. Moreover, the use of catalyst offers the advantage of lower temperatures and no soot formation or unwanted by-products. Lower temperatures favour the water-gas shift reaction downstream the reforming process; it will mean also less fuel consumed during start-up and a wider choice

of reactor materials, which can lower the device cost. Higher temperatures require more thermal integration and more insulation adding to the size and costs. Catalytic partial oxidation is more difficult to control and the main issues include over-heating or hot spots due to the exothermic nature of the reactions and coking problem [2]. Gaseous fuels CPOX has been demonstrated by processing on a Rh catalyst n-butane at T=450°C [52], propane at T=700°C [53] and many works focused on methane reforming with this technique [54; 55; 56]. Catalytic partial oxidation of liquid higher hydrocarbons such as diesel and gasoline surrogates and desulfurized heavy liquid fuels has been demonstrated by [57; 58] and [59], suggesting that reforming into hydrogen will be possible in the future. The results and details from these papers are discussed and compared to this project in Section 4.5.

1.2.4.2   Thermal POX

TPOX shows more flexibility regarding the fuel to be reformed and more robust and cheaper reactors compared to CPOX. Thermal partial oxidation reformers are characterized by flame temperatures of about 1300-1500°C [2] but the optimal operating range for syngas production lies in the ultra-rich regime close to or beyond the conventional rich flammability limits. This limit has been overcome through several experimental works using filtration wave, parallel channel, spouted bed combustor and two-layer porous burner concepts [60; 61; 62; 63; 64; 65]. These non-catalytic reforming techniques enhance reaction rates by increasing reaction temperatures through internal heat transfer. Cool flame oxidation for heavy hydrocarbon breakdown techniques [27; 66] were used in fossil fuels partial oxidation reforming, especially for heavy liquid fuels such as diesel. In [65], the authors reformed methane/air mixtures with a proportion of fuel of 40% above the normal rich flammability limit, thanks to the heat recirculation due to the spouted bed. They also suggest the technique as a way to reform coal and heavy fuel oil. The parallel channel concept has been developed by Ellzey et al. [63], who successfully reformed propane/air mixtures in a meso-scale reformer. The reformer consists of parallel channels separated by conducting walls. By alternating the flow directions between adjacent channels, counter-flow heat exchange is

exploited to preheat the unreacted fuel/air mixture to a temperature level where a self-sustained reaction zone is viable. Nevertheless, all the works produced on hydrocarbon reforming to syngas in a non-catalytic partial oxidation reformer are on the development stage and at laboratory scale. Combustion in porous media will be discussed later in this Chapter, being one of the main features of this experimental work and specific details are given in Section 1.3.

1.2.5 Autothermal reforming

Also known as indirect partial oxidation or oxidative steam reforming, autothermal reforming (ATR) was firstly introduced by Haldor Topsoe in the late 1950s [67]. In essence, this process may be considered as a combination of partial oxidation and steam reforming:

$$C_mH_n + (0.5)mH_2O + 0.25mO_2 = mCO + (0.5m + 0.5n)H_2 \qquad (1.3)$$
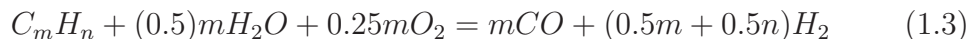
It involves the introduction of both air and steam into a reforming reactor: the partial oxidation occurs in an inlet zone of the reactor, providing heat for the steam reforming reaction occurring in a second zone of the vessel that is packed with catalyst. The catalyst controls the reaction pathways and determines the relative extents of the oxidation and steam reforming reactions. No external heating is required, since the exothermic oxidation reaction provides the heat necessary for the endothermic steam reforming reaction. ATR can overcome the load limitations of SR, because the oxidation process produces the heat required for the endothermic reactions, leading to a rapid response to power demand and faster start-up. The heat necessary to rapidly heat the reactor can be generated by operating at a higher than normal oxygen-fuel ratio. A practical example of an ATR processor is given by [68], describing a reactor capable of reforming gasoline to produce a stream containing 40% H_2 on a dry basis with an efficiency around 70% based on the lower heating value.

Thermodynamic calculations show that autothermal reforming theoretically yields higher reforming efficiencies than partial oxidation even at lower preheat temperatures [69]. Within an autothermal reformer heat can be integrated, for example, to vaporize the water and preheat the steam. In the case of partial

oxidation, this heat is waste energy and has to be removed by a cooling system. Intuitively, it results that the maximum theoretical efficiency is achieved at the thermoneutral point, where enough heat is provided to the steam reforming process to drive the reaction and no energy produced in the exothermic partial oxidation reaction is wasted [32]. The maximum achievable reforming efficiency is around 80% [69].

Three advantages are particularly important:

- Less complicated reactor design and lower reactor weights because of the less heat integration required;

- Wider choice of reactor materials;

- Lower fuel consumption during start-up.

An automotive application has been developed by a work sponsored by Renault and Nuvera Fuel Cells [70], showing hydrogen concentrations around 40% and CO level below 100 ppm using ethanol or gasoline as hydrocarbon feed stock. The reaction can in theory be completely balanced, but in practice a little excess of air is added to compensate the heat losses and to obtain a rapid response. The difference between the efficiency of the ATR and SR consists in the loss represented by the latent heat of vaporization of the water that escapes with the combustion products in the steam reforming system [32], when part of the fuel feed is used to combusted to generate heat for the reforming process. In autothermal reforming operations, the $H_2O/C_mH_nO_p$ and $O_2/C_mH_nO_p$ ratios play a fundamental role in thermal integration (global exothermicity or endothermicity), hydrogen and carbon monoxide yield, coke deposition and soot emission.

In recent years, ATR reformers gained interest as application for APU (auxiliary power unit) systems, in order to replace the idle functioning of IC engines with SOFC or PEMFC, due to stricter regulations, coupled with gasoline or diesel fuel processors [71; 72; 73; 74].

1.2.6 Comparison of the three techniques

Partial oxidation is much faster than any of the other two reactions - by roughly 2 orders of magnitude compared to steam reforming - and response time in fuel

supply is shorter [67]. This feature makes POX attractive for automotive applications. Moreover, it presents higher simplicity and scalability [32]. The main drawbacks of POX compared to steam reforming are the lower hydrogen yield and the dilution of the produced hydrogen by the inert nitrogen, which lowers the hydrogen concentration significantly when using air as the oxidiser. Catalytic steam reforming offers higher hydrogen concentrations: 70-80% hydrogen is achieved for steam reforming versus 40-50% for partial oxidation and autothermal reforming on a dry basis in the crude reformate gas [33], but it operates at high temperature and low space velocity owing to slow kinetics. Even though steam reforming yields more hydrogen than the other two techniques, POX results superior to the other systems in terms of the energy cost to produce the same amount of hydrogen [51]. The difference in hydrocarbon consumption among the three reforming systems depends strongly upon the efficiency of the heat exchanger [75]. Reforming through partial oxidation is less expensive than with steam reforming because of the compactness of the reactors, which do not need heat exchangers [76]. For practical applications, partial oxidation and autothermal reforming are more attractive because of their higher energy efficiency and small and light hardware compared to SR. Moreover, POX is the only of the three techniques that allows the reforming of fossil fuel in absence of catalyst. For this reason, the thermal POX technique has been chosen as the concept to design the liquid fuel reformer presented in this thesis.

1.2.7 Syngas clean-up and water-gas shift

Carbon monoxide must be kept under 10 ppm for the requirements of PEM fuel cell electrodes [2]. At low temperature CO can deactivate the anode catalyst made of Pt/C. This requirement is initially approached by using a water gas shift reaction (WGSR), a process discovered in 1780 by the physicist Felice Fontana [77]:

$$CO + H_2O \rightarrow CO_2 + H_2 \tag{1.4}$$

This reaction is exothermic and independent of pressure, thus it is thermodynamically favoured at low temperatures. For this reason, a general rule is that the higher the temperature is, the higher the carbon monoxide concentration will be.

In the shift reactor, the hydrogen yield is increased and the content of carbon monoxide in the reformed gas is reduced to 1-2% approximately with two different temperature stages (HT-WGSR and LT-WGSR) [2; 78]. The catalyst involved in driving the reaction must be carefully handled, regarding sulphur and oxygen content in the reactants, temperature, phyroporicity and hot spot, especially for exothermic processes (partial oxidation).

Other reactions can also be employed to further reduce the CO content in the feed:

- Preferential or selective oxidation (through a precious catalyst only CO is adsorbed and converted in CO_2 through a small amount of extra air - PROX) [79].

- CO methanation (it consists in the hydrogenation of CO using the H_2 already present in the gas stream) [80].

- Molecular oxygen bleeding (by injecting low amounts of O_2 into a H_2 anode feed stream contaminated by CO, the severe effects of carbon monoxide could be completely eliminated for fuel cells operating at 80°C) [81].

- Membranes (Palladium membrane allows only hydrogen to pass through its crystal lattice when it is heated above 300°C) [82].

1.3   Combustion in porous media

Combustion in porous media offers a way to establish non-catalytic POX and is discussed here, as it forms the topic of this thesis. In traditional combustion applications, the peak temperatures inside a combustion zone are directly related to the energy content of the unburned air/fuel mixture. The theoretical maximum temperature is predicted by the chemical equilibrium of an adiabatic process and is thus called the adiabatic equilibrium temperature. The insertion of a porous medium in the reaction zone allows the transfer of enthalpy from the burned gases to the unburned gases. The recirculation of the sensible enthalpy of the flame products occurs through convection from the hot gas to the inert matrix, which, in turn, transfers the heat through conduction and radiation to the matrix
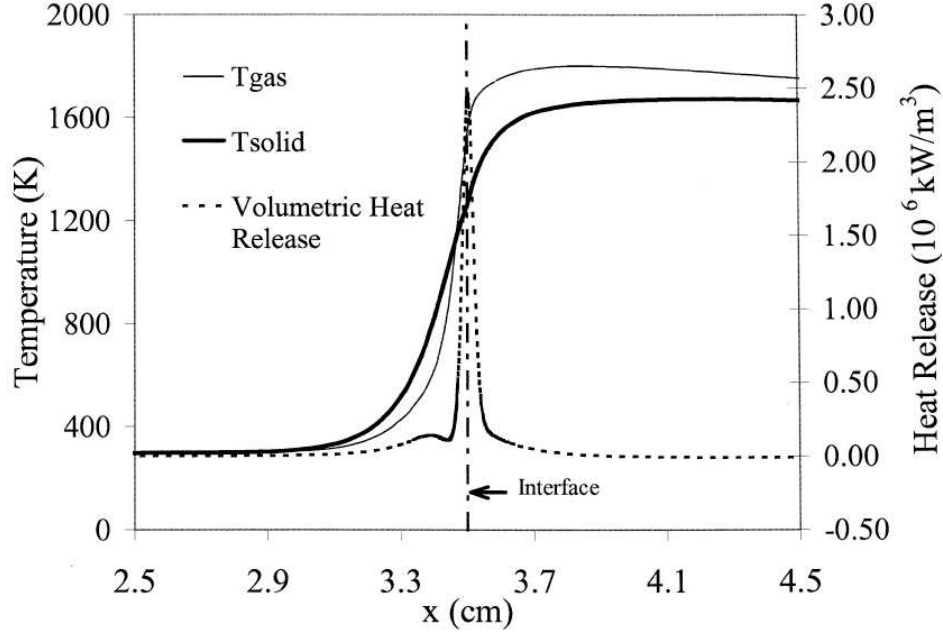
Figure 1.3: Solid and gas temperature and volumetric heat release for inlet gas velocity of 60 cm/s and φ=0.65. Source [3].

upstream of the flame, which then heats the incoming unburned mixture [83]. The higher thermal conductivity of the solid matrix compared to the conductivity of the gas enhances the effective heat transfer from the products to the reactants. Through this mechanism, it is possible to achieve a local temperature higher than the adiabatic flame temperature, while at the exit the temperature is limited by the first law of thermodynamics (Fig. 1.3). This mechanism leads to reaction zones effectively operating with substantial amounts of preheat, which results in faster kinetics and hence higher laminar flame speed (up to 20 times higher than a corresponding free flame [84]) and in the extension of the flammability limit of the mixture [85]. At ultra-rich or ultra-lean equivalence ratios the flame temperature is higher than in free flame conditions, which allows initiation and chain branching mechanisms to still occur. The superadiabatic effect in porous media has been observed in 1912 [86] and extensively studied by several authors [83; 87; 88; 89; 90].

1.3.1   Rich operation

The temperatures achieved in superadiabatic combustion and the fuel-rich conditions provide an environment necessary for thermal cracking and/or partial oxidation of various hydrocarbons. The extended rich flammability limit and the higher flame temperatures allow partial oxidation conditions to be established, thus allowing the stripping of the hydrogen out of the original fuel molecule. Consequently, the main products of the reactions are molecular hydrogen and carbon monoxide (syngas), along with nitrogen (since air provides the oxidiser) and some other species in lower concentration (carbon dioxide and light hydrocarbons). The main parameters affecting the oxidation behaviour are the thermal load, the equivalence ratio, the thermal conductivity of the porous matrix (material, porosity). Because of the heat recirculation, a balance must be achieved between heat feedback, heat release and heat losses, such that the effective flame speed equals the incoming fresh gas velocity. In this case a stationary flame can be developed. Otherwise, the reforming in porous media can assume an unsteady (filtration wave) condition. This operating mode has been experimentally demonstrated for gaseous [62], and liquid fuels [4] and the concept is to alternate the direction of the flame front by switching alternatively the reactant inlet with the product outlet. Depending on the gas flow velocity and the equivalence ratio, wave propagates either in the downstream direction producing super-adiabatic temperature or in the upstream direction (counter-flow) [91]. Babkin et al. classified the filtration wave mechanism in five regimes based on the wave velocity [92], showing that the low velocity regime (10^{-4} m/s) leads to strong thermal coupling between gaseous and solid phase. Filtration wave operation may have the disadvantage of a more complex fluid handling system, whereas stabilised flames, on the other hand, are easier to control and hence this latter option has been adopted in this research. A rich flame in porous media can be stabilised through different techniques [92; 93]:

- cooling of the porous matrix at the desired flame position;

- equalization of flame velocity with the flow speed with ad hoc reactor design;

- heat radiation from a specific position which lowers the flame speed;

- two-layer porous structure with a small pore region (flame holder) and a large pore region (reforming layer).

The last option has been chosen for this project because of the wider range of velocity and equivalence ratio flame conditions that can be stabilised compared to the other techniques. Flame propagation is possible only when the rate of heat release from the reaction is higher than the heat loss to the surroundings. For small pore structures, the flame propagation is limited to the upstream direction, because, for some conditions, the heat losses from the flame in the small-pores layer are higher than the heat released from the reaction. Moreover, the higher optical thickness limits the radiative heat transfer in the upstream direction. Therefore, the flame is quenched and cannot propagate upstream and sits at the interface of the two porous layers. This concept has been introduced for first by Babkin et al. [92], and it has been successfully demonstrated for gaseous [60; 94; 95] and for liquid fuel reforming to syngas [60; 61]. This research focused on the same principle, but demonstrated for the first time the applicability to heavy commercial fuels.

1.3.2 Lean operation

As the superadiabatic effect in porous media allows to extend the flammability limit, there are advantages also in the ultra-lean zone. Porous medium burners working at ultra-lean equivalence ratios have demonstrated low NOx and CO emissions compared to traditional burners and hence they obtained wide interest in the field of radiant heating applications [96]. The subsequent decrease in temperature due to the recirculation of the heat from the hot combustion products inhibits the formation of nitrogen oxides. NOx may be formed either by the thermal (Zeldovich) or prompt (Fenimore) mechanism. Because NOx formation is dependent on the peak temperature, NOx emissions are observed to decrease with decreasing equivalence ratio [97; 98]. Reduced temperatures in the combustion zone might be predicted to lead to increased emissions of CO and unburned hydrocarbons (UHC). However, the use of lean mixtures means that this is not the case. A number of investigations find that CO emissions tend to be very low (less than 40 ppm) and that they decrease with decreasing equivalence ratio [97].

It is in any case fundamental to avoid hot and cold spots to prevent formation of NOx, CO and UHC. For these reasons commercial products are already available in this area, such as in space and water heating, industrial furnaces for glass production, food industries, metal heat-treating, coating and paint drying, chemical processing, paper and wood drying, and food processing [99; 100]. Further lean-burn applications include the reburn of exhaust gases from existing combustion systems, and the mitigation of fugitive methane emissions.

1.3.3   Kinetic modeling

Some numerical works have been performed on partial oxidation of hydrocarbons in porous media. Ellzey et al. studied numerically the conversion of n-heptane in a porous medium reactor consisting of alumina pellets [4]. The model used treats the combustion process as one-dimensional and transient conservation equations are solved for mass, gas-phase energy, solid-phase energy, and gas species. Heat transfer processes include solid conduction within the porous matrix, convective heat transfer between the solid and gas, solid radiation and gas-phase conduction. Transport associated with species diffusion is also included. Chemical kinetics and transport processes are modeled using CHEMKIN and TRANFIT with an intermediate complexity mechanism for n-heptane [10]. The significant finding in this study is the path by which hydrogen is produced in a porous reactor, which consists in initial partial oxidation reactions and steam reforming occurring downstream of the main reaction zone. Small hydrocarbons play a key role in the steam reforming reaction, because they provide a valuable pathway to increase hydrogen production. The computational results shown in Fig. 1.4 illustrate the prediction for the structure of a heptane/air reaction zone within porous media. After the n-heptane is thermally broken down, there is formation and consumption of small hydrocarbon compounds as the hydrogen concentration continues to increase. The initial oxidation reactions result in a sharp increase in hydrogen in the main reaction zone. However, the hydrogen concentration continues to increase downstream of the main reaction zone due to steam reforming; evidence of which is illustrated by the peak and subsequent decrease of the water concentration in the gas. In the process of steam reforming, water is consumed to
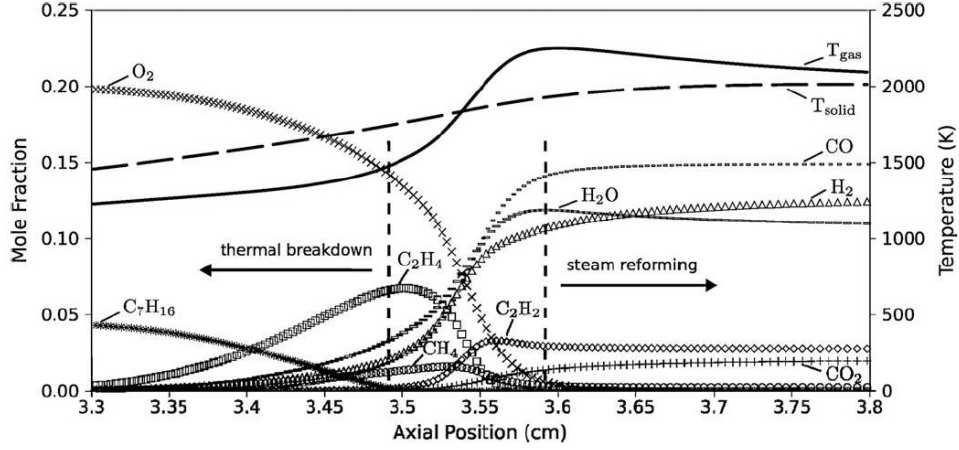
Figure 1.4: Computational structure of the reaction zone for n-heptane/air combustion at φ=2.5 and v=60 cm/s. Source [4].

form CO, CO_2, and H_2. The numerical analysis predicted that steam reforming contributed approximately 18% of the total hydrogen produced.

Similar behavior also appeared for the case of methane partial oxidations using a batch reactor model, the SENKIN code of CHEMKIN 3.6.2 [64]. This finding indicates that a long post-oxidation zone is necessary for the oxidation of the soot precursors and for reactions to complete. It can be also concluded that the injection of steam in the post oxidation zone will enhance the WGS and oxidized the soot that could be formed.

In ref. [101], the oxidation of n-hexadecane at φ=0.5, 1.0 and 1.5 has been modeled with a reaction mechanism consisting of 238 species and 1756 reversible reactions. At φ=1.5 and T=1000 K, n-hexadecane preferentially reacts with H (41.8%), and to a lesser extent with OH (17.1%) and CH_3 (16.6%); thermal decompositions represent 18.3% of the fuel consumption. This value increases to 83.2% at 1200 K.

Trimis et al. [5] performed experimental and numerical investigation of a TPOX reforming process for methane/air mixtures. The model showed the molar $H_2 : CO$ ratio increasing with decreasing air/fuel ratio (Fig. 1.5) and it was explained by considering the respective carbon monoxide and hydrogen formation pathways. Carbon monoxide is formed from reactions involving either the formyl

radical (HCO) or ketene (CH_2CO), the former being dominant for leaner mixtures while the latter for richer. Both HCO and CH_2CO are oxygenated species and their levels are expected to drop as the mixture becomes richer. At the same time, rich conditions favour both hydrogen radical and unburned hydrocarbons formation, thus promoting H abstraction reactions, such as:

$$CH_4 + H \rightarrow CH_3 + H_2 \tag{1.5}$$

and

$$C_2H_4 + H \rightarrow C_2H_3 + H_2 \tag{1.6}$$

which lead directly to H_2 formation. Also the acetylene fraction is predicted to increase with the equivalence ratio.
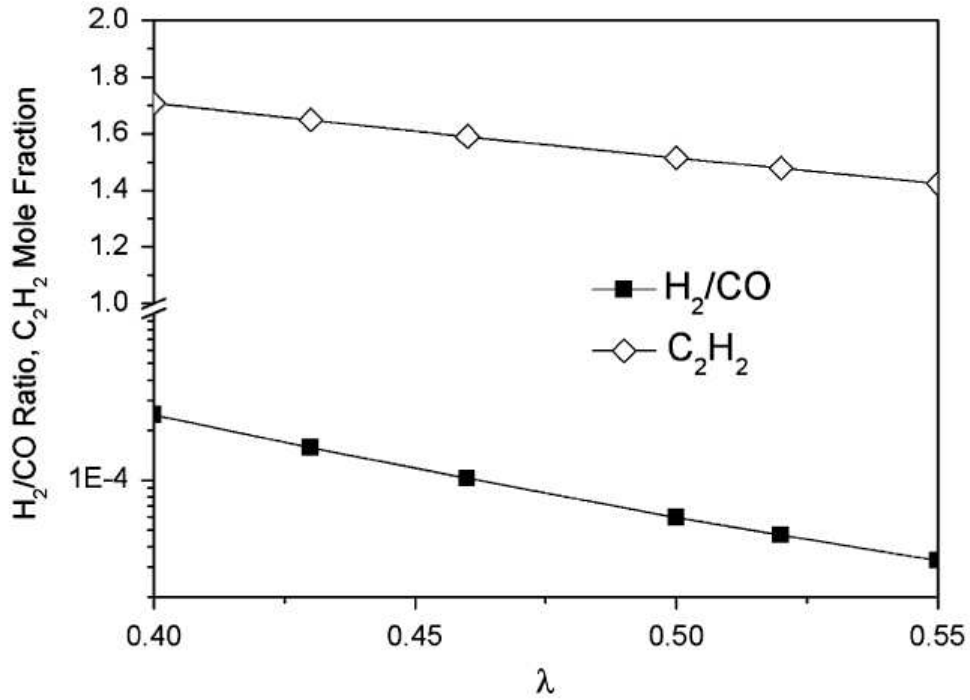
Figure 1.5: Computed exhaust $H_2 : CO$ and C_2H_2 levels as a function of mixture stoichiometry and for an air preheat temperature of 500°C. Source [5].

1.4   Scope of Thesis

1.4.1   Specific objectives

The main target of this thesis is to demonstrate experimentally the feasibility of a compact and flexible liquid fuel reformer for mobile applications. These two requirements led to consideration of the non-catalytic partial oxidation as the reforming technique. In this way it has been possible to reform common commercial fuels (diesel, kerosene and biodiesel), which, because of their poisoning compounds, cannot be reformed in any reformer involving catalysts. The partial oxidation technique allows reduction of the dimension of the reactor and the two-layer porous layer concept led to a sharp decrease in the device costs. The specific objectives of this thesis are to:

- design a compact reactor including a vaporization stage, an ignition strategy and a reforming layer;

- study the behaviour of the reformer varying the characteristic parameters of the system (equivalence ratio, thermal load, materials);

- demonstrate the flexibility of the system with different heavy liquid fuels;

- test the possibility of reducing the carbon monoxide content and improve the hydrogen fraction of the reformate.

1.4.2   Structure of Thesis

These targets were achieved and demonstrated with a set of experiments described in the following chapters. The second chapter describes the experimental methods, materials, fuels and measuring techniques that allowed optimisation and investigation of burner functionality. The third chapter concerns n-heptane reforming and presents a range of preliminary investigations, which lead to the burner characterisation in terms of mixture preparation and operating envelope of the burner. Moreover, parametric investigations have been performed to assess the sensitivity of the reformate composition to the characteristic parameters. The

use of a standard fuel allowed comparison of the results with chemical equilibrium data. The commercial fuel reforming experiments, described in the fourth chapter, demonstrate the flexibility of the reformer in processing commercial and carbon neutral fuels such as diesel, kerosene and biodiesel in the same burner. The last chapter describes the investigations and the preliminary tests on steam reforming and WGS in order to clean the reformate from poisoning species (CO) and approach the requirements of a fuel cell.

Chapter 2

Experimental methods

This chapter describes the experimental methods used in this project. The different stages to achieve fuel reforming are presented, including fuel and material specifications and the measurement techniques. At the end of the chapter, the procedure adopted to run the tests is also presented and the equilibrium and carbon balance calculation tools are explained.

2.1 Apparatus

The reformer developed for these experiments is illustrated in Fig. 2.1. Its distinctive characteristic is the two-layer porous structure, the atomizer section, and the capability to use various types of porous media. Different stages are implemented to achieve fuel reforming to syngas and they are explained in details in the following sections.

In principle, the liquid fuel needs to be atomized, vaporized and mixed with the oxidizer. Then the mixture must be ignited and eventually reforming takes place by means of the superadiabatic effect in the porous medium. In the experiments, the flow rates of air (oxidizer) and fuel are accurately delivered by means of two mass-flow controllers. Subsequently, the fuel needs to be intimately mixed with the oxidizer through liquid break-up and evaporation. This target is achieved using a modified commercial air-assisted atomizer and providing a hot environment where the mixture is formed. The unreacted mixture is then ignited by means of four spark plugs and stabilized over a flame holder. Thereafter, the

flame is switched to rich condition and the fuel is then reformed in the porous material that allows the superadiabatic condition to be established leading to the extension of the flammability limit. Eventually, gas samples have been analyzed by means of a Gas Chromatograph and soot emission was also investigated by means of a filter-paper-method machine.

Moreover, it has been necessary to monitor the temperature of the different stages. For this purpose, one K-type and two R-type thermocouples are inserted in the reactor in the vaporization stage, at the ignition level and at the exit of the burner (T_1, T_2 and T_3 respectively in Fig. 2.1).
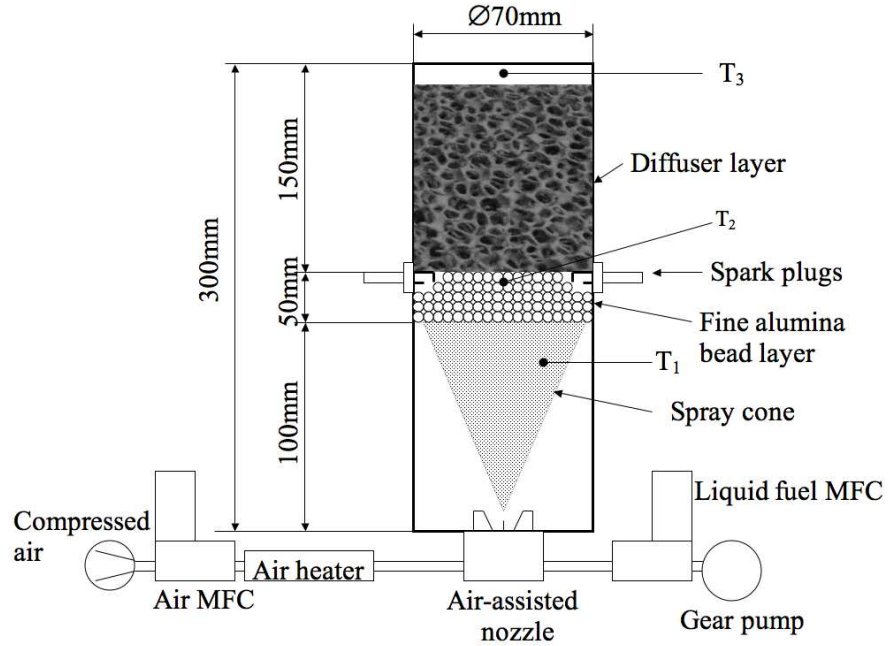
Figure 2.1: Equipment setup for burner A, B and C. Burner D has alumina beads as diffuser layer and burners E and F have a diameter of 100 mm.

2.1.1 Burners

Initially, 70 mm ID quartz tubes were used as burners in order to optically detect the flame inside the porous material, as shown in Fig. 2.2 where the tube is filled with two layers of alumina beads of different size. At the bottom of the tube a

brass plug was fixed and sealed with high-temperature O-rings and the nozzle was centrally attached. The complete vaporization of the fuels could also be visually checked, by denoting the absence of condensation on the tube's walls.

Later on in the project, stainless steel tubes have been adopted to approach the target of a practical device. A standard 316 SS grade was used due to its good machining and welding characteristics and for the broad availability of the material. Two different sizes were chosen in order to assess the scalability of the device. A 70 mm ID x 300 mm burner was the most tested version, but a 100 mm ID modular burner was also investigated for some steam reforming and water-gas shift reaction experiments (Chapter 5). Both the burners are flanged at the bottom, to fit and seal a plate with the nozzle, the T_1 thermocouple and a containing stainless steel cone fitted in it. The plate is sealed to the rest of the burner by a copper washer, since no plastic materials can withstand the high temperatures of the process, and checked periodically for liquid and gas leakage. The stainless steel burners are displayed in Fig. 2.3.

A 6 mm ID stainless steel tube coil has been wrapped around the burner to integrate the heat produced by the exothermic reforming reaction. This heat has been used to preheat the vaporizing air used to prepare the fuel/air mixture and hence the burner was independent from external heat sources after the start-up of the system.

The burners have been insulated with alumina wool (ZIRCAR Alumina mat) in order to minimize heat losses to the environment. Specifically, only the reforming layer was externally insulated, whereas the vaporization stage was left without any covering over the stainless steel tube. In this way the heat losses will not allow this section to overheat and hence will oppose the flame propagation to the upstream direction, preventing the ignition of the spray on the top of the nozzle.
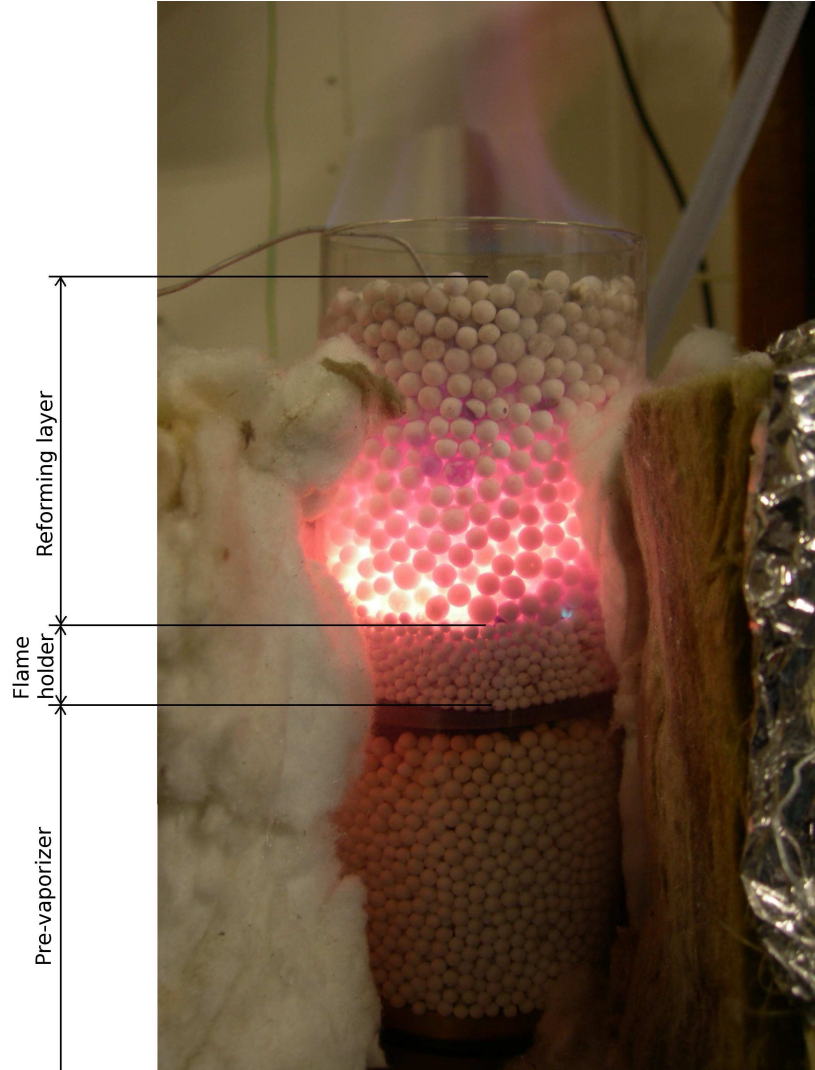
Figure 2.2: 70 mm ID quartz tube equipped with a 25 mm layer of 2-3 mm Al_2O_3 beads (flame holder) and a 80 mm layer of 6 mm Al_2O_3 beads (reforming layer). n-heptane/air flame at φ=2, P=5 kW and preheating temperature T_1=423 K. The flame on the rim of the burner is due to the autoignition of the syngas with the laboratory air.
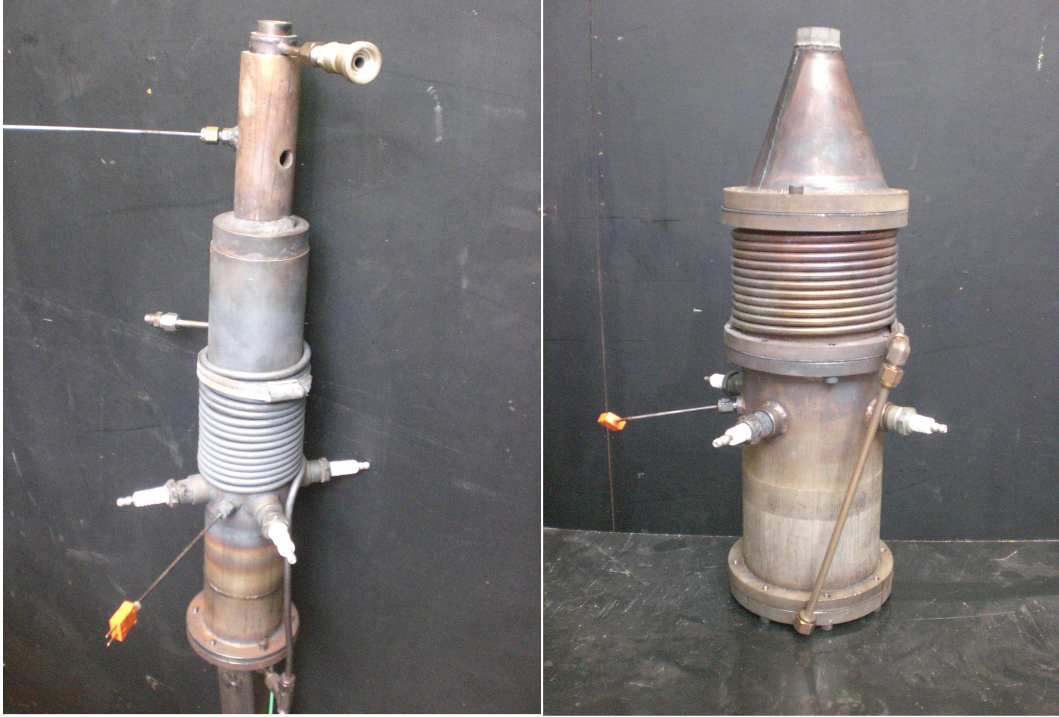
Figure 2.3: 70 mm ID burner and 100 mm ID burner equipped with spark plugs, coil stainless steel tube, thermocouples and top hoods.

2.1.2 Porous materials

The porous matrices used for the reforming layer are in the form of ceramic foam or beads. Table 2.1 summarizes the main features of each material. The fine-pore layer assists evaporation and prevents the flame to propagate upstream in most of the conditions investigated, while the second (downstream) layer is where the reforming occurs.

The first layer is a flame holder and it consists of a 50 mm long packed bed of 2-4 mm Al_2O_3 beads. The beads are held in place by a stainless steel wire mesh placed over the stainless steel containing cone. The bead material is commercially used for drying purposes (Sigma-Aldrich) and it has a melting point of 2313 K [102]. This layer also enhances oxidizer/fuel mixing before ignition because of the convoluted path that the mixture has to cover before reaching the layer interface.

On top of this first layer, different porous materials were implemented, foams (burner A, B, C, E and F) and beads (burner D). Five pieces of foams, different in terms of their porosity and material, have been tested (Fig. 2.4). The ceramic foams tested in this work come from the foundry industry for metal filtering and thus are high temperature resistant while the ceramic beads are designed as heat exchange media. Beads are more robust to thermal cycles compared to ceramic foams, which are brittle and crack after few (around 10) cycles of high temperature reforming and cooling down (Fig. 2.5a). Furthermore, beads have the advantage of ease of fitting inside the burner. The main drawback of the utilization of beads in place of foams is the higher thermal inertia due to the matrix geometry (thin solid bridges for ceramic foams compared to $\sim$6 mm diameter solid beads) and hence the lower response time of configuration D. Moreover, the ignition system used for burner A, B, C, E and F failed for burner D, because the heat released by the flame kernels does not offset the heat losses to the alumina beads. The flame had to be ignited from the top of the burner and the reaction layer slowly penetrated into the packed bed while heating the beads.

The foam pieces had to be wrapped in an alumina paper in order to seal them to the burner's walls, to minimize leaking around the porous media and to protect them from the different thermal expansion compared to the stainless steel tube. Zirconia foam is MgO stabilised and it exhibits higher resistance to high temperatures than the SiC, Al_2O_3, SiO_2 compound foam [103]. Fig. 2.5b shows the damage to the foam of burner C due to the high temperatures reached at equivalence ratios close to stoichiometry and the high thermal loads.

29

Table 2.1: Porous medium specifications.

Burner	A	B	C	D	E	F
Material	ZrO_2 foam	ZrO_2 foam	SiC, Al_2O_3, SiO_2 foam	$D \simeq 6$mm $\alpha - Al_2O_3$ beads	ZrO_2 foam	ZrO_2 foam
Porosity	30 ppi	10 ppi	30 ppi	40%[a]	30 ppi	30 ppi
Length [mm]	100	100	100	100	50	25
Max Temperature [K]	1973 [103]	1973 [103]	1723 [103]	1923 [105]	1973 [103]	1973 [103]
Thermal conductivity[b] $[Wm^{-1}K^{-1}]$	2	2	-	12-30 [106]	2	2
Supplier	Lanik	Lanik	Lanik	Almatis	Lanik	Lanik

[a]Packed bed porosity ε estimated by [104], with d_P particle diameter and D reactor diameter:

$$\varepsilon = 0.375 + 0.34\frac{d_p}{D}$$

[b]of the raw material

Figure 2.4: Porous foams used for the reforming layer. Specifications in Table 2.1 as burners A, B, C, E and F from left to right.

Figure 2.5: Foam failures: (a) ZrO_2 foam cracking after thermal cycles; (b) SiC, Al_2O_3, SiO_2 compound foam melted after high-temperature operations. The alumina paper wrapping is evident at the side of the cylindrical piece.

2.1.3 Flow control

The air flow is supplied by the laboratory compressed air line and it is controlled by a Bronkhorst Mass Flow Controller. The controller works on the thermal mass flow measuring principle (the temperature drift between no flow condition and gas flowing through a heated channel is directly proportional to mass flow through the sensor). The maximum pressure supplied is 2 bar (relative) before the nozzle. The air flow can be directed to a 750 W electric heater, able to preheat the air up to 573 K, or it can be switched to the stainless steel tube wrapped around the burner. During the experiment it may become necessary to mix the air preheated by the coil with some fresh air to keep the temperature at the desired value.

The liquid flow is delivered by a magnetic driven gear pump. The amount of liquid supplied is controlled by a mini CORI-FLOW Bronkhorst Mass Flow Meter which gives the voltage feedback to the pump according to the flow reading, adjusting the speed of the pump.

The mini CORI-FLOW is able to measure the density and the temperature of the liquid passing through and then it infers the flow rate, independently from the liquid characteristics and hence no calibration is required.

For safety reasons, only a small amount of liquid is kept next to the feeding system and the flow controllers shut their valves if a power cut occurs. Moreover, for better accuracy the fuel line is flushed with acetone before a different fuel is tested.

2.1.4 Atomization and vaporization

The atomization turned out to be one of the key and most delicate stages of the reforming process. Several commercial and custom-made nozzles have been tested before finding a suitable design. Eventually, a commercial air-assisted nozzle has been used for the experiments. The main issue was the processing of a very low liquid flow rate and the achievement at the same time of a good atomization quality. This goal has been achieved using a DELAVAN AL-15 nozzle, commercially used for heavy oil burners. The nozzle is designed around the external mix of air and fuel concept. In this nozzle, the liquid phase is ejected in a jet form and the air is impinging on it externally to the nozzle, causing the break-up and the

atomization. Therefore, this design allows independent control of the fuel and the air flow rate, giving high turndown ratios. The supplier certifies droplets with a Sauter Mean Diameter (SMD) of 50 μm and a spray cone of around 45 $^\circ$.

However, the commercial nozzle had to be modified to withstand the high temperatures of the experiments. In particular, all the plastic seals have been removed and the fuel channel has been replaced with a hypodermic tube in order to reduce the residence time of the liquid inside the hot nozzle housing. The nozzle is heated by the hot air flowing through and this can cause boiling of the liquid inside the fuel channel. Consequently, flow oscillations may occur with low boiling point liquids (i.e. n-heptane). An extra hypodermic tube has been added next to the fuel line in order to inject water for the steam reforming and water-gas shift reaction experiments. The different steps in the nozzle modification are illustrated in Fig. 2.6.

The spray flows in a 100 mm long stainless steel conical section and the evaporated fuel-air mixture reaches the first porous layer. A K-type thermocouple placed just before the upstream side of the first porous section (i.e. at the end of the atomiser-vapouriser conical section) gives the voltage feedback to the air heater through a temperature controller (T_1). This configuration is displayed in Fig. 2.7. Different temperature set points have been fixed, according to the fuel specifications, as explained in Section 2.2.

The uniformity of the air/fuel mixture has been assessed and the results are reported in Section 3.1.1. For that purpose, a Fast Flame Ionization detector (Cambustion HFR500 FFID) has been used. A 1.5 mm probe has been used to sample the carbon content of the mixture over the burner cross section immediately downstream the fine porous layer (flame holder). The detector gives the total C_1 as contributions from all the hydrocarbons present in the gas sample. The sample line has been kept at 423 K when sampling n-heptane/air mixtures, in order to avoid fuel condensation in the probe. Only n-heptane could be sampled, since the other fuels have higher boiling points. The machine probe head would suffer damages to the plastic sealings if its temperature is raised above 423 K and the condensation of fuel (especially from heavy fuel like the one used in this research) in case of lower temperatures would flood the machine and damage the sensors.

The FFID machine has a linearity of the output (voltage output over carbon concentration) until 2.0-2.5% C_1. After this threshold, the reading is lower than the actual value. Since the mixture sampled contained higher concentration of hydrocarbons (φ=2.0 leads to a molar fraction of 3.7% of C_7H_{16} in air), the reading is normalized over the average value, in order to detect variation from the mean value, rather than obtaining the exact proportion of fuel in air.

Figure 2.6: Exploded view of the DELAVAN AL-15 nozzle. (a) original version; (b) modified nozzle; (c) modified nozzle with water line.

Figure 2.7: Front and top view of the fuel pre-vaporizer. The T_1 thermocouple on top of the cone, the air and fuel inlet and the nozzle are visible in the two photographs.

2.1.5   Ignition

The main problem associated with this stage was the development of a stable flame in between the two "cold" porous layers. Tests with a quartz tube demonstrated the ease of quenching of a flame immediately after being generated by two electrodes with a gap of 2 mm on the peripheral area of the burner. The high heat losses to the porous matrix overcomes the heat generated by the flame kernel.

Eventually, the ignition has been achieved by fixing four automotive spark plugs evenly distributed on the burner walls at the porous layer interface. The peripheral position prevents the spark plugs to undergo the maximum temperature of the burner, improving the lifetime of the electrodes. Additionally, after few seconds of voltage applied to the plugs, four flame kernels quickly develop and cover the whole cross section of the tube. Thus, a long emission of unreacted mixture is avoided.

At the porous layer interface a R-type thermocouple is placed (T_2) and it gives the indication of successful ignitions. The actual temperature reading of this thermocouple is not taken into consideration as it is strongly affected by radiation from the porous material, the temperature of which cannot be measured in order to be used for a correction.

2.1.6   Temperature detection

The temperatures of the different stages have been measured by three thermocouples. T_1 is a K-type thermocouple with 1.5 mm bead diameter. K-type thermocouples have an accuracy within ± 2.5 K from 233 to 606 K which is suitable for the measurement of the evaporation stage temperature (max. 573 K) [107]. Two more thermocouples were located inside the burner. T_2 is a R-type thermocouple for the ignition detection at the porous layers interface and T_3 is a R-type thermocouple placed at the exit of the burner, where the gas samples are extracted. Both have a bead diameter of 0.5 mm and hence they are quick response detectors (0.025 seconds from 293 K to 373 K [107]). T_3 gives the temperature of the syngas that is eventually analyzed by the Gas Chromatograph and provides the indication of the achievement of a thermal steady state, once the reading

becomes constant. This temperature is also used to calculate the energy balance between the input species and the output species, to assess the heat losses (Section 3.27). R-type thermocouples' accuracy is within $\pm 0.0025 \cdot |T|$ K from 873 to 1873 K [107].

T_1 is directly plugged into the temperature controller for the electric air heater, whereas T_2 and T_3 are connected to an amplifier (Omega Omni-Amp IV), which provides also the cold junction compensation, and thereafter are plugged into a digital acquisition card (NI-PCI-6034E). Eventually, a computer equipped with NI Labview converts the voltage measured by these two detectors into a temperature reading.

2.1.7 Gas sample analysis

In order to collect a gas sample, it was necessary to quench the ongoing reactions and to remove the water vapour to avoid any damage to the gas chromatograph. A water-cooled probe attached to a vacuum pump allows the quenching and extraction of a sample of the exhaust gas at the burner exit. Subsequently, the sample is passed through a calcium chloride cartridge for water removal. Between the extraction and the drying stage, the sample line has been kept over 373 K to avoid water condensation, by using a heating cord wrapped around the extraction tube.

To obtain a consistent sample of the reformate, a hood with a 25 mm outlet has been attached to the top of the burners. Therefore, the sample analyzed represents a mixture of the gas coming from the very hot part (central) and from the cold parts of the burner (peripheral — close to the burner walls). This hood has a conical shape in order to avoid strong pressure drops which may affect the spray and the flame.

The gas samples have been injected into a gas chromatograph (GC). The GC is equipped with a Thermal Conductivity Detector (TCD) and with a Flame Ionization Detector (FID) and two columns for the species separation. The Molecular Sieve is used to separate H_2, O_2, N_2, CH_4 and CO. It is too retentive for C_2 hydrocarbons and it can be deactivated by CO_2 and H_2O. The Haysep N porous polymer column do not retain permanent gases and then H_2, air, CO and CH_4

pass straight through without separation. CO_2 is separated along with C_2H_2, C_2H_4 and C_2H_6. Therefore, the gas sample passes first through the Haysep N (porous polymer bead column) which retains carbon dioxide and C_2 hydrocarbons while the other species elute quickly to the Molecular Sieve column. A 3-way valve allows the bypass of the Molecular Sieve before CO_2 comes off the porous polymer bead column. Finally, the sample passes through the TCD (nondestructive detector) and afterwards through the FID (sample is combusted). The FID detector is about 100 times more sensitive than the TCD. This detector ionizes carbon atoms, in a hydrogen flame. Normally a hydrogen flame produces a negligible amount of ions, so only hydrogen carbon bounded compounds carried into the flame result in the formation of ions, whose quantity is measured in the FID and the carbon amount deducted.

The carrier gas used is high-purity Argon and pure air and 99.995% purity hydrogen were used for the FID flame. The machine is calibrated by a gas mixture with species concentrations similar to the ones expected in the reformate before every set of tests. The first calibration gas used was composed of 19.94% H_2, 1.00% O_2, 15.00% CO, 4.04% CO_2, 4.87% CH_4, 3.01% C_2H_2, 1.99% C_2H_4, 1.00% C_2H_6, balance nitrogen. Later on in the research, a new calibration gas was used, to match better the new syngas composition obtained through the system optimization: 19.83% H_2, 0.993% O_2, 18.09% CO, 2.95% CO_2, 4.00% CH_4, 2.98% C_2H_2, 2.01% C_2H_4, 0.514% C_2H_6, balance nitrogen. The sample line has been periodically checked for leaks and the samples have been injected at the same temperature and pressure. Given the partial oxidation process, no air should be present in the gas samples, therefore the absence of oxygen in the GC reading may insure that no leaks are present in the sampling line.

2.1.8 Particulate detection

Soot emission was investigated by means of a filter-paper-method machine (AVL 415S). A gas sample is taken from the exit of the burner with a probe and passed through a filter paper. The blackening of the filter paper is measured with a reflectometer and this indicates the soot content in the exhaust gas. The output

value (FSN) is the Filter Smoke Number and it corresponds to the Paper Blackening (PB), as defined by Eq. 2.1, for a sampling length of 405 mm at 298 K and 1 bar:

$$PB = \frac{100 - R_R}{10} \qquad (2.1)$$

with $R_R = \frac{R_P}{R_F} \cdot 100\%$ and R_P the reflectometer value of sample, R_F the reflectometer value of the unblackened paper and R_R the relative brightness of the sample. The soot detector extracted five gas samples for each condition and the average value is reported in Section 3.4 and 4.4.

2.2 Fuels

The fuels investigated in this work are n-heptane, Jet A-1 kerosene, commercial diesel oil and Rapeseed-Oil Methyl Ester (RME) biodiesel. Laboratory analyses were performed for Jet A-1, Diesel and biodiesel by the Chemistry Department Labs of Cambridge University. From the carbon-to-hydrogen ratio it is possible to calculate the approximate molecular formulas of the fuel which, together with the fuel specifications, are summarised in Table 2.2. n-heptane is high-purity laboratory grade fuel (99+%). The diesel oil used for the reforming experiments is commercial fuel from a local gas station and kerosene is from a supplier for the local airport. The RME biodiesel is rapeseed-oil based and follows the EN 14214 standards and requirements.

The choice of reforming n-heptane has been dictated by the possibility of comparing experimental data with numerical simulations and computational models, given the availability of chemical mechanisms [10] for such a reference fuel. Diesel, kerosene and biodiesel experiments represent practical applications of the reformer with commercial fuels. Different evaporation temperatures (T_1) have been set for ensuring full evaporation for each fuel. n-heptane has been vaporised in a 423 K environment. The boiling point range of Diesel is 457-648 K [108; 109] due to the different properties of the different component contained; consequently, the evaporation temperature was set to 573 K, being the maximum achievable

with the configuration adopted. It has to be noted that the first layer improves the vaporization process, as demonstrated by [110]. This effect is due to the high temperature of the first layer for the heat conduction and radiation coming from the downstream flame front and for the complex flow pattern covered by the mixture inside the ceramic bead layer, which enhances the heat transfer to the residual liquid spray phase. Similarly, kerosene boiling range is 463-523 K [108] and hence T_1 has been set at 523 K. The biodiesel/air mixture preparation temperature has been set at 523 K, limited by the risk of cracking at high temperatures, caused by the thermal instability of this fuel due to the presence of oxygen atoms in the fuel molecule, as explained by [111; 112]. Figs. 2.8, 2.9 and 2.10 give the GC-MS reading of those fuels. The spectra clearly show the presence of heavier hydrocarbon components in diesel compared to kerosene, as listed in Table dieselgcms and kerosenegcms. The biodiesel spectrum is consistent with similar analyses published for the same type of fuel [113]. The fuel specifications given by the suppliers are listed in Figs. 2.11, 2.12 and 2.13.

Table 2.2: Fuel specifications.

Fuel	n-heptane	Jet A-1	Diesel oil	RME biodiesel
Chemical formula	C_7H_{16}	$C_{12}H_{24}$	$C_{12}H_{23}$	$C_{19}H_{36}O_2$
LHV [MJ/kg]	44.926	42.800	43.000	37.600
Kinematic Viscosity [mm^2/s] @ 40 °C	0.51	1.0-2.0	2.0-4.5	3.50-5.0
Vapour Pressure [kPa]	0.05	0.5	0.5	<0.267
Density [kg/m^3] @ 15 °C	0.682	0.820	820-835	0.875-0.900
Heat of vaporization [kJ/kg]	318	251	250	254
Supplier	Acros	CPS fuels	Shell	ADM
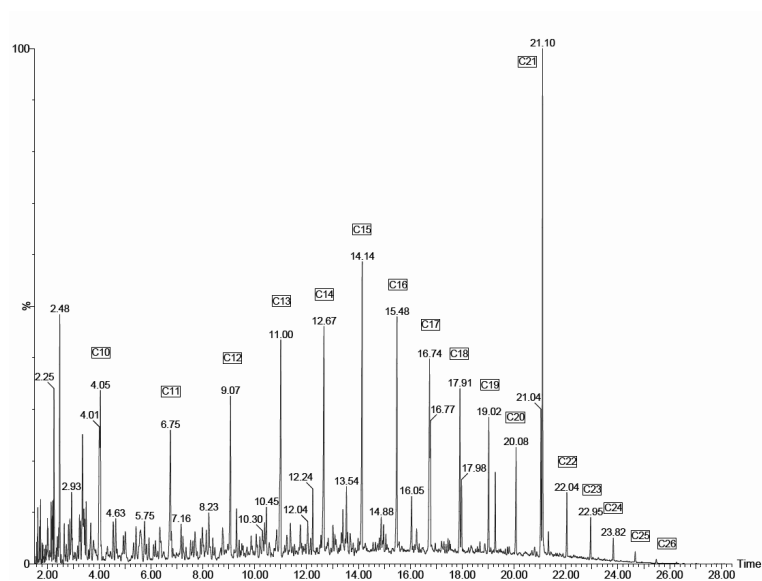
Figure 2.8: GC-MS output for Diesel oil.
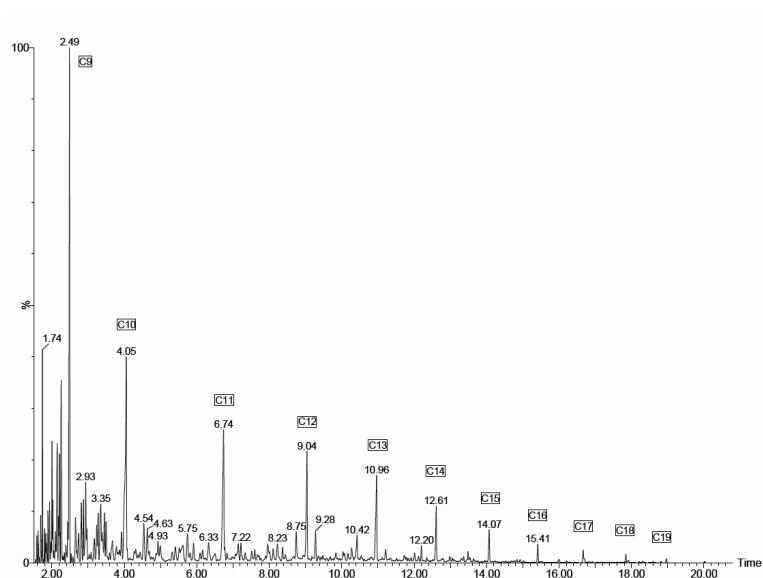
Figure 2.9: GC-MS output for Jet A-1.
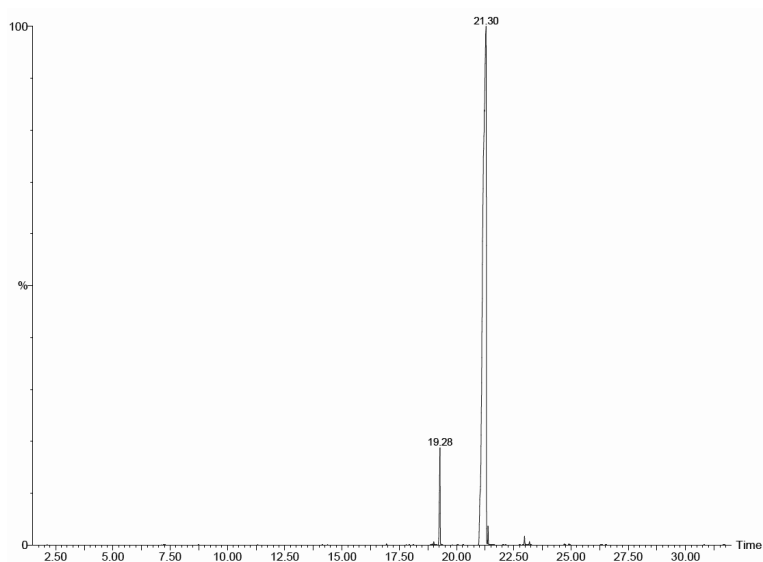
Figure 2.10: GC-MS output for RME biodiesel.

Table 2.3: Fig. 2.8 main peak description.

Peak number	Retention Time	Component Type
1	2.254	Aromatic
2	2.480	Unknown
3	3.354	Aromatic
4	4.007	Aromatic
5	4.047	Alkane
6	6.748	Alkane
7	9.068	Alkane
8	11.002	Alkane
9	12.669	Alkane
10	14.142	Alkane
11	15.482	Alkane
12	16.743	Alkane
13	16.769	Alkane
14	17.910	Alkane
15	17.976	Alkane
16	19.023	Alkane
17	19.276	Methyl Ester
18	20.077	Alkane
19	21.037	Unknown
20	21.097	Unknown
21	22.037	Alkane
22	22.950	Alkane
23	23.824	Alkane

Table 2.4: Fig. 2.9 main peak description.

Peak number	Retention Time	Component Type
1	1.740	Alkane
2	2.007	Alkane
3	2.147	Unknown
4	2.214	Alkane
5	2.260	Aromatic
6	2.487	Alkane
7	4.054	Alkane
8	6.741	Alkane
9	9.041	Alkane
10	10.962	Alkane
11	12.609	Alkane
12	14.069	Alkane
13	15.409	Alkane

SHELL DIESEL

**A high performance Ultra Low Sulphur Diesel meeting
BSEN590 containing a unique Performance Additive package**

Major Properties

Specification Parameters	Test Method	Units	Limit	Guarantee	Typicals
Sulphur (IP373)	IP 373	ppm	max	50	20 - 50
Density (ASTM D 4052)	D 1298	Kg/m^3	min / max	820 / 835	830 / 835
Distillation T95 (ASTM D86)	D86	%Vol	max	345	345

Other Properties

Specifcations	Test Method	Units	Limit	Guarantee	Typicals
Appearance		Visual		Clear & Bright	Clear & Bright
Cetane Number	ISO 5165	Number	min	51	58
Cetane Index	ISO 4264	Calc.	min.	46	54
Lubricity	ISO 12156-1	microns	max.	460	200 - 300
Cloud Point	D 2500	Deg C	max	Winter -5 / Summer +3	Winter -5 / Summer +3
CFPP	IP 309	Deg C	max	Winter -15 / Summer -5	Winter -15 / Summer -5
Viscosity	IP 71	cSt	min max	2.0 4.5	2.0 4.5
Ash	ISO 6245	% mass	max.	0.01	0.01
Carbon Residue	IP 398	% mass	max.	0.3	0.3
Copper Corrosion	IP 154	Class	max.	1	1
Distillation Recovered 250ºC	IP 123	Deg C	max.	65	65
Flash Point	ISO 2719	Deg C	min	>55	60
Particulate Matter	DIN 51 419	mg/Kg	max.	24	24
Water	IP PM BR	mg/Kg	max.	200	< 100
Oxidation Stability	ASTM D2274)	g/m^3	max.	25	25
Polycyclic Aromatics	IP 391	% m/m	max.	11	4

Figure 2.11: Shell diesel specifications [6].

Data Sheet
connediesel® CD 99

BIODIESEL

Oelmühle Hamburg
Aktiengesellschaft

PROPERTY	UNIT	METHOD	LIMIT acc. DIN EN 14214		Typical Data connediesel® CD 99
			MINIMUM	MAXIMUM	
Ester content	mm²/s	prEN 14103	96,5		99,5
Density (15 ℃)	g/ml	DIN EN ISO 3675	0,875	0,900	0,883
Kin. Viscosity (40℃)	mm²/s	DIN EN ISO 3104	3,50	5,00	4,5
Flashpoint (PM)	℃	DIN EN ISO 22719	101		> 170
CFPP	℃	DIN EN 116		0 / -10 / -20	=-12 / -12 / -20
Sulphur content	mg/kg	DIN EN 24260		10,0	< 10,0
Carbon residue (10% residue)	% (m/m)	DIN EN ISO 10370		0,30	< 0,30
Cetane number		ISO/DIS 5165:1996	51		54
Ash	% (m/m)	DIN ISO 3987		0,02	< 0,02
Water content	mg/kg	DIN EN ISO 12937		300	200
Total contamination	mg/kg	DIN EN 12662		20	< 10
Copperstrip corrosion		DIN EN ISO 2160		1	1
Oxidation stability	h	DIN EN 14112	6,0		8
Total acid number	mg KOH / g	DIN EN 14104		0,50	0,25
Iodine value		DIN EN 14111		120	112 - 115
Linolenic acid methyl ester	% (m/m)			12	< 12
Fatty acid methyl ester with ≥ 4 double bonds	% (m/m)			1	-
Methanol	% (m/m)	DIN EN 14110		0,20	0,01
Monoglycerides	% (m/m)	DIN EN 14105		0,80	< 0,8
Diglycerides	% (m/m)	DIN EN 14105		0,20	< 0,2
Triglycerides	% (m/m)	DIN EN 14105		0,20	< 0,2
Free Glycerine	% (m/m)	DIN EN 14105		0,020	<0,002
Total glycerine	% (m/m)	DIN EN 14105		0,25	0,15
Alkaline metals (Na + K)	mg/kg	DIN EN 14108 / 14109		5,0	< 3
Earth alkaline metals (Ca + Mg)	mg/kg	prEN 14538		5,0	< 3
Phosphorous	mg/kg	DIN EN 14107		10,0	< 7

Oelmühle Hamburg AG
D-21107 Hamburg
Fax + 49 - 40 - 7 51 94 - 1 70 / Tel. + 49 - 40 - 7 51 94 - 0

Figure 2.12: ADM biodiesel specifications [7].

CONOCOPHILLIPS LIMITED / JET :- UK MARKETING SPECIFICATION

REGULAR KEROSENE (BS 2869 CLASS C2)

SHEET 6

PROPERTY & UNITS		LIMIT	TEST METHOD Note (1)
Appearance @ Ambient Temp		Clear and bright, free from visible sediment and water	Visual
Odour		Merchantable	-
Density @ 15°C g/ml	Max	0.820	ASTM D4052 / IP 365
Smoke Point (mm)	Min	19	BS 2000 - 57
Flash Point (°C)	Min	38.0	BS EN ISO 13736
Char Value (mg/kg)	Max	20	BS 2000 - 10
Viscosity (cSt @ 40°C)	Min - Max	1.00 - 2.00	BS EN ISO 3104
Sulphur (%wt)	Max	0.10	ASTM D3227 / IP 342
Doctor Test or Mercaptan Sulphur (%wt)	Max	Negative 0.0025	IP 30 ASTM D3227 / IP 342
Copper Corrosion (3 hours @ 100°C)	Class	1	BS EN ISO 2160
Distillation (C) % Vol Recovered @ 20°C % Vol Recovered @ 21°C % Vol Recovered @ 24°C FBP (°C)	Min Max Min Max	15.0 90 50 300	EN ISO 3405 : 1998
Residue % Volume	Max	2	

THIS SPECIFICATION IS REPRESENTATIVE OF THE PRODUCT SUPPLIED BY CONOCOPHILLIPS LTD
AND WILL ALWAYS MEET BS 2869 (LATEST EDITION) CLASS C2 FOR REGULAR KEROSENE

Notes.

1) Latest Test Methods or technical equivalent used

2) Product will be marked with HM C&E statutory marker

THIS SPECIFICATION IS ACCURATE AT THE DATE OF ISSUE, AND SUPERSEDES ALL PREVIOUS ISSUES

Figure 2.13: CPS kerosene specifications [8].

2.3 Post reforming catalysis

In order to explore the possibility of reducing the carbon monoxide and hydrocarbon content of the syngas, two further stages have been implemented and tested. These two stages consists of a steam reforming stage to process the remaining light hydrocarbons present in the off gas and a water-gas shift reaction to transform the carbon monoxide to carbon dioxide and hydrogen. Both these stages need steam and a catalytic bed where the reaction can take place. Burner E was used for these experiments, due to the larger section area and therefore the longer residence time of the syngas inside the catalytic bed. It has to be noted that both the catalysts are poisoned by sulphur and therefore out of the fuels used in this project, only n-heptane and biodiesel could be tested.

2.3.1 Steam reforming catalyst

The steam reforming catalyst used for this investigation is the G 90-EW from Süd-chemie which is nickel-based on an aluminium oxide and calcium aluminate carrier in "spoked wheel" shape, as shown in Fig. 2.14a. Specifically, the component proportion on a weight basis is 11% Ni, 80% Al_2O_3, 9% CaO (bound as $CaAl_{12}O_{19}$) and less than 0.02% of Na and SiO_2. This catalyst is designed to process natural gas, but it will be shown later that it has excellent performance with the reformate produced by the partial oxidation of n-heptane, which contains (apart from hydrogen and carbon monoxide) mainly methane and acetylene. The operating temperature range for this catalyst is 773-1173 K and for this reason it was simply poured on top of the ZrO_2 foam, in order to use all the heat produced by the reforming process without the aid of any external heat source. A modular section of 100 mm in length was filled with this material.

2.3.2 Water-gas shift catalyst

The catalyst used for the water-gas shift reaction is the NextCatA from the supplier Fuelcellsmaterial.com. It comes in pellet shapes (Fig. 2.14b) composed of Zirconia doped with Ceria and 2% of Pt. The catalyst is for high-temperature

49

operations and the working range is 673-1073 K. A cartridge filled with pellets was attached to the top of the hood of burner E.

Figure 2.14: (a) Süd-chemie G 90-EW steam reforming catalyst wheels; (b) Fuelcellsmaterial.com ZDC/Pt catalyst pellets.

2.4 Procedure

A typical test procedure starts with the warming up of the reactor by a flow of only the oxidiser (i.e. the air) through the reactor to bring the temperatures up to the appropriate value corresponding to the fuel characteristics so as to avoid fuel condensation. This first stage takes approximately from 10 to 20 minutes, depending on the fuel that is processed. At this point, the fuel is injected. An air/fuel ratio close to stoichiometry and a thermal power of 2 kW is used first to achieve a prompt ignition. At this condition, the unreacted air/fuel mixture flow velocity nearly matches a typical hydrocarbon laminar flame speed at φ=1.0 (approx. 40 cm/s [114] at normal atmospheric temperature and pressure) for the size of the burners used in this experiment. The four automotive spark plugs are activated and provide the means of ignition. After the ignition, the reaction zone quickly extends inside the porous matrix and the equivalence ratio is switched to rich values. When the thermocouple on the top of the burner (T_3) gives a constant reading, the system has reached thermal equilibrium and samples can

be extracted through the sampling line. From cold to fully stabilised operation, the system takes about 20-30 minutes, depending on the fuel.

2.5 Equilibrium calculation

The experimental molar fractions of H_2, O_2, N_2, CO and CO_2 and hydrocarbons up to C_2 (methane, acetylene, ethylene and ethane) have been compared to thermodynamic equilibrium calculations. The results were obtained by means of a computational tool which elaborates the NASA database thermodynamic coefficients [115]. The inputs to this code are the pressure (atmospheric in our case) and the temperature of the mixture whose equilibrium composition is to be calculated. Two options were used: (a) the adiabatic flame temperature corresponding to the φ and initial T (T_1) used, calculated by [116], and (b) the experimentally-determined sample temperature (T_3).

2.6 Carbon balance

An algorithm has been written and used to calculate the water content of the syngas. An iterative water molar fraction value has been introduced in the calculation in order to minimize the O:N ratio of the dry species minus the O:N ratio of the wet species, since the O:N ratio must be conserved. In this way the water mole fraction is estimated and hence the percentage of H_2 bound by water and light hydrocarbons present in the off-gas can be estimated.

The sum of the three components (molecular hydrogen, hydrogen in hydrocarbons and hydrogen in water) ranges from around 90% down to 75% of the hydrogen contained in the fuel molecule over the equivalence ratio. The discrepancy at rich equivalence ratios may be due to the soot formation or to deposits which have been detected on the first porous layer (flame holder). Moreover, potential formation of hydrocarbons not detectable by the Gas Chromatograph or condensed in the drier cartridge together with water may contain the missing hydrogen. Hydrocarbons not detectable are those higher than C_2 which, even if in small fractions, can "hide" large quantities of hydrogen. The Gas Chromatograph columns can tolerate a maximum temperature of $160\,°C$ and hence high-boiling

point hydrocarbons cannot be analyzed by the described configuration in any case.

Chapter 3

n-heptane reforming

This chapter deals with the experimental investigations carried out on n-heptane reforming. Several parameters have been explored such as the thermal load, the equivalence ratio, the different material characteristics and the burner size effect on the syngas composition. Some preliminary studies have also been performed concerning the homogeneity of the unreacted air/fuel mixture before the layer interface and the syngas composition uniformity over the cross section of the burner. Also the operating range of one of the configurations has been investigated, demonstrating the superadiabatic effect on the flame speed.

3.1 Preliminary investigations

In this section the mixture uniformity, the reformate uniformity over the cross section of the burner and the operating range of the reformer have been investigated.

3.1.1 Mixture homogeneity

The functionality of the atomisation and evaporation stage of the burner has been investigated in terms of mixture homogeneity by means of the HFR500 FFID and with the methodology described in Section 2.1.4. The tests have been conducted on the 70 and 100 mm ID burner with n-heptane/air mixtures at P=7 kW and φ=2.0, 2.5 and 3.0 with a preheat temperature of 423 K. The mixture

was sampled at 100 Hz and 1000 readings were recorded and averaged at 10 mm displacement steps of the probe above the flame holder layer. Fig. 3.1 shows the results of this investigations with the plot of the local voltage output normalized by the average value over the cross section of the fuel/air mixture at φ=2.0 for the two burners. It can be noted that the mixture is richer than the average value in the central part of the burners, whereas on the sides it results leaner. However, the deviation is limited to $\pm 2\%$ for the 70 mm ID burner and to $\pm 5\%$ for the 100 mm ID burner.

The same investigation has been carried out at φ=2.5 and 3.0 at P=7 kW. Fig. 3.2 and Fig. 3.3 display the results from the two burners. A mixture inhomogeneity is more marked at higher equivalence ratios. At φ=2.5 the deviation from the average value is around $\pm 4\%$ and $\pm 10\%$ and at φ=3.0 it reaches $\pm 7\%$ and $\pm 15\%$ for the small and big burner respectively. Probably, the modification of the nozzle design and the reduced air flow rate at high equivalence ratios impede the initial breakdown of the liquid jet and hence may affect the uniform distribution of the air/fuel mixture over the burner cross section. This disparity is very mild for the small burner and confined to the peripheral area of the cross section, whereas it is stronger for the 100 mm ID burner. This is may also be due to the narrow spray cone angle (45°) that prevents the mixture to cover uniformly the cross section of the tube. Nevertheless, in view of the relatively small mixture inhomogeneity and the further mixing achieved inside the reforming section, it is expected that the reformate composition will be uniform across the burner. This is demonstrated in more detail in the next Section.
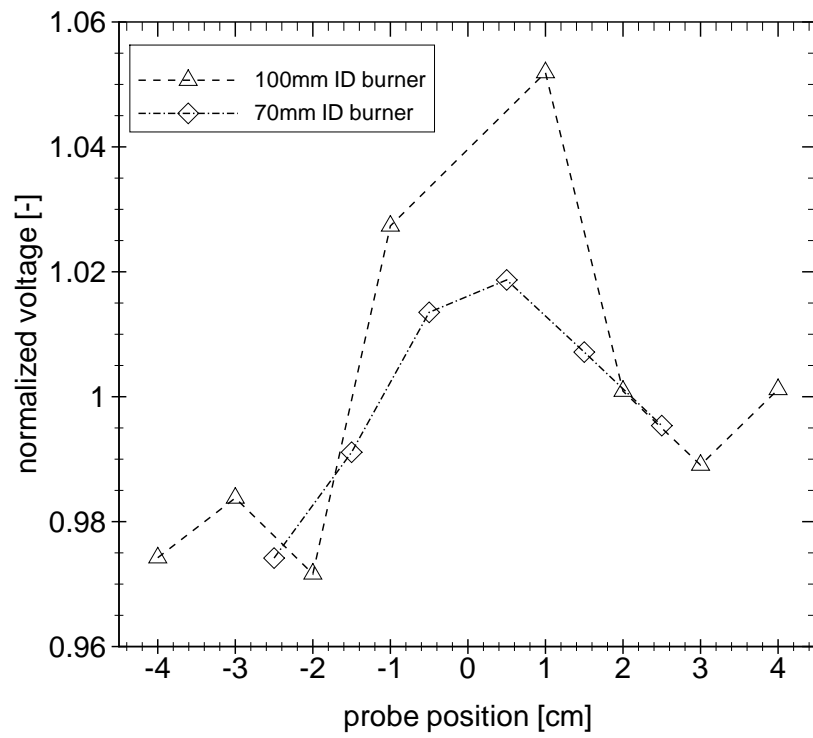
Figure 3.1: Reactant mixture over the first porous layer (flame holder) measured by the FFID and expressed as normalized voltage over the cross section of the two size burners (70 and 100 mm ID) at P=7 kW and φ=2.0.
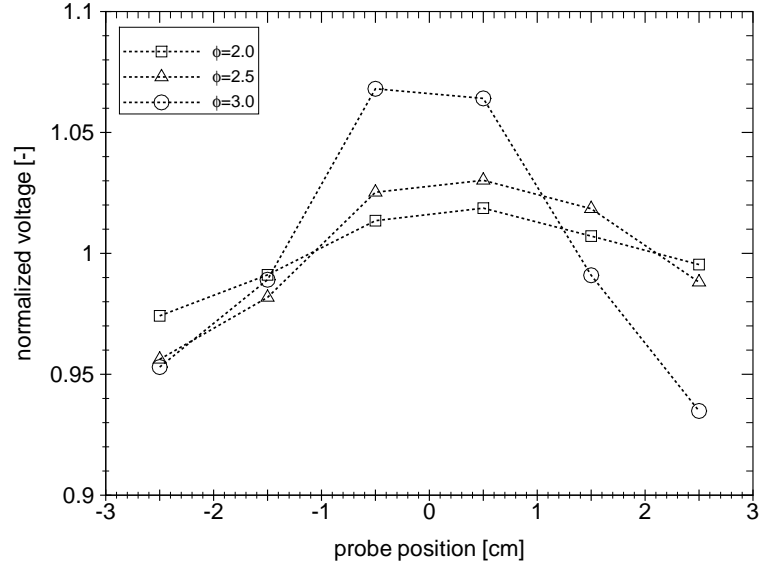
Figure 3.2: Reactant mixture over the first porous layer (flame holder) measured by the FFID and expressed as normalized voltage over the cross section of the 70 mm ID burner at P=7 kW and φ=2.0, 2.5 and 3.0.
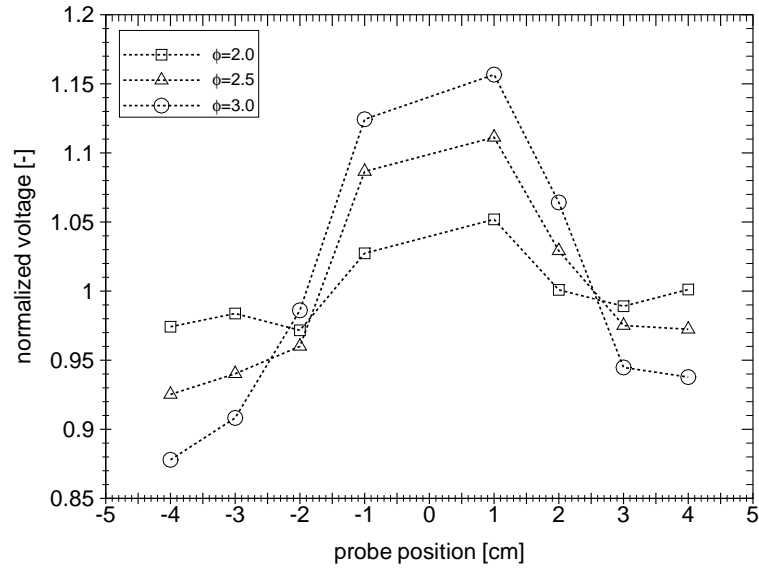
Figure 3.3: Reactant mixture over the first porous layer (flame holder) measured by the FFID and expressed as normalized voltage over the cross section of the 100 mm ID burner at P=7 kW and φ=2.0, 2.5 and 3.0.

3.1.2   Reformate uniformity

After the investigation of the air/fuel mixture before ignition, a similar test has been carried out for the uniformity of the syngas composition after the porous reforming layer. For this purpose, burner E has been used (100 mm ID tube with a 30 ppi ZrO_2 foam), since it developed the largest divergence from a uniform distribution of air/fuel mixture. Five different locations were sampled, going from the burner walls to the centre of the tube. The extraction of the gas sample has been carried out right above the foam, before diffusion and mixing could occur. Also the temperature has been recorded at the different sampling points.

The results are shown in Fig. 3.4. The syngas composition results to be uniform over the radial positions, whereas the temperature trend follows a parabolic curve over the flame holder layer, due to the heat losses at the walls. Hydrogen and carbon monoxide peaks at the centre of the reformer and they are lower in molar fraction at the peripheral area. Similarly, the temperature peaks at the centre because of the heat losses at the tube's walls. The syngas composition difference between the five sampling points is anyway very limited and it is contained within 10% variation of the average value.
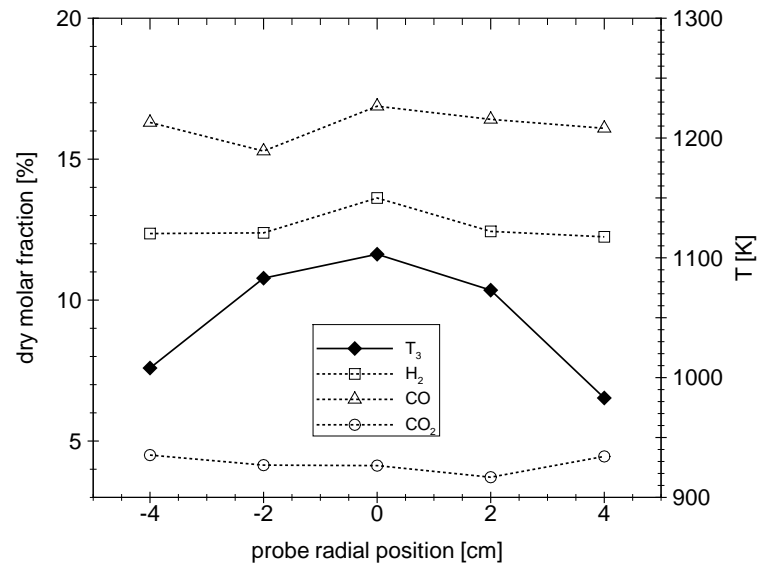
Figure 3.4: Syngas composition and exit temperature T_3 over the reforming layer of burner E at P= 7 kW and φ=2.0.

3.1.3 Operating envelope

The operating points of the burner have been explored in order to detect stationary flame conditions. Burner C was used for this purpose. The thermal load has been fixed and flames with equivalence ratios ranging from 1.5 to richer values were investigated. Then further sets of tests were carried out with a higher thermal load. Four different flame behaviours have been observed: (a) quenching – the heat produced by the flame does not offset the heat losses and the flame cannot be sustained; (b) flash-back – the flame speed is high enough (or the flow rate low enough) to penetrate the flame holder layer in the upstream direction and ignite the mixture in the vaporization area; (c) filtration wave – a reaction wave travels from the layer interface up to the top of the burner; (d) steady flame stabilized at the interface or immediately downstream. This condition is the one of interest in this work. The difference between conditions (c) and (d) was detected by the temperature measurements. When the thermocouple placed at the interface (T_2) gave a constant and higher reading than the exit gas temperature (T_3), a filtration wave did not initiate and the flame would stabilise. On the contrary, a filtration wave gives a decreasing reading of the interface temperature T_2 with time. A steady condition is associated with the stabilisation of the reaction zone in the first half of the large pore layer, as demonstrated by [90]. Moreover, the flow and fuel/air proportion conditions (P and φ) have been kept constant for at least 20 mins, as a filtration wave travels with a speed around 10^{-4} m/s [62; 63; 92] , which means that the flame would reach the top of the porous matrix in approximately 16 mins, for this specific configuration. Therefore, if the flame did not appear on the top of the porous media after 20 mins, the working point was included in condition (d).

The operating envelope is described in Fig. 3.5, where the working points of the reactor are plotted at different flow rates and equivalence ratios. Since the flame is stabilised, the flow velocity in the burner is equivalent to the flame speed. High equivalence ratios (up to φ=5.0) were reached and a maximum flame speed of 88.6 cm/s at φ=2.0 has been achieved, limited by the equipment maximum scale and the hazard of the great heat produced. The broadest steady operating zone occurs at φ=2.0, consistent with [117].

The experimental results have been compared to numerical calculations of free premixed flames (i.e. in the absence of porous media) carried out by means of a commercial code (COSILAB) [9]. The calculated flame speeds are for a free n-heptane flame at the corresponding preheat temperature and equivalence ratio of the experimental results. A detailed mechanism for n-heptane have been used [10]. The comparison of the two sets of data demonstrates that the flame in the porous media achieves much higher flame speeds than the the free flame at the same φ, showing the establishment of superadiabatic conditions.
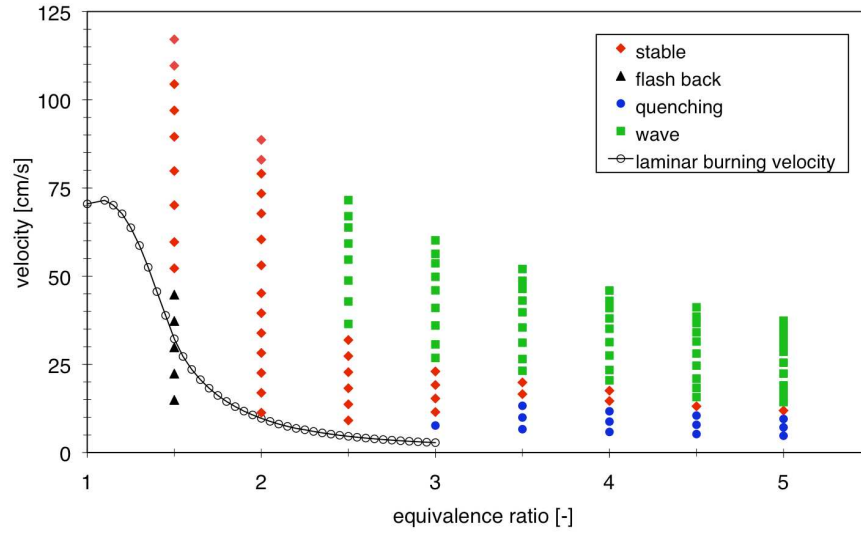
Figure 3.5: Operating envelope for burner C for n-heptane reforming at a preheat temperature of 423 K. Laminar burning velocity of free premixed flames calculated by the code COSILAB [9] and a detailed chemical mechanism [10].

3.2 Parametric investigations

This section deals with the sensitivity of the syngas composition on different parameters, namely equivalence ratio, thermal load, porous material and burner size.

3.2.1 Thermal load effect

The effect of the thermal load on the syngas quality for a fixed equivalence ratio has been investigated in burner A. The thermal load is defined in this work as the mass flow rate of fuel multiplied by the lower heating value ($P = \dot{m} \cdot LHV$) and thus it is strictly related to the bulk velocity of the flow inside the burner. The equivalence ratio has been kept constant at φ=2.0, since, as demonstrated by Section 3.1.3, at this condition the burner showed stationary flame conditions for a broad range of flow speed. The thermal load range has been varied from 2 to 12 kW, corresponding to a flame speed ranging from 11.3 to 67.6 cm/s. The results are reported in Fig. 3.6. The dry molar fractions of hydrogen and carbon monoxide increase and approach equilibrium as the thermal load increases. Similarly, the dry carbon dioxide molar fraction decreases with P. In Fig. 3.7, the experimental dry molar fraction of hydrogen, carbon monoxide and carbon dioxide is compared to the calculated equilibrium at the measured exit temperature T_3. The similar trends and the similarity of the values demonstrate consistency of the experimental results.

The increase of hydrogen and carbon monoxide concentration may be attributed to the higher reaction temperatures which are measured with increasing thermal loads. Fig. 3.8 demonstrates this increase with the plot of the measured exit temperature (T_3) compared to the adiabatic flame temperature of a n-heptane/air mixtures at φ=2.0 over the thermal load. Also, the light hydrocarbons present in the syngas show a decrease in their concentration passing from a thermal load of 2 kW to 7 kW and afterwards the molar fractions assume constant values. This enhancement is highlighted also by the conversion efficiency, defined by Eq. 3.1:

$$\eta_{LHV} = \frac{\dot{m}_{H_2} LHV_{H_2} + \dot{m}_{CO} LHV_{CO}}{\dot{m}_{C_7H_{16}} LHV_{C_7H_{16}}} \qquad (3.1)$$

η_{LHV} is 46.6% at P=2 kW and increases up to 70% at P=7 kW and then it improves slowly up to almost 72% at P=12 kW, as shown in Fig. 3.10. Analogously, the molar hydrogen conversion, given by Eq. 3.2, can be introduced and it represents the percentage of H_2 present in the reformate over the H_2 content of n-heptane, in terms of molar fraction X:

$$\eta_{H_2} = \frac{X_{H_2,out}}{8 X_{C_7H_{16},in}} \qquad (3.2)$$

η_{H_2} is 27.8 % at P=2 kW and increases up to 48.1% at P=7 kW and it reaches 49% at P=12 kW. Fig. 3.9 displays the hydrogen distribution in the products. It can be noted that molecular hydrogen percentage increases with the thermal load reaching a peak at P=7-8 kW and it assumes a constant value afterwards.

Higher thermal loads have not been investigated due to equipment limitations, the hazard of the high temperatures and the high hydrogen and carbon monoxide flow rates produced. Similarly, lower thermal loads than 2 kW have not been investigated for the risk of damaging the air heater at low air flow rates and for the little heat produced by the flame which could not offset the heat losses to the sides of the burner and by radiation downstream.
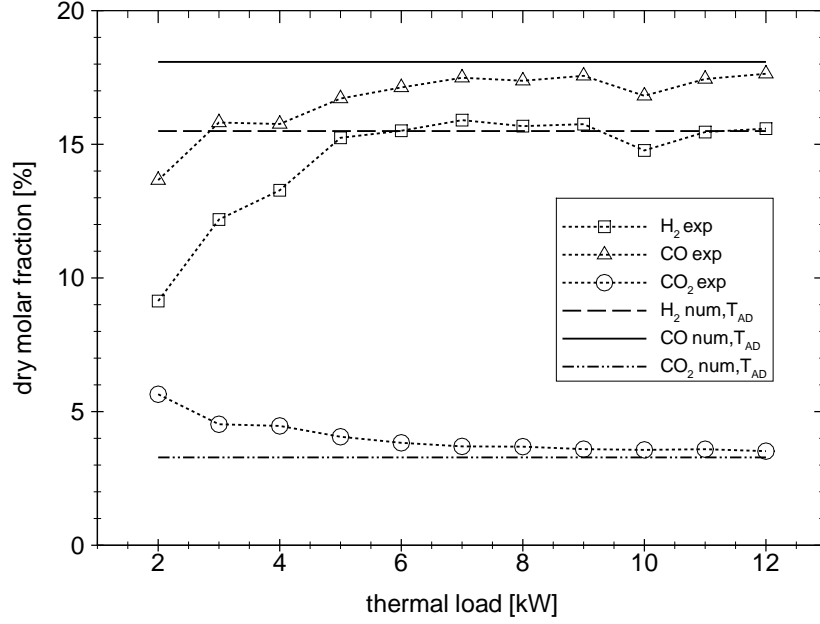
(a)
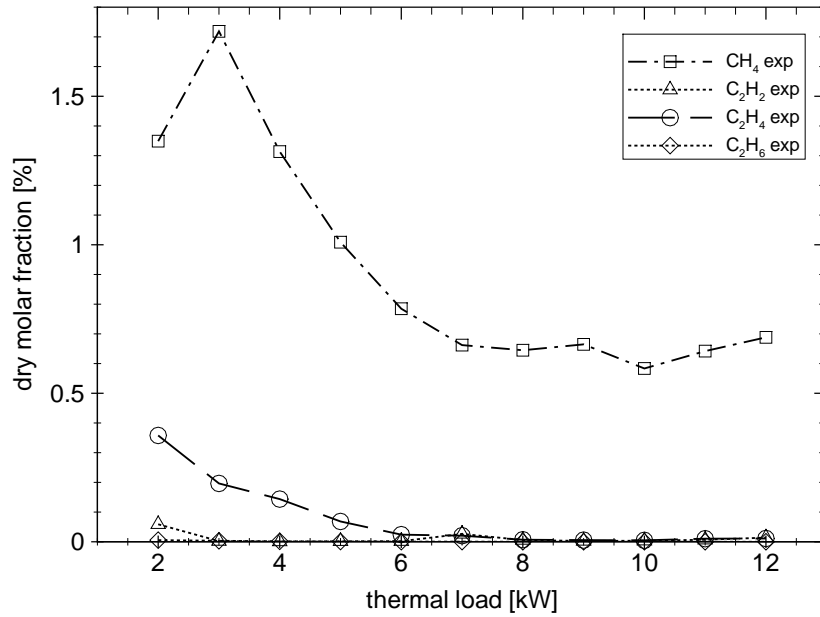
(b)

Figure 3.6: Calculated equilibrium at the adiabatic flame temperature and the experimental mole fractions (on a dry basis) for a inlet air/fuel temperature of 423 K at various thermal loads for n-heptane reforming at φ=2.0 for burner A. (a) Hydrogen, carbon monoxide and carbon dioxide. (b) Measured methane, acetylene, ethylene and ethane.
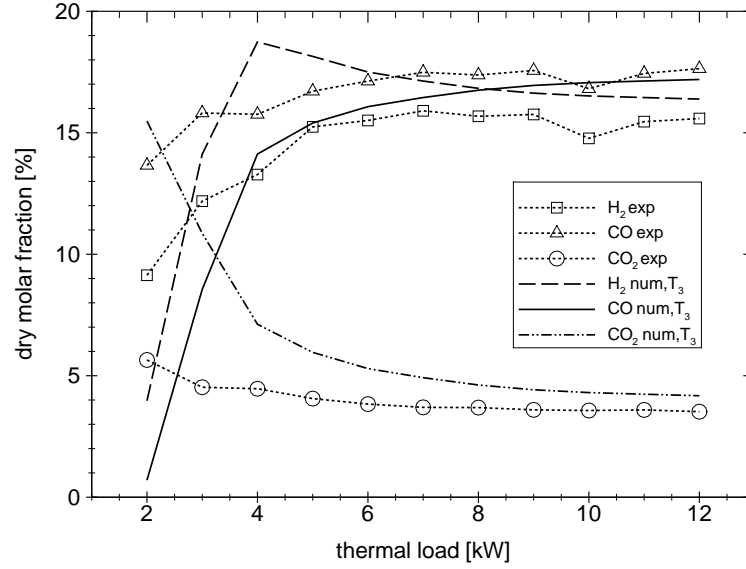
Figure 3.7: Calculated equilibrium at the measured exit temperature T_3 and the experimental mole fractions (on a dry basis) of hydrogen, carbon monoxide and carbon dioxide for a inlet air/fuel temperature of 423 K at various thermal loads for n-heptane reforming at φ=2.0 for burner A.
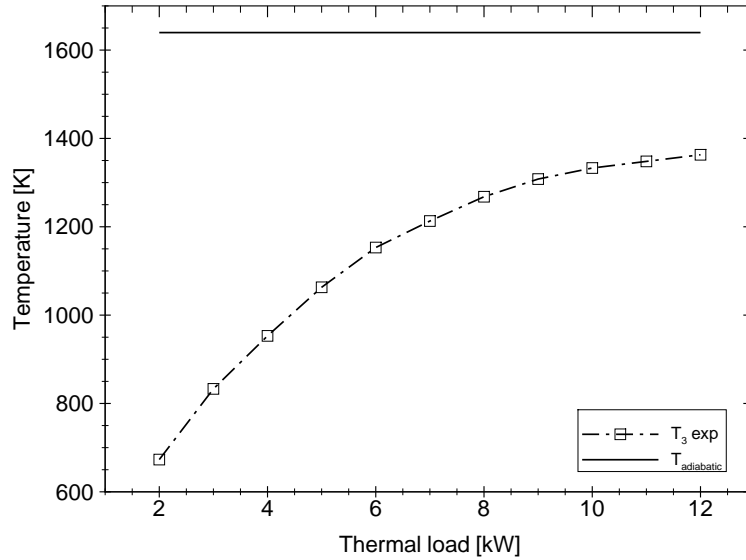
Figure 3.8: Adiabatic and experimental exit temperature T_3 for n-heptane reforming at conditions as in Fig. 3.6.
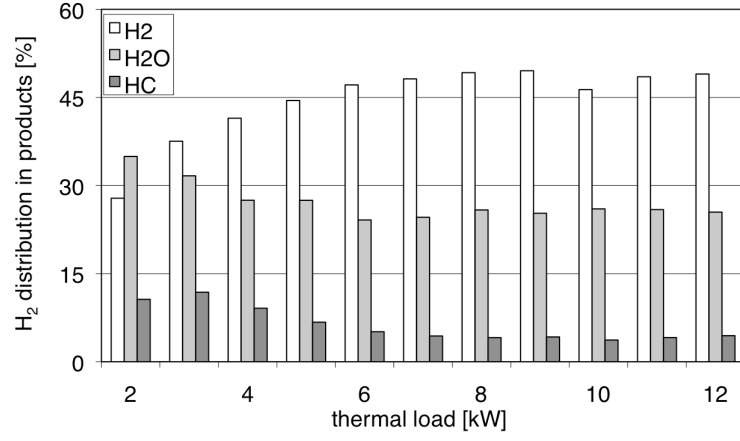
Figure 3.9: H_2 distribution in hydrogen, water and hydrocarbons present in n-heptane reformate as a function of thermal load based on processing of the measured dry molar fractions. Conditions as in Fig. 3.6.
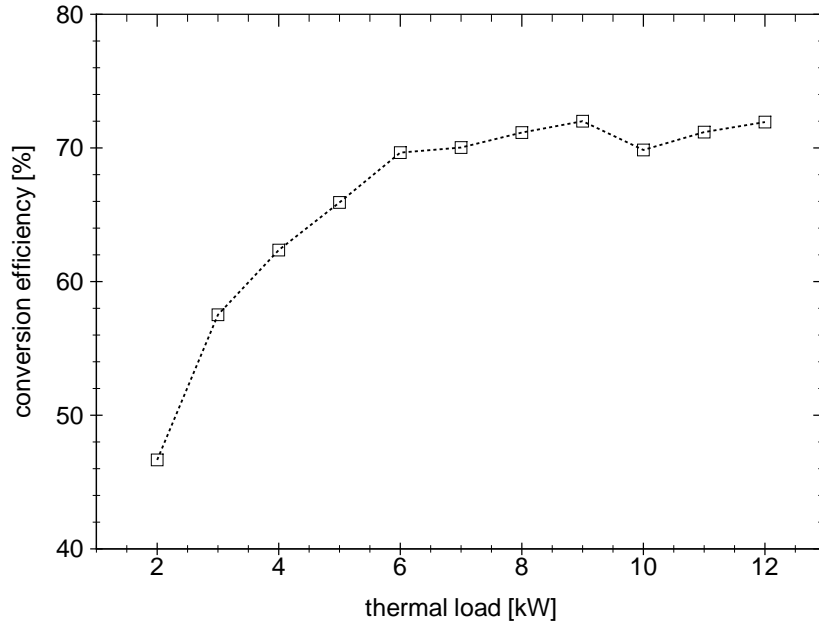
Figure 3.10: Conversion efficiency for n-heptane reforming at $\varphi=2.0$ and at various thermal loads for a preheat temperature of 423 K.

65

3.2.2 Equivalence ratio effect

Different porous materials for the reforming layer (burners A, C and D) at thermal loads ranging from 6 to 8 kW have been tested at equivalence ratios from φ=1.1 to φ=3.0 with steps of 0.1. The results from the equivalence ratio effect on the reformate are shown in Figs. 3.11, 3.12, 3.13, 3.14, 3.15, 3.16, 3.17, 3.18 and 3.19 where the experimental molar fractions on a dry basis of H_2, CO, CO_2 and of hydrocarbons up to C_2 are displayed, along with the calculated equilibrium data for burner A, C and D at P= 6, 7 and 8 kW. The thermodynamic equilibrium calculations predict negligible concentrations of hydrocarbons.

The general trend is a monotonic increase of the hydrogen and carbon monoxide molar fraction and decrease of carbon dioxide molar fraction against the equivalence ratio. Experimental results and calculated thermodynamic equilibrium data are very close up to φ=1.7 for P=6 kW and up to φ=1.9 for P=7 and 8 kW for burner A. For burner C at φ=1.7, H_2, CO, CO_2 dry molar fractions are: 10.0% and 10.2%, 14.2% and 15.7%, 4.8% and 4.3% for the experimental and equilibrium results respectively. At P=7 kW and φ=1.9 the dry molar fractions of H_2, CO, CO_2 for burner A are 13.4% and 13.8%, 15.9% and 17.3%, 4.2% and 3.6% for the experimental and equilibrium results respectively. For burner D, experimental data coincide well with equilibrium calculated molar fractions up to an equivalence ratio of φ=2.0-2.1. At P=8 kW and φ=2.0, burner D presents the following H_2, CO, CO_2 molar fractions: 15.4% and 15.5%, 17.9% and 18%, 3.4% and 3.3% for the experimental and equilibrium results respectively. For all the conditions displayed, at φ richer than 2.0, hydrogen and carbon monoxide molar fractions stay constant, whereas the hydrocarbon (HC) presence increases considerably. For instance, passing from φ=2.1 to 2.9 for burner A, H_2, CO and CO_2 molar fractions pass from 15.28% to 15.29%, 16.7% to 15.8% and from 3.8% to 2.9% respectively, whereas methane increases from 1.18% to 3.3%, acetylene from 0.7% to 1.8%, ethylene from 600 ppm to 1.3% and ethane from below detectable limit to 140 ppm. Hence, the disparity of the hydrogen and carbon monoxide values between the experimental and equilibrium data is probably due to the formation of light hydrocarbons at high equivalence ratios.

Rich flames lead to a large presence of hydrogen and carbon monoxide in the samples but at the same time the reaction temperatures drop because for the technique used in this study the heat provided is solely produced by the oxidation process. Consequently, after an increase of H_2 and CO molar fractions, the fuel is reformed to light hydrocarbons rather than to syngas, because of the lower temperature of the process. Ideally, by providing more heat (i.e. the steam reforming concept relies on external heat sources [118]), the syngas molar fraction curve over the equivalence ratio may increase monotonically.

In general, the operating point around φ=2.0 has demonstrated better performance in terms of high stability and repeatability, high conversion efficiency and low soot formation for the foam burners. This aspect is underlined by Fig. 3.20a, where the H_2 content is maximised at φ=2.0 for burner A at P= 7 kW. High water content is exhibited at lower φ and high HC content is observed at higher φ. Both water and light hydrocarbons act as hydrogen sinks. Also the conversion efficiency, defined by Eq. 3.1, peaked around the same condition, as illustrated by Fig. 3.20b. It is also interesting to note the consistent anomaly in the hydrocarbon molar fraction trend at around φ=2.5, especially for Fig. 3.11b, 3.14b, 3.16b and 3.19b. Such behaviour may need further investigations and analysis.
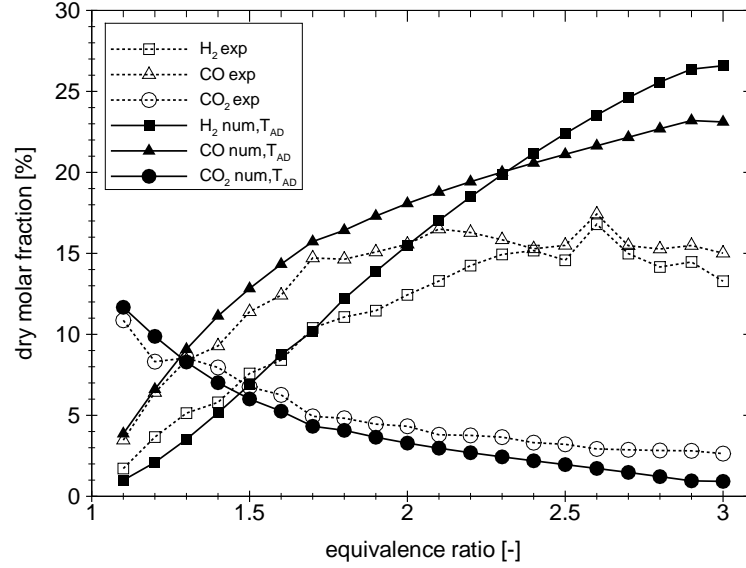
(a)
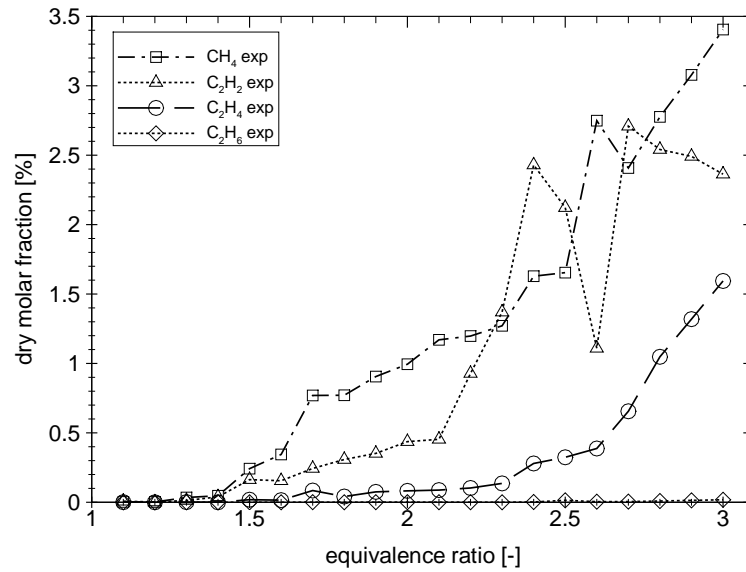
(b)

Figure 3.11: Calculated equilibrium at the adiabatic flame temperature and the experimental mole fractions (on a dry basis) for a inlet air/fuel temperature of 423 K at various equivalence ratio for *n*-heptane reforming at P=6 kW for burner A. (a) Hydrogen, carbon monoxide and carbon dioxide. (b) Measured methane, acetylene, ethylene and ethane.

(a)

(b)

Figure 3.12: Calculated equilibrium at the adiabatic flame temperature and the experimental mole fractions (on a dry basis) for a inlet air/fuel temperature of 423 K at various equivalence ratio for n-heptane reforming at P=7 kW for burner A. (a) Hydrogen, carbon monoxide and carbon dioxide. (b) Measured methane, acetylene, ethylene and ethane.

(a)

(b)

Figure 3.13: Calculated equilibrium at the adiabatic flame temperature and the experimental mole fractions (on a dry basis) for a inlet air/fuel temperature of 423 K at various equivalence ratio for n-heptane reforming at P=8 kW for burner A. (a) Hydrogen, carbon monoxide and carbon dioxide. (b) Measured methane, acetylene, ethylene and ethane.
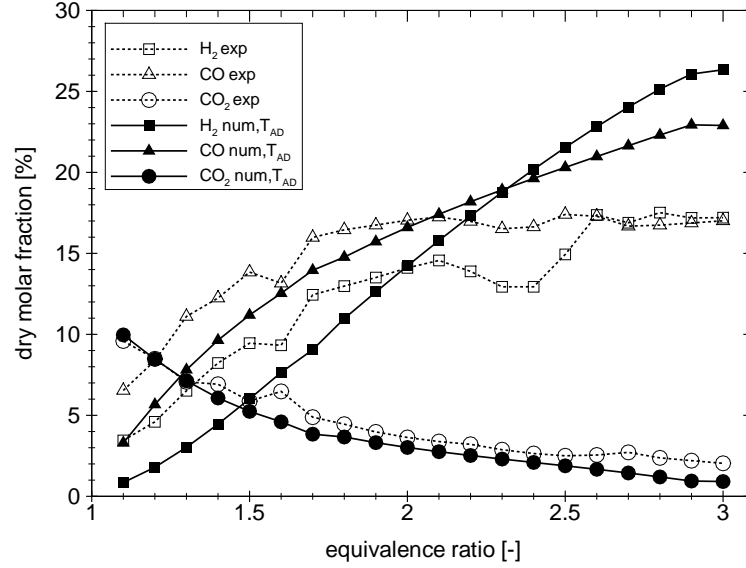
(a)
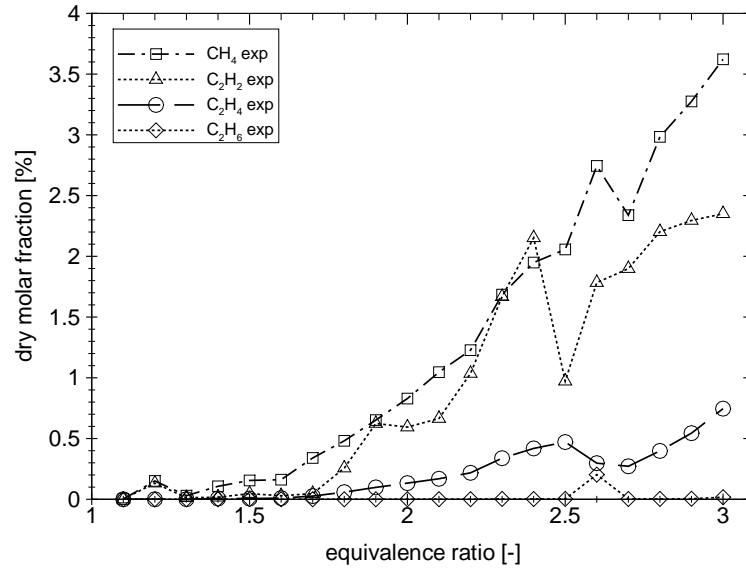
(b)

Figure 3.14: Calculated equilibrium at the adiabatic flame temperature and the experimental mole fractions (on a dry basis) for a inlet air/fuel temperature of 423 K at various equivalence ratio for *n*-heptane reforming at P=6 kW for burner C. (a) Hydrogen, carbon monoxide and carbon dioxide. (b) Measured methane, acetylene, ethylene and ethane.
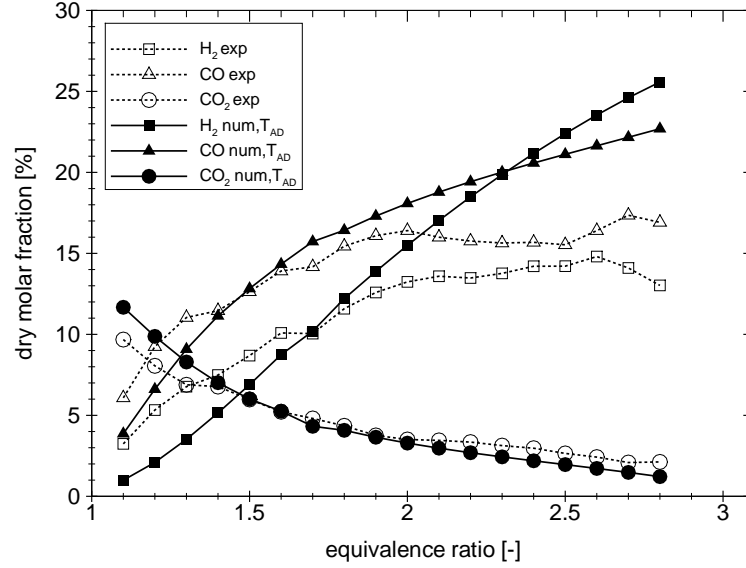
(a)
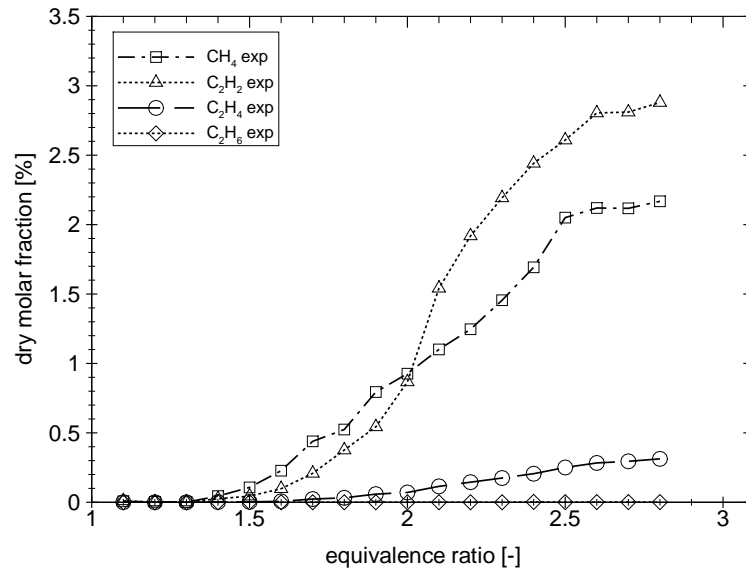
(b)

Figure 3.15: Calculated equilibrium at the adiabatic flame temperature and the experimental mole fractions (on a dry basis) for a inlet air/fuel temperature of 423 K at various equivalence ratio for *n*-heptane reforming at P=7 kW for burner C. (a) Hydrogen, carbon monoxide and carbon dioxide. (b) Measured methane, acetylene, ethylene and ethane.
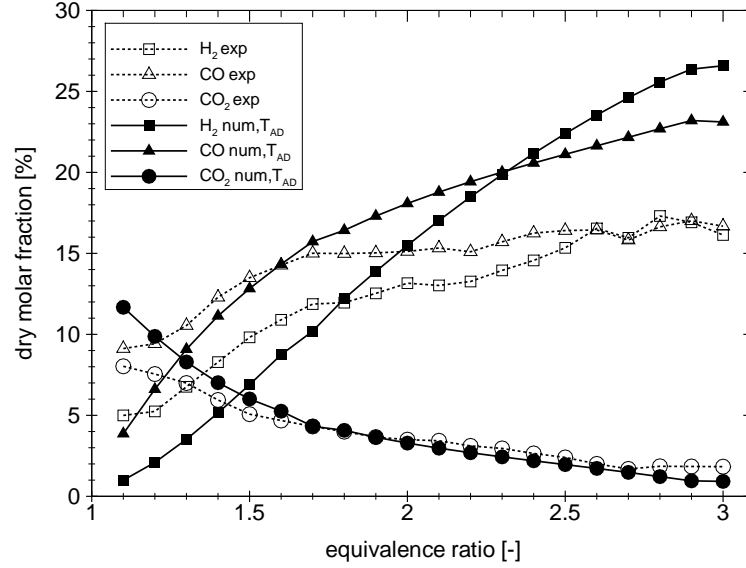
(a)
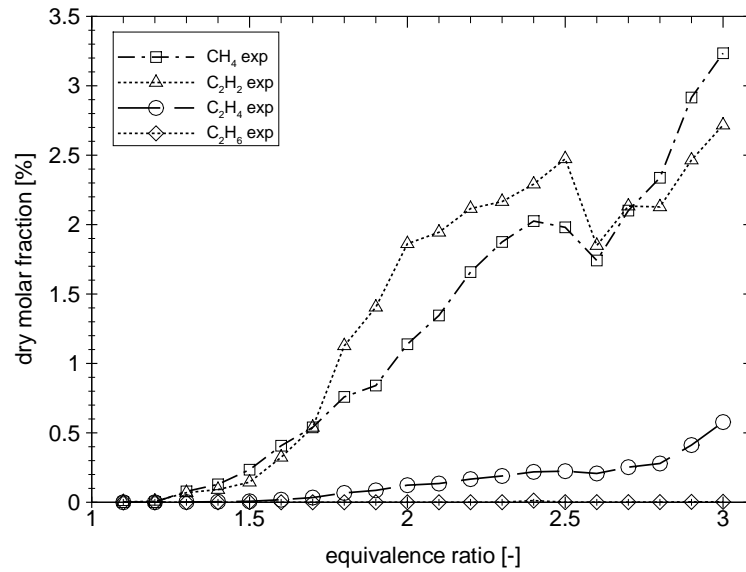
(b)

Figure 3.16: Calculated equilibrium at the adiabatic flame temperature and the experimental mole fractions (on a dry basis) for a inlet air/fuel temperature of 423 K at various equivalence ratio for *n*-heptane reforming at P=8 kW for burner C. (a) Hydrogen, carbon monoxide and carbon dioxide. (b) Measured methane, acetylene, ethylene and ethane.
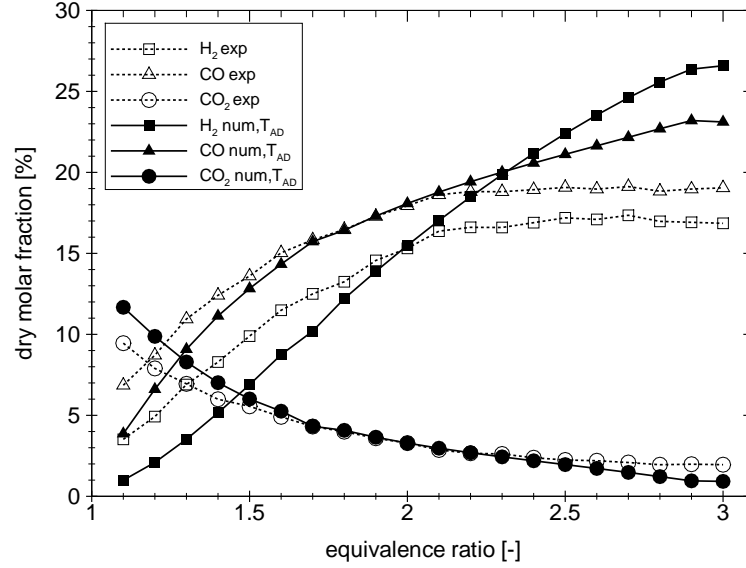
(a)
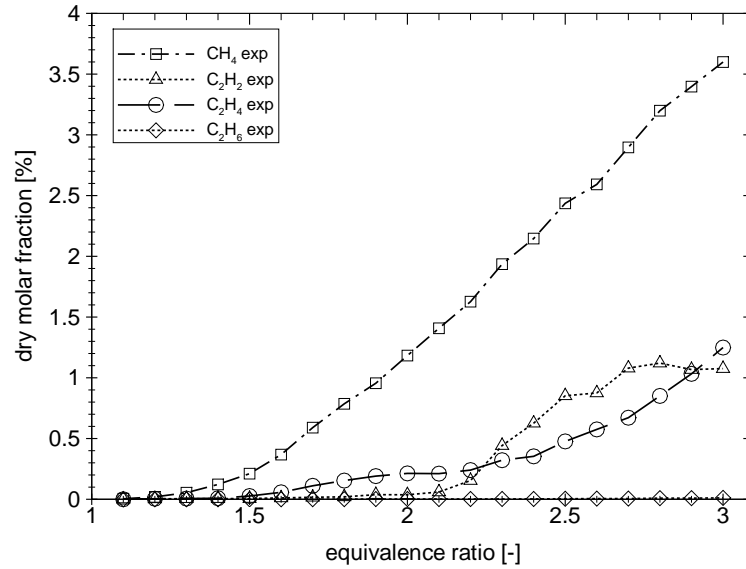
(b)

Figure 3.17: Calculated equilibrium at the adiabatic flame temperature and the experimental mole fractions (on a dry basis) for a inlet air/fuel temperature of 423 K at various equivalence ratio for *n*-heptane reforming at P=6 kW for burner D. (a) Hydrogen, carbon monoxide and carbon dioxide. (b) Measured methane, acetylene, ethylene and ethane.
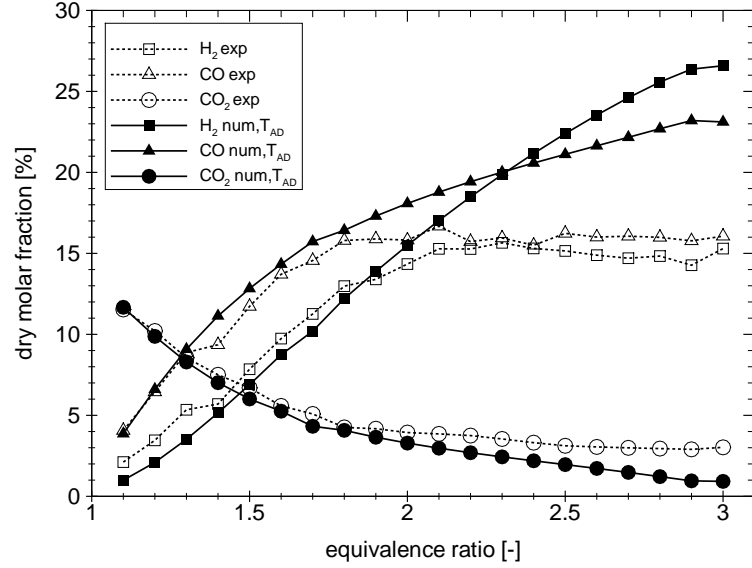
74
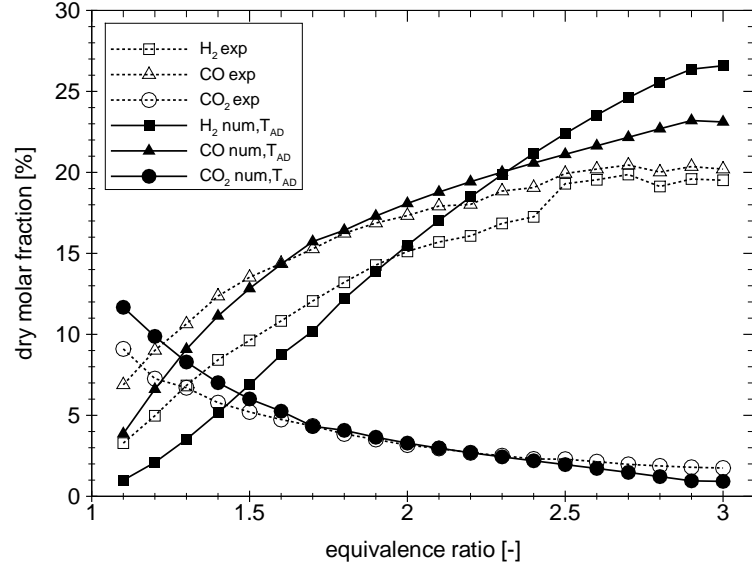
(a)
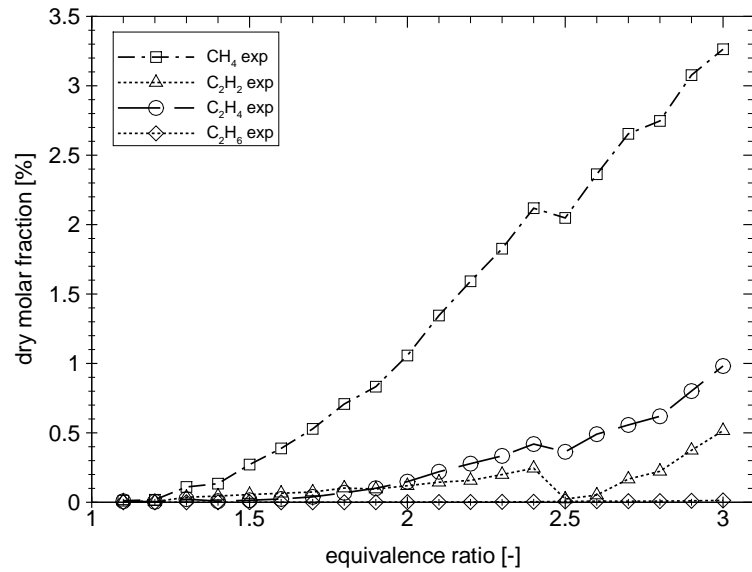
(b)

Figure 3.18: Calculated equilibrium at the adiabatic flame temperature and the experimental mole fractions (on a dry basis) for a inlet air/fuel temperature of 423 K at various equivalence ratio for *n*-heptane reforming at P=7 kW for burner D. (a) Hydrogen, carbon monoxide and carbon dioxide. (b) Measured methane, acetylene, ethylene and ethane.
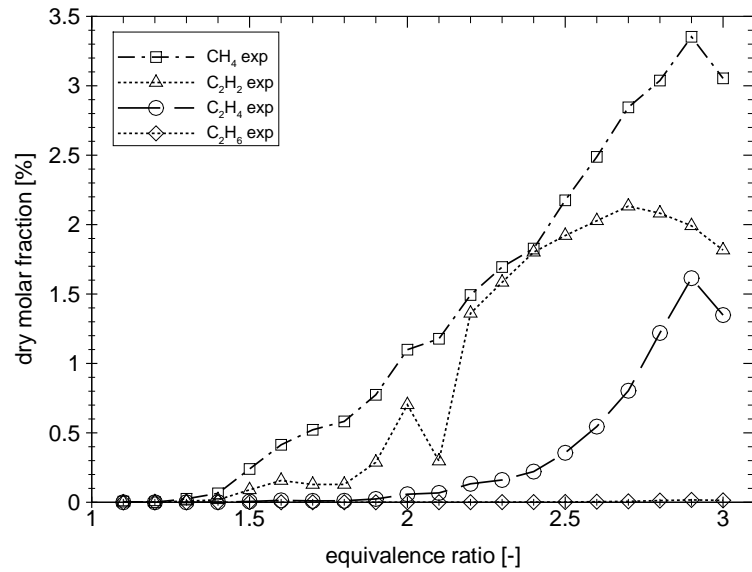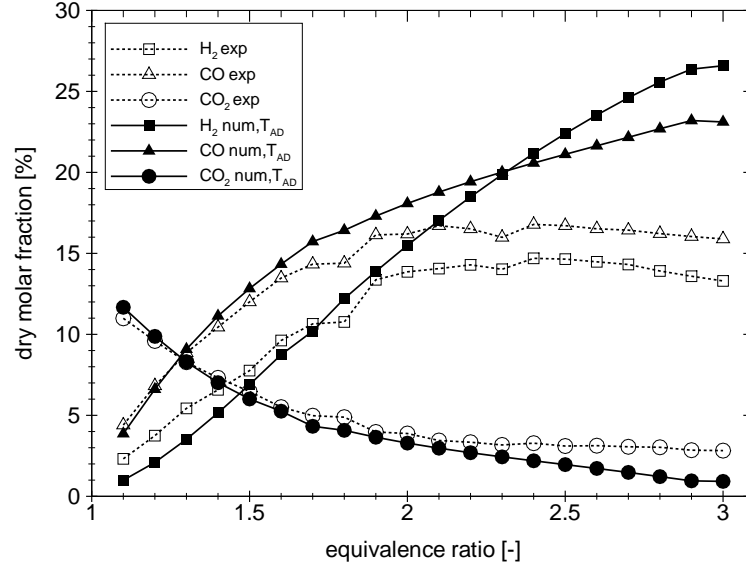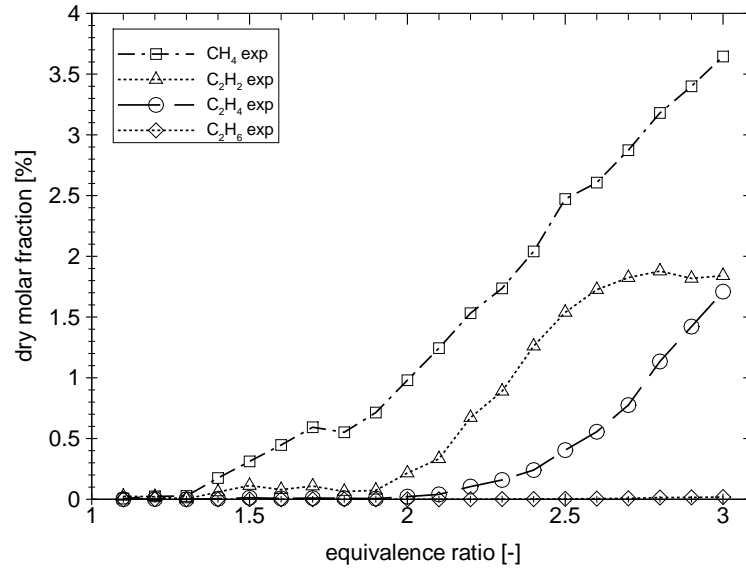
75
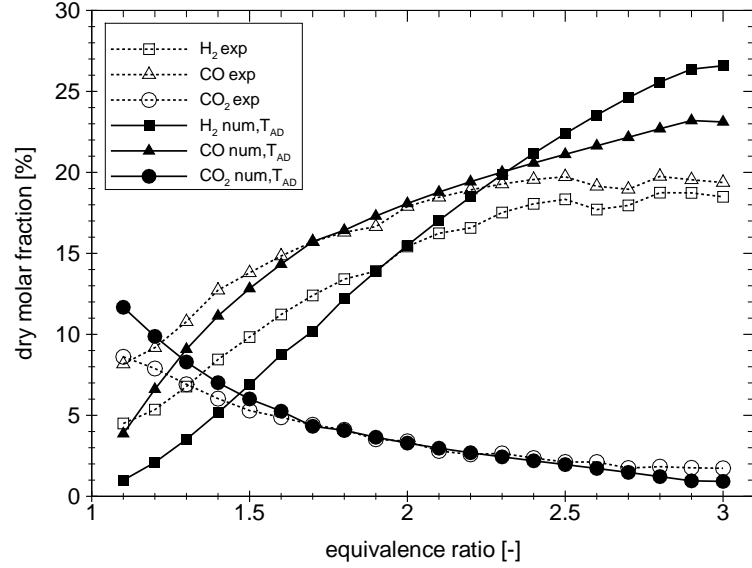
(a)
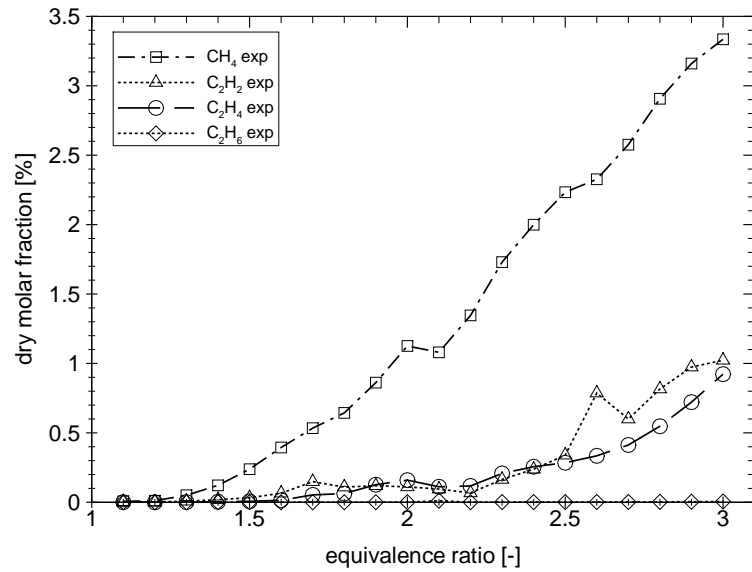
(b)

Figure 3.19: Calculated equilibrium at the adiabatic flame temperature and the experimental mole fractions (on a dry basis) for a inlet air/fuel temperature of 423 K at various equivalence ratio for n-heptane reforming at P=8 kW for burner D. (a) Hydrogen, carbon monoxide and carbon dioxide. (b) Measured methane, acetylene, ethylene and ethane.
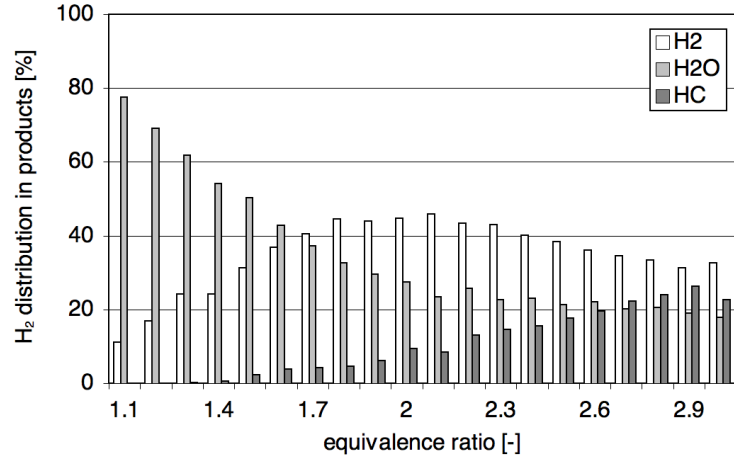
(a)
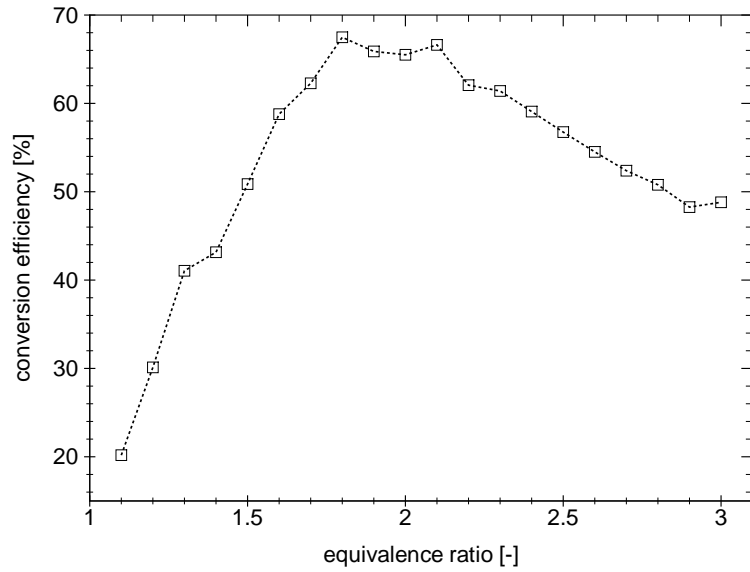
(b)

Figure 3.20: (a) H_2 distribution in hydrogen, water and hydrocarbons present in n-heptane reformate as a function of equivalence ratio based on processing of the measured dry molar fractions. (b) Conversion efficiency defined by Eq. 3.1 against the equivalence ratio for n-heptane. Conditions as in Fig. 3.12.

3.2.3   Porous material effect

This section focus on different porous materials for the reforming stage. Fig. 3.21 compares the experimental results obtained from a similar investigation as the one in Section 3.2.2 (φ ranging from 1.1 to 3.0 at P=7 kW), but carried out in burners A, B, C and D. The only significant enhancement in the reformer performance has been demonstrated by burner D, which uses a packed bed of alumina beads, as demonstrated by Fig. 3.22. The maximum deviation, calculated as the standard deviation of three tests carried out for some conditions, resulted to be $\pm 0.5\%$ vol. from the value reported in the graphs. Therefore, this enhancement is especially meaningful at equivalence ratios higher than φ=2.2. Fig. 3.21 shows a higher molar fraction of H_2 and CO for very rich equivalence ratios, along with a lower hydrocarbon content compared to the foam burners. Specifically, the conversion efficiency peaks at 75% at φ=2.5 with H_2, CO and CO_2 experimental dry molar fractions of 19.3%, 19.9% and 2.3% respectively for burner D, compared to a conversion efficiency of 57.9% and 15.0%, 17.1% and 2.9% molar fractions for burner B, 56.7% and 54.7% for burner A and C respectively (Fig. 3.22) at the same equivalence ratio. The temperatures shown in Fig. 3.23 may aid the understanding of this trend; it appears that the beads lead to higher reforming temperature (by 100 K) compared to the foam matrices. The thermal conductivity of Al_2O_3 is higher compared to ZrO_2, as listed in Table 2.1, and this may enhance the heat recirculation and the superadiabatic effect. Therefore, as shown by the experimental results, higher reforming temperatures lead to a lower presence of HCs in the reformate, resulting in higher H_2 and CO molar fraction. The other parameters such as porosity and foam material (burner A, B and C) seem to not affect appreciably the reformate composition.
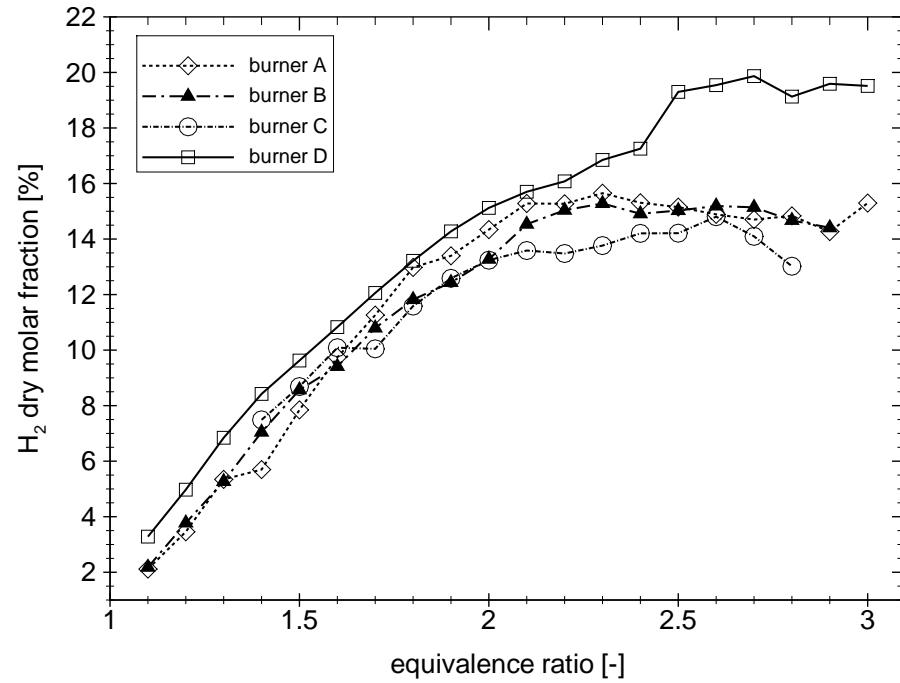
(a)
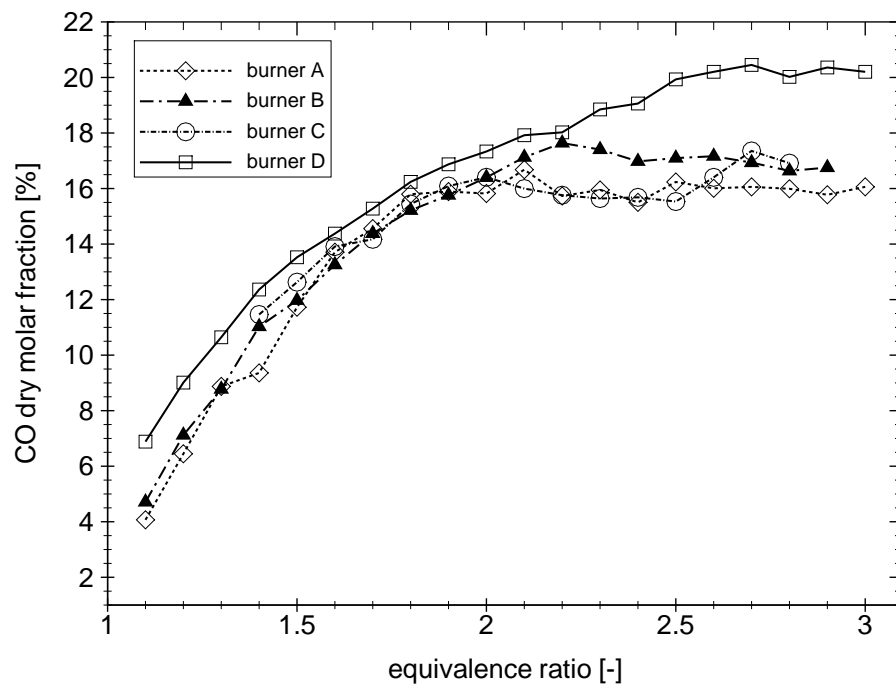
(b)
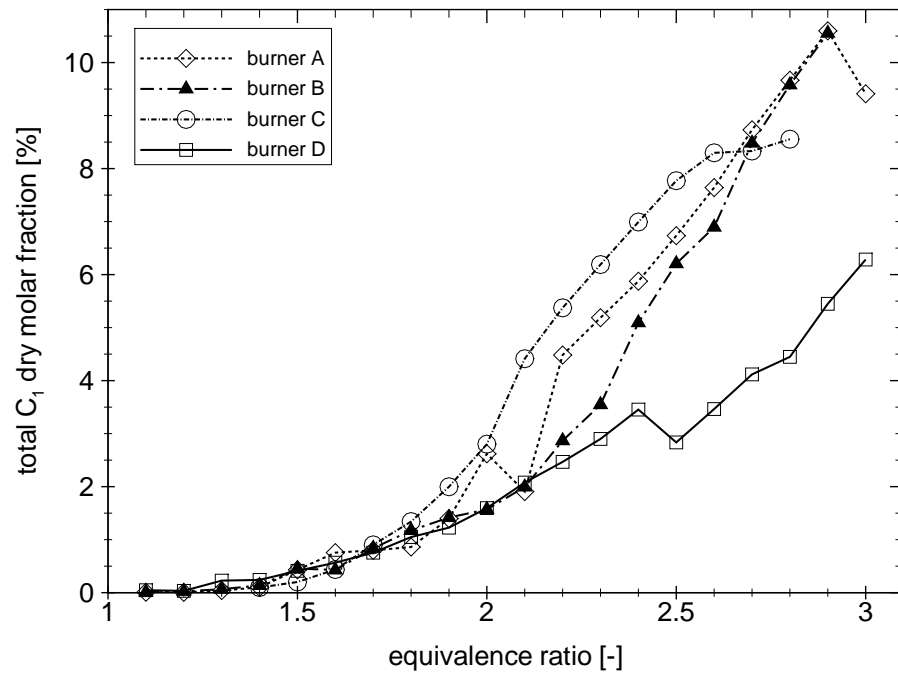
(c)

Figure 3.21: Experimental mole fractions (on a dry basis) of (a) H_2, (b) CO and (c) total C_1 (contributions from CH_4, C_2H_2, C_2H_4 and C_2H_6) for burners A, B, C and D at conditions as in Fig. 3.12.
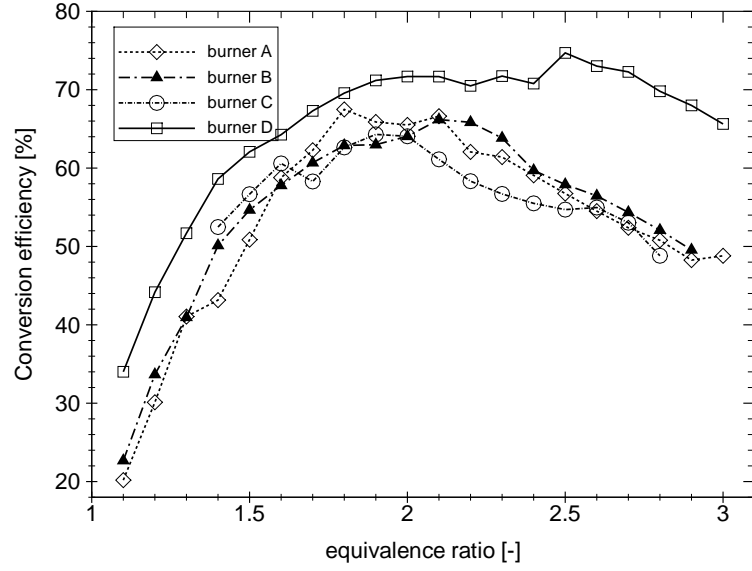
Figure 3.22: Conversion efficiency, as defined by Eq. 3.1, for burners A, B, C and D at conditions as in Fig. 3.12.
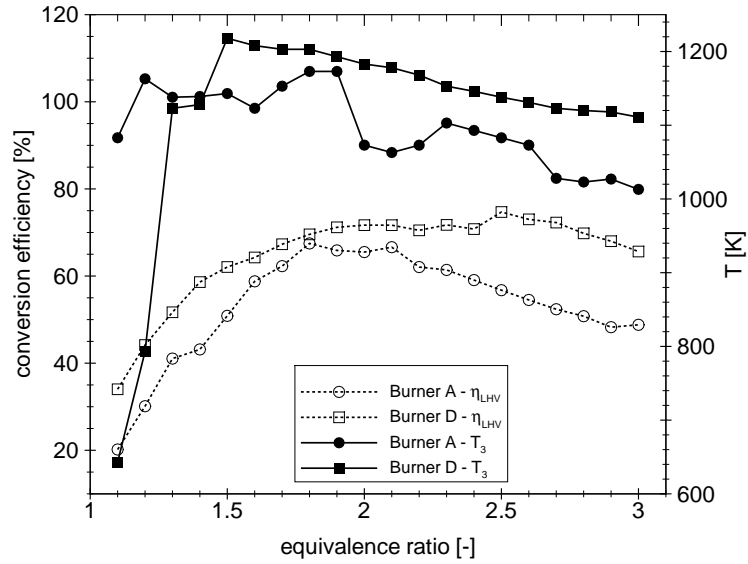
Figure 3.23: Exit temperature (T_3) and conversion efficiency, as defined by Eq. 3.1, for burners A and D at conditions as in Fig. 3.12.

A further investigation on the reforming layer with n-heptane concerns the length of the porous medium. Burners E and F were set for this purpose. The reformate component molar fraction graphs (Fig. 3.24) demonstrate higher values of CO and H_2 and lower molar fraction of C_1 of burner E compared to burner F. This may be due to the larger amount of heat captured and therefore recirculated by a longer matrix, but also to the longer residence time in a hot environment for the partial oxidation products. However, the limited improvement of the performance observed, suggested that any further tests with longer pieces of foam would not be very productive.
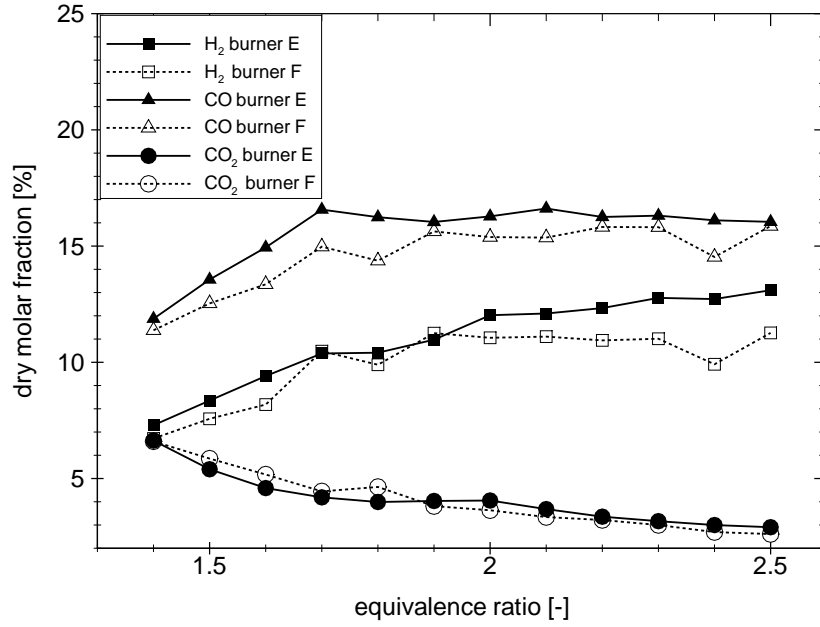
(a)
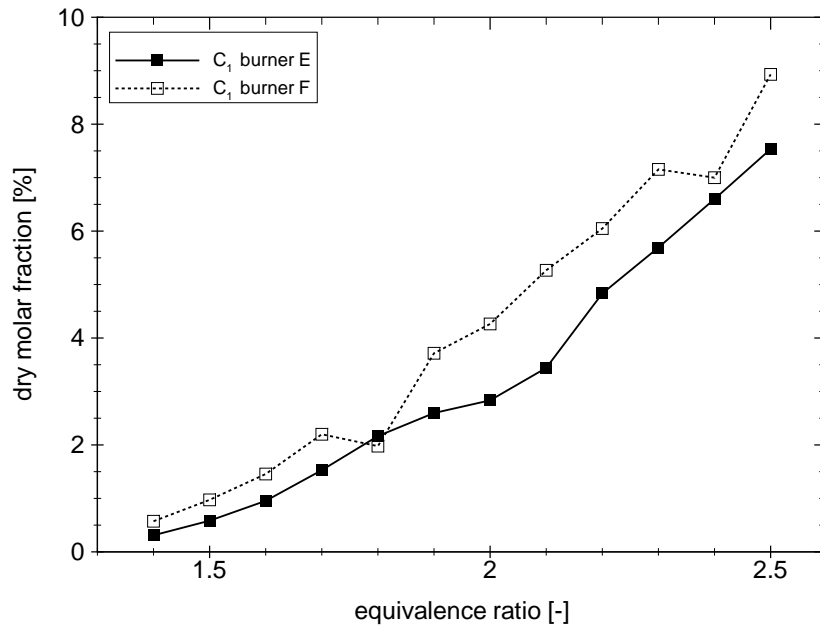
(b)

Figure 3.24: Experimental mole fractions (on a dry basis) for an inlet air/fuel temperature of 423 K at various equivalence ratios for n-heptane reforming at P=7 kW for burners E and F. (a) Hydrogen, carbon monoxide and carbon dioxide. (b) total C_1 (contributions from CH_4, C_2H_2, C_2H_4 and C_2H_6).

83

3.2.4 Burner size effect

The results from the two burners of different diameter have been compared. The same porous material (30 ppi ZrO_2 foam) has been used for the reforming layer. The results are displayed in Fig. 3.25. Hydrogen molar fractions are very similar up to an equivalence ratio of 1.7. For richer equivalence ratios, burner A develops a higher hydrogen presence in the syngas. For CO and CO_2, the trend is the opposite. Burner E shows a higher concentration of carbon monoxide and carbon dioxide compared to burner A up to an equivalence ratio of 1.8. From this point onwards the two curves overlap. This behaviour is mirrored by the C_1 graph, which shows a slight higher hydrocarbon presence in burner E syngas. Since the exit temperatures recorded by the themocouple T_3 are very similar for both burners (Fig. 3.26), a possible reason is a better mixture uniformity in the smaller burner, demonstrated in Section 3.1.1.
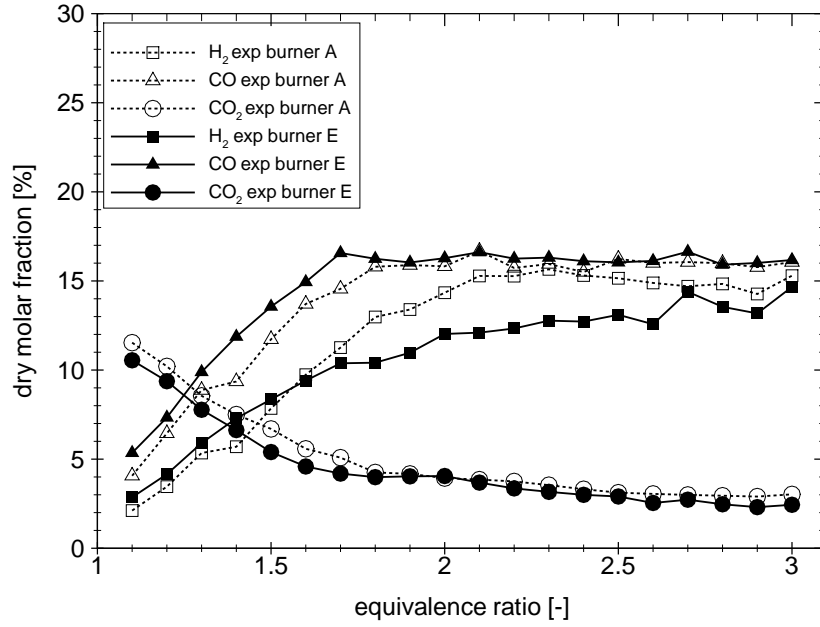
(a)
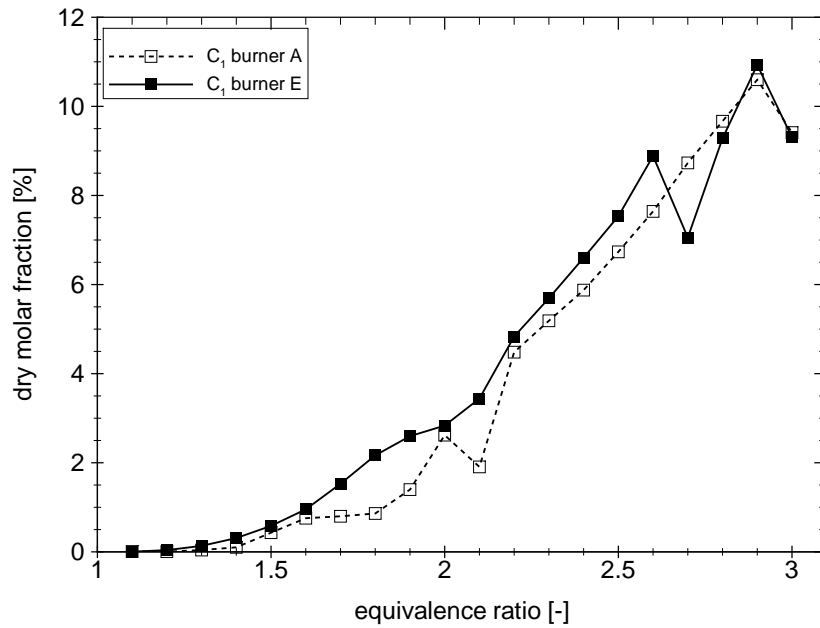
(b)

Figure 3.25: Experimental mole fractions (on a dry basis) for an inlet air/fuel temperature of 423 K at various equivalence ratios for n-heptane reforming at P=7 kW for burners A and E. (a) Hydrogen, carbon monoxide and carbon dioxide. (b) total C_1 (contributions from CH_4, C_2H_2, C_2H_4 and C_2H_6).
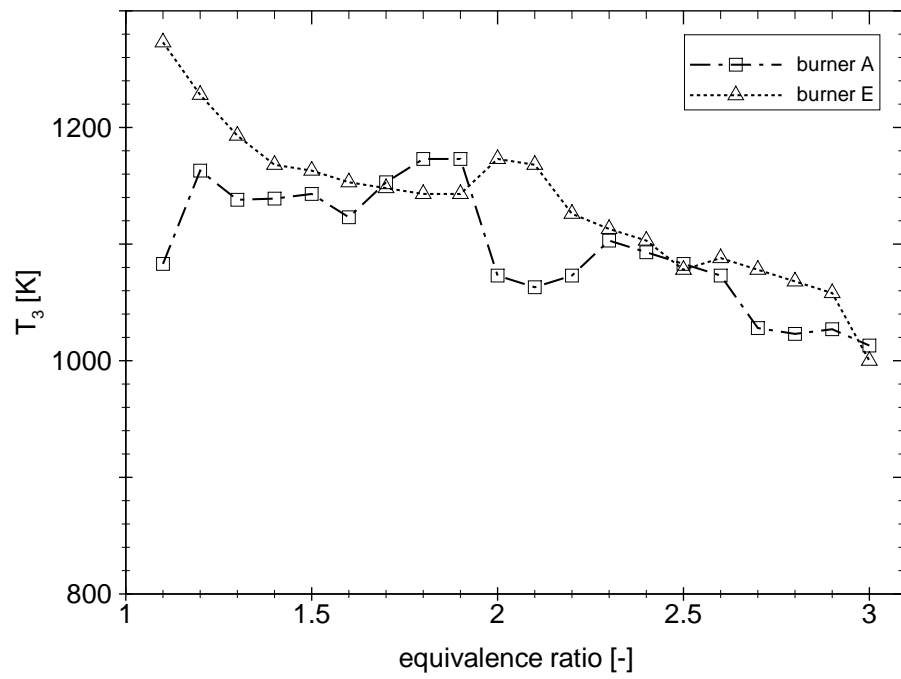
Figure 3.26: Exit temperature (T_3) for burners A and E at condition as in Fig. 3.12.

3.3 Heat losses

Heat losses were assessed by means of a energy balance between the inlet species and the products given by the Gas Chromatograph analyses. For this purpose, the NASA database of species enthalpies has been used. The polynomial fits, calculated at the measured exit temperature, have been used to infer the mixture enthalpy, which has been then multiplied by the molar flow rate of the products. The difference between the energy stored in the reactants and the energy stored in the products gives the energy lost through radiation from the porous matrix at the top of the burner in the downstream direction and through conduction and convection at the outer wall of the reactor. Fig. 3.27 shows the percentage of heat losses versus the thermal power input. At low firing rate the heat losses are around 34% of the energy of the fuel, whereas at higher firing rates this ratio drops to 10%. It is straightforward to devise ways to reduce these heat losses, for example by preheating the atomising air (coil tube wrapped around the burner) or the fuel or to produce steam for a potential syngas clean-up stage.
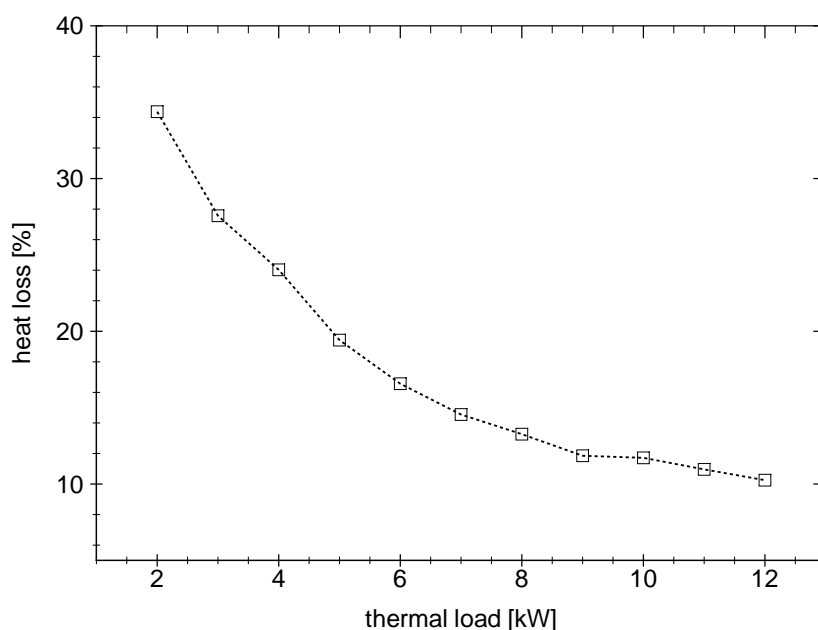
Figure 3.27: Heat losses as a percentage of the thermal load vs. thermal load. Burner A and $\varphi=2.0$.

3.4   Soot emission

The soot emission has been measured with a filter-method machine, as described by Section 2.1.8. The measurement gave the value of the FSN, defined by Eq. 2.1, which is plotted vs. the equivalence ratio in Fig. 3.28. The measurement gives only a value which can be used as a qualitative trend of the particulate formation. No indications about the size and the number of particles can be obtained with this configuration. The trend shows that soot appears at an equivalence ratio of φ=2.0-2.1 and it constantly increases with richer flames. Moreover, burner D presents less particulate emission compared to burner A. The main reason for this difference may be the lower presence of C_2 hydrocarbons for n-heptane reforming in burner D compared to burner A, as highlighted by the comparison between Fig. 3.18b and Fig. 3.12b, since C_2 hydrocarbons are soot precursors [119].
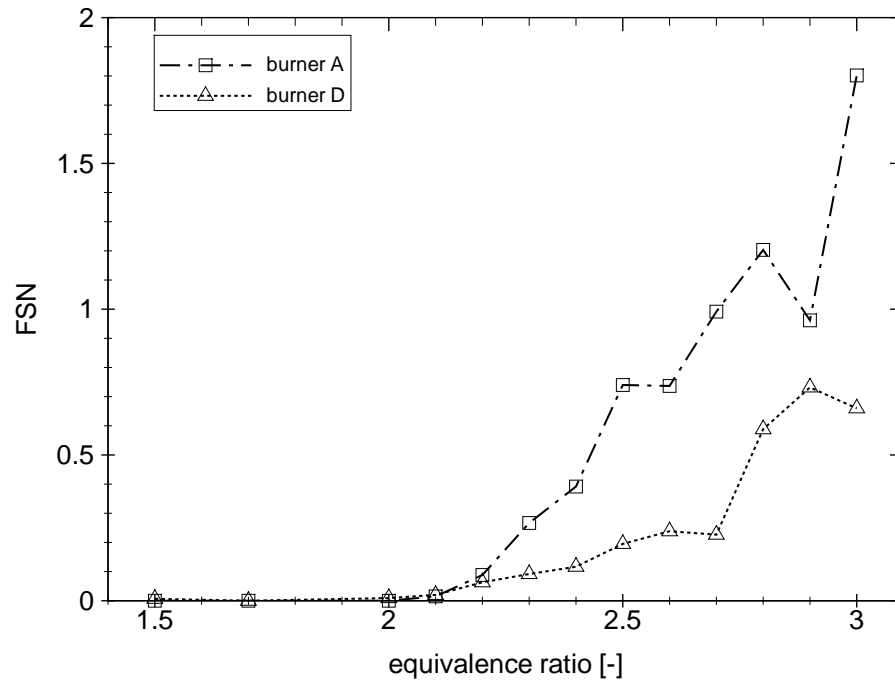
Figure 3.28: Soot emissions measured by a filter-method machine (FSN defined by Eq. 2.1) for n-heptane over a range of equivalence ratio for burner A and D at P=7 kW.

3.5 Discussion

N-heptane reforming to syngas has been investigated by Ellzey et al. [4] through the filtration wave mode and the experimental results may be compared with this work. The porous layer used by those authors was a packed bed of alumina pellets and the comparison with the packed bed of alumina beads (burner D) used in this paper leads to significant similarities. In [4], both the equivalence ratio and the flow velocity (thermal load) effect on the reformer efficiency have been examined. The thermal load impact assessed by [4] matches the trend observed in a previous paper [61]. Pertinent to this work, the equivalence ratio effect described in the previous section is also compatible with the filtration-wave reformer [4] trends. In both investigations, H_2 and CO molar fractions increase steeply with φ, followed by a moderate increase at high equivalence ratios. In [4] CO molar fraction at φ=3.0 was 22% for a flow velocity of 60 cm/s, while in this paper it reaches 20% for a velocity of about 30 cm/s. Ellzey et al. [4] also introduced the hydrogen and carbon monoxide conversion efficiency, defined as the molar flow rate of H_2 and CO over the molar flow rate of the hydrogen and carbon bound in the reactants. Results are very similar with η_{H_2}=75% and η_{CO}=90% and 88% for [4] and this work, respectively. A qualitative soot inspection in [4] revealed a very low soot formation for $1.5<\varphi<2.0$, as stated in the soot emission section of this paper. Therefore the present stable-flame n-heptane reforming at a two-layer porous medium yields similar syngas quality to the filtration wave technique.

As demonstrated in Section 3.2.3, the porous material length affects the syngas characteristics in n-heptane reforming. Numerical simulations [120; 121] suggest that in the partial oxidation reforming the fuel goes through combination of partial and complete oxidation reactions. The water produced downstream drives steam reforming and produces H_2. Also, in [62] this two-stage process is noticed by observing a first quick thermal decomposition of methane, characterized by rapid consumption of oxygen and hydrogen and water formation, followed by the steam reforming of methane reacting with water producing hydrogen and carbon monoxide in an endothermic reaction. The analysis carried out [62] shows that the first stage characteristic time is around 20 ms whereas the steam reformation stage is highly sensitive to temperature and a difference of 300 K leads to a

reaction characteristic time shifting from 10^2 to 10^{-1} s. Being an endothermic process, the presence of a hot and thicker material may enhance this second stage of the reforming process.

3.6   Chapter summary

Various burner sizes, materials, equivalence ratios and thermal loads have been explored for evaluating reforming of n-heptane. Two burners have been tested in order to assess the homogeneity of the n-heptane/air distribution. The 70 mm ID burner demonstrated a good vapour distribution at P=7 kW at φ=2.0, 2.5 and 3.0. The 100 mm ID burner showed a higher difference between the centre and the peripheral area of the cross section, reaching a divergence up to 15% at φ=3.0. However, the syngas composition over the reforming layer for the same burner resulted to be uniform within 10% from the mean value.

The operating points of one foam burner (burner C) has been investigated and it verified the establishment of flame speed higher than the free-flame at the corresponding condition. Moreover, the equivalence ratio of 2.0 resulted to be the broadest steady-flame operating zone.

The parametric investigation (thermal load, equivalence ratio, porous material and burner size) highlighted the close dependency of the conversion efficiency to the process temperature. In all cases, the parameter providing a better heat recirculation and therefore a stronger superadiabatic effect, lead to a condition close to thermodynamic equilibrium. Specifically, a high thermal load and the bead burner (burner D) demonstrated the best performance. Furthermore, the equivalence ratio effect investigation showed a peak in the conversion efficiency around φ=2.0 for the foam burners. From this value onwards, the syngas composition moves away from equilibrium and light hydrocarbons start to be at significant molar fractions. Eventually, the burner size did not affect heavily the reformer output; a slight lower performance of the 100 mm ID burner seems to be due to the lower homogeneity of the mixture distribution.

Finally, the heat losses and the soot emission have been also assessed. The 70 mm ID burner demonstrated a minimum of 10% of the input fuel energy lost by

conduction and radiation and the filter-method machine pointed, qualitatively, to φ=2.0 as the soot limit condition for burner A and D at P=7 kW.

Chapter 4

Diesel, Biodiesel and Kerosene reforming

This chapter deals with the reforming of "real" fuels. The scope of this research was the reforming of commercially-available fuels and the achievement of this target is described in the following sections. Diesel has been reformed at various thermal loads, equivalence ratios and for different burners. Also Jet A-1 Kerosene and RME Biodiesel has been successfully processed in the same reformer as the other fuels.

4.1 Diesel

This section contains the diesel processing results. Commercial grade has been chosen to better demonstrate the feasibility and the performances with the target fuel set for this research.

4.1.1 Thermal load

A thermal load ranging from P=2 to 12 kW has been tested in burner A at a fixed equivalence ratio of φ=2.0. The flame speed corresponded to a range from 15.2 cm/s to 91.3 cm/s and it is higher compared to the n-heptane experiment because of the higher preheat temperature T_1 used (lower density of air). The results are reported in Fig. 4.1. As for the n-heptane experiment in Section 3.2.1, the dry

molar fraction of hydrogen and carbon monoxide increases constantly starting from 5.3% and 10.1% and reaching 14.1% and 18.4% respectively. At the same time carbon dioxide passed from 8.3% at P=2 kW and to 3.8% at P=12 kW. Also the hydrocarbons detected by the FID embedded in the gas chromatograph show a steep drop in their molar fraction. Specifically, as illustrated in Fig. 4.1b, the main components, methane and ethylene, decreased from 1.2% to 0.4% and from 1.1% to 90 ppm respectively. Acetylene and ethane demonstrated a very scarce presence over all the tests.

The conversion efficiency, as defined by Eq. 3.1 and graphically shown in Fig. 4.2, starts from 31.1% at P= 2 kW and reaches 71.1% at P=12 kW. The exit temperature T_3 matches this trend, by peaking at 1300 K for P=12 kW. Similar to the investigation carried out in Section 3.2.1, the distribution of hydrogen in the products has been assessed. As for Eq. 3.2, the percentage of molecular hydrogen present in the products passes from 17.8% to 49.6% at P=12 kW, as depicted in Fig. 4.3. The main issue with diesel reformate analyses is that the sum of the three components (molecular hydrogen, hydrogen in hydrocarbons and hydrogen in water) is around 75% of the total hydrogen contained in the fuel molecule, compared to the 80% obtained with the n-heptane experiments. The possible explanation is the complexity of the diesel molecule, which may lead to the formation of a larger quantity of heavy hydrocarbons compared to n-heptane during the reforming process, which are not detectable by the gas chromatograph. This explanation finds support also from the difference between the total hydrogen contained in the products at low and at high temperatures (i.e. thermal loads). At P=2 kW the sum of the hydrogen spread over the three different components is 71.8%, whereas at P=12 kW is 75.8%. Therefore, it appears that the high temperatures achieved at the maximum thermal load of this test enhance the reaction rates and lead to diesel reforming to "light" components which can be detected by the current configuration.
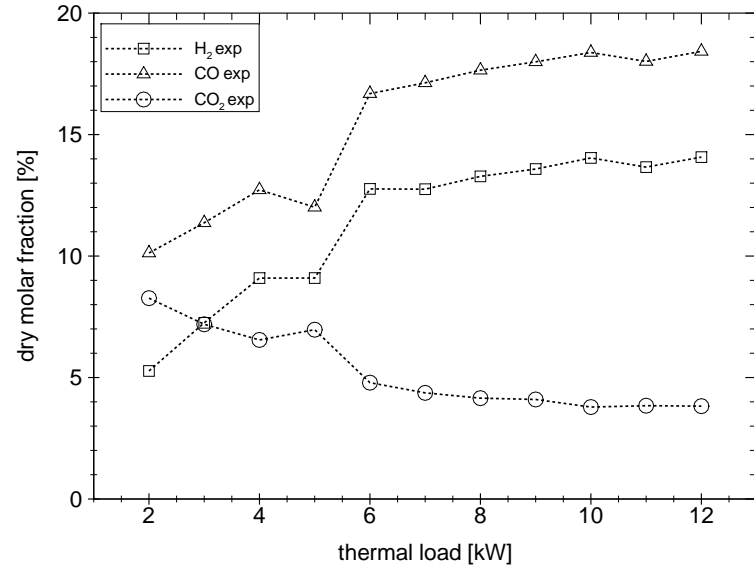
(a)
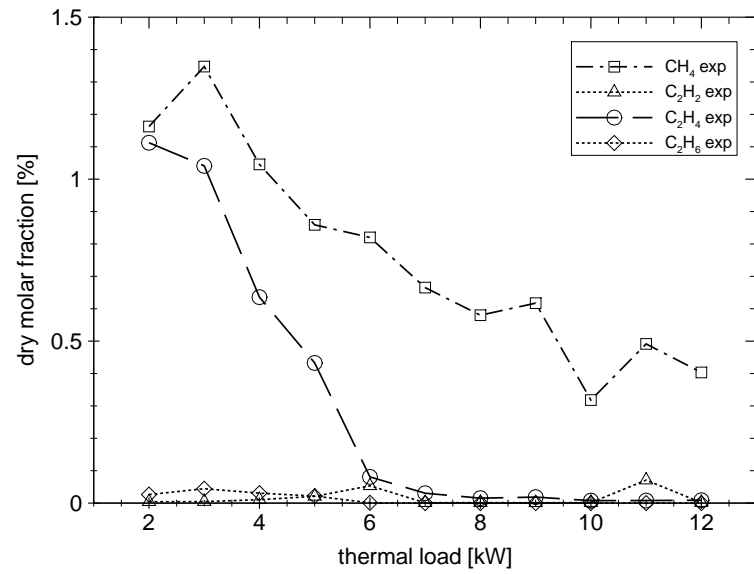
(b)

Figure 4.1: Experimental mole fractions (on a dry basis) for a inlet air/fuel temperature of 573 K at various thermal loads for diesel reforming at $\varphi=2.0$ for burner A. (a) Hydrogen, carbon monoxide and carbon dioxide. (b) Methane, acetylene, ethylene and ethane.
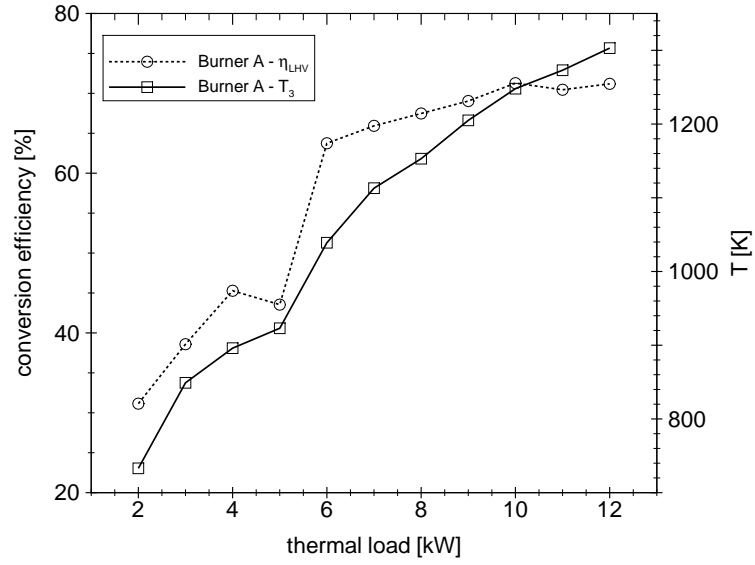
Figure 4.2: Experimental exit temperature T_3 and conversion efficiency for diesel reforming at conditions as in Fig. 4.1.
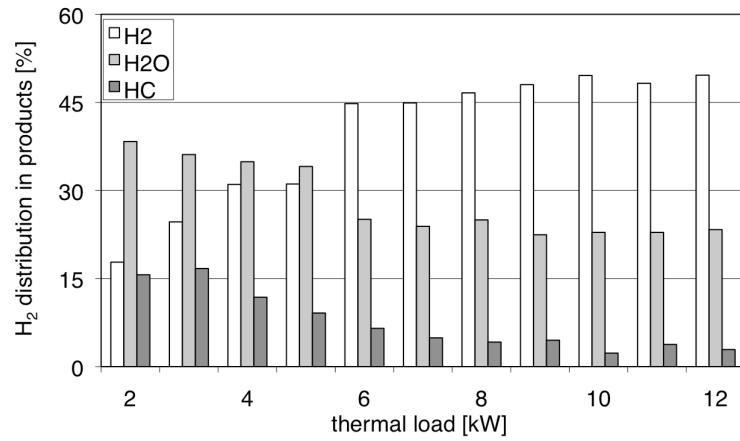
Figure 4.3: H_2 distribution in hydrogen, water and hydrocarbons present in diesel reformate as a function of thermal load based on processing of the measured dry molar fractions. Conditions as in Fig. 4.1.

4.1.2   Equivalence ratio

Burner A and C have been used to test the equivalence ratio effect on the syngas obtained from diesel oil. Burner C has been tested from φ=1.1 to 2.5, while the investigation on burner A has been extended up to φ=3.0. Steps of 0.1 were taken and the analyses of the gas samples gave the results depicted in Fig. 4.4 and Fig. 4.5. Both burners presented a similar trend, also equivalent to the n-heptane reforming results. However, diesel reformate presents higher molar fraction values of CO and lower molar fraction values of H_2. This difference is due to the different H/C ratio of the two fuels (2.28 for C_7H_{16} and 1.92 for $C_{12}H_{23}$). Specifically to diesel reformate, H_2 and CO peak at φ=2.5 with molar fraction values of 14.5% and 18.4% respectively and similarly the molecular hydrogen in the products over the hydrogen contained in the reactants ratio (Eq. 3.2) peaks at φ=2.4 with a value of 43.5%, as shown in Fig. 4.6a. The conversion efficiency peaks at φ=2.0 with a value of η_{LHV}=62.7% (Fig. 4.6b) and H_2, CO and CO_2 experimental dry molar fractions reach values of 12%, 16.6% and 4.8% respectively at this point.

For richer values of φ, the performance drops steeply, as demonstrated by burner A, and a red flame has been detected on the top of the porous material. In Fig. 4.7 a quartz tube has been put over the stainless steel tube to visualize better this effect for Diesel reforming at P=7 kW and φ=3.0. In the picture a red flame coming out from the burner can be noted. It is not due to air entrainment and it is not a filtration wave reaching the top of the foam as the flame resulted being stabilized at the layer interface. The preheat temperature T_1 has been raised up to 773 K, by circulating the oxidative air only through the coil wrapped around the tube, in the attempt to raise the overall reaction temperatures, but no enhancements have been noticed. Furthermore, this effect was associated with a steep increase in the soot emission, as demonstrated by Section 4.4. The reason of this event is not clear, but it seems to be associated with the production of heavy hydrocarbons in the reforming process, which partially oxidize only at the exit of the burner. It can also be due to high radiation from the particles emitted. An investigation with the aid of a spectrometer would confirm one of these assumptions. Moreover, once the fuel flow has been stopped, the air flowing

in the hot porous matrix lead to the oxidation of deposits inside the reforming layer and a flame was still present for 20-30 seconds more.

A further distinction between n-heptane and diesel reforming in burner A is the different path taken by the light hydrocarbon formation. n-heptane presents higher concentrations of acetylene compared to ethylene, whereas for diesel (but also for Jet A-1 and Bio-diesel, as it will be shown in the following sections) ethylene is higher than acetylene.
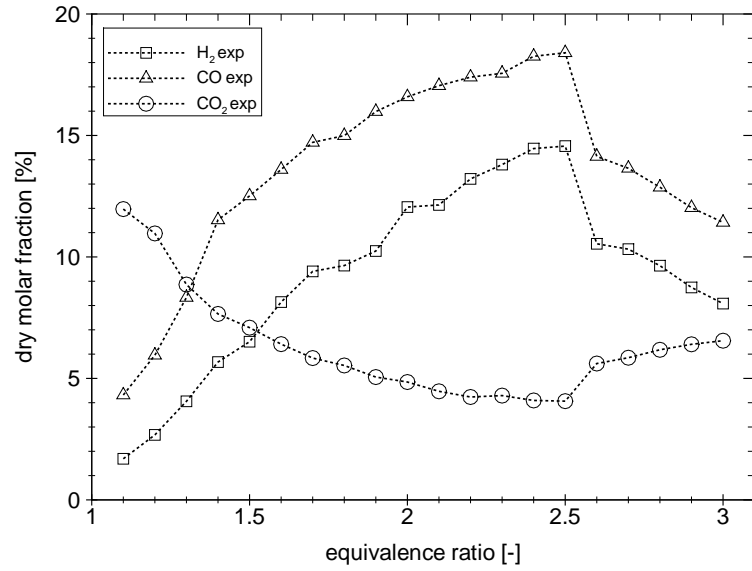
(a)
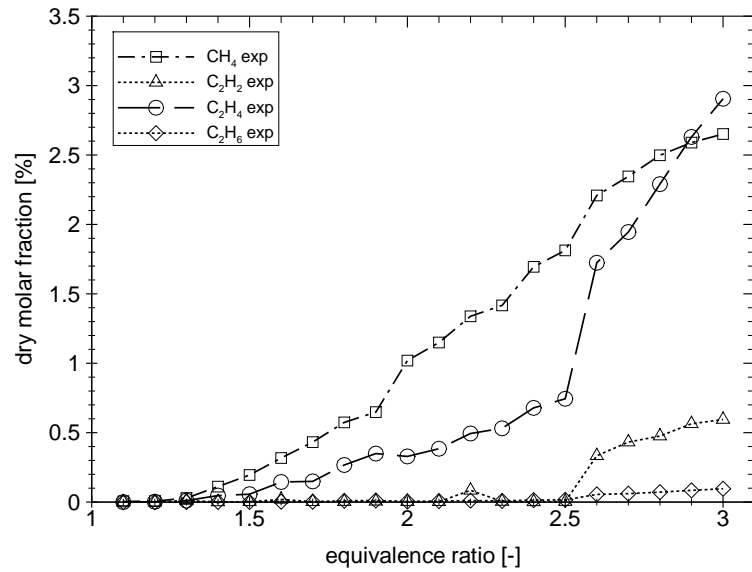
(b)

Figure 4.4: Experimental mole fractions (on a dry basis) for a inlet air/fuel temperature of 573 K at various equivalence ratio for diesel reforming at P=7 kW for burner A. (a) Hydrogen, carbon monoxide and carbon dioxide. (b) Methane, acetylene, ethylene and ethane.
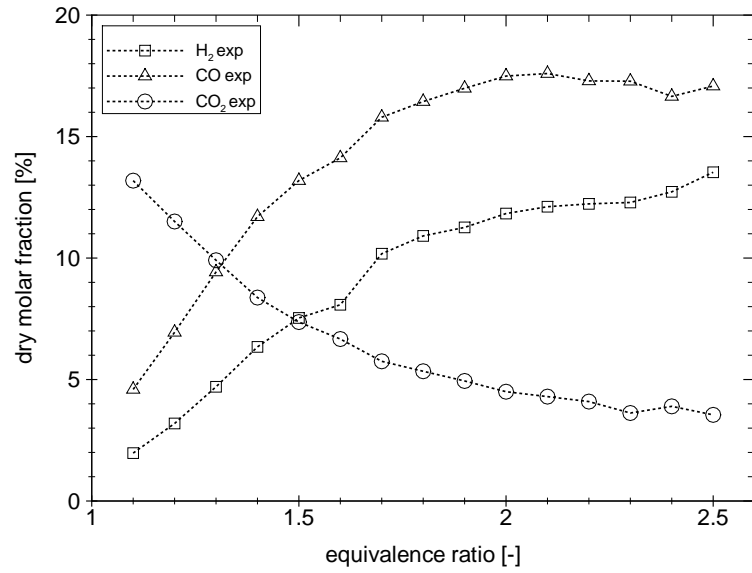
(a)

(b)

Figure 4.5: Experimental mole fractions (on a dry basis) for a inlet air/fuel temperature of 573 K at various equivalence ratio for diesel reforming at P=7 kW for burner C. (a) Hydrogen, carbon monoxide and carbon dioxide. (b) Methane, acetylene, ethylene and ethane.
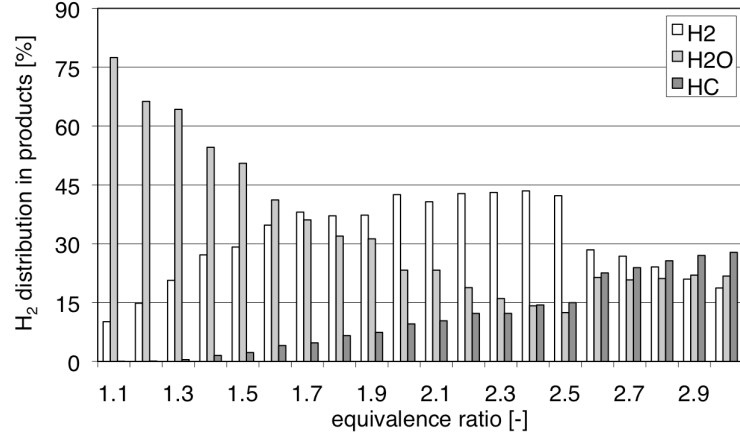
(a)
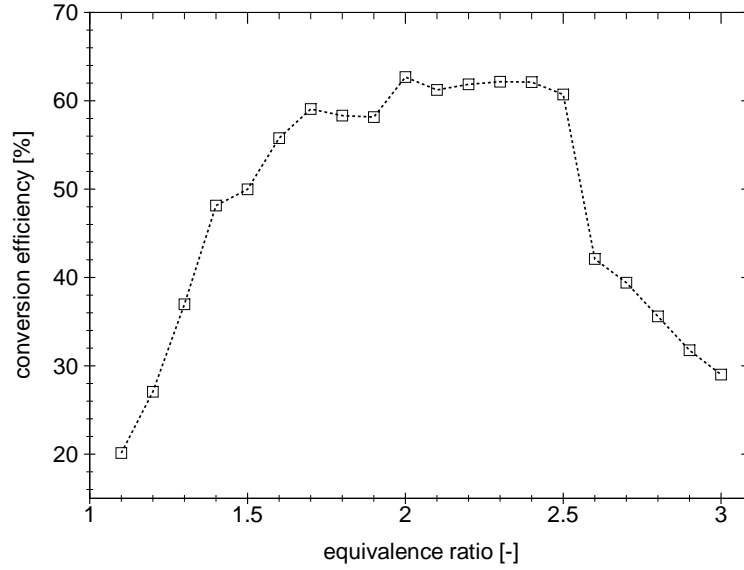
(b)

Figure 4.6: (a) H_2 distribution in hydrogen, water and hydrocarbons present in diesel reformate as a function of equivalence ratio based on processing of the measured dry molar fractions. (b) Conversion efficiency defined by Eq. 3.1 against the equivalence ratio for diesel. Conditions as in Fig. 4.4.

Figure 4.7: Flame on the top of the reforming layer of burner A in diesel reforming at P=7 kW and φ=3.0.

4.1.3   Porous material effect

The test performed in the previous section has been repeated in burner D (Al_2O_3 beads). The trend shown in Fig. 4.8 demonstrates a similar behaviour to the one observed for n-heptane reforming. The syngas quality is enhanced and the curves describing H_2 and CO molar fractions increase monotonically in this configuration, leading to a higher conversion efficiency for φ richer than 2.5 compared to those exhibited by burner A (Fig. 4.9) at these rich values. The broadest difference between burner A and D has been recorded at φ=2.8. At this condition, burner A presents a dry molar fraction of hydrogen and carbon monoxide of 9.6% and 12.9% respectively, whereas burner D gives 13.7% and 18.1% respectively. The conversion efficiency passes from 35.6% to 53.8% switching from the Zirconia foam burner to the Alumina beads reactor at this equivalence ratio.

In the previous section, a test run in burner C has been mentioned. It demonstrated similar molar fractions to the ones obtained in the Zirconia burner. The foam burners showed again no significant difference in the syngas composition, even for different materials.
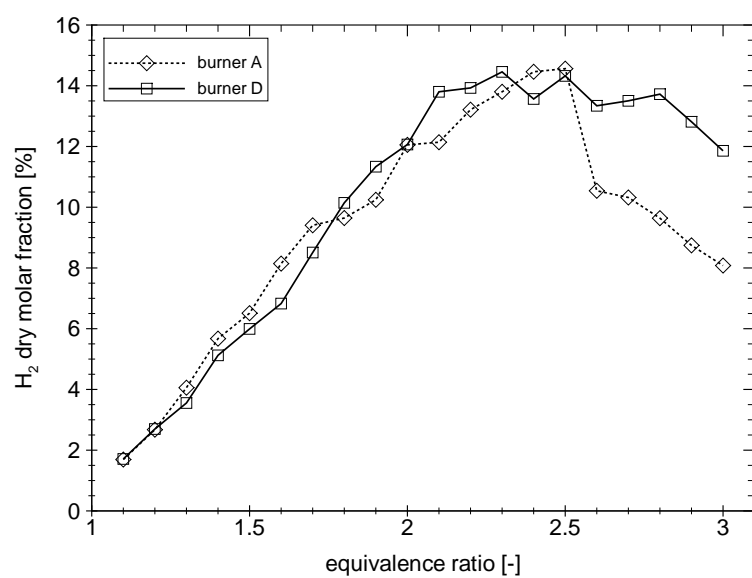
(a)
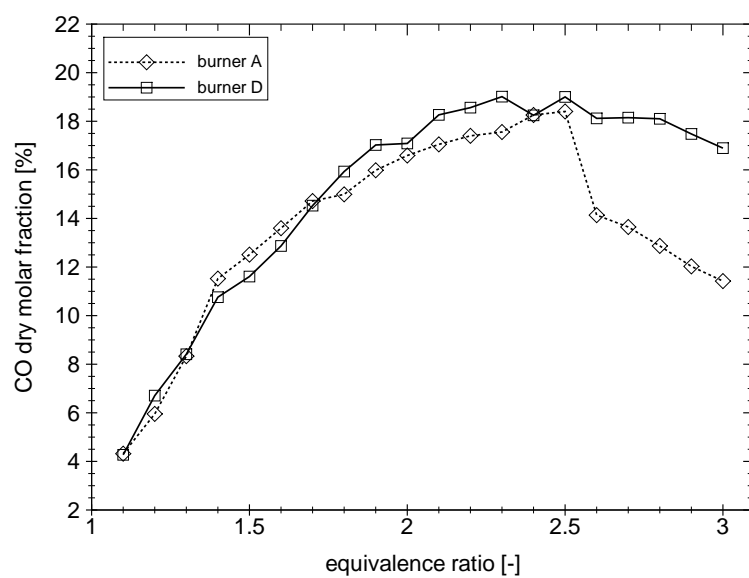
(b)
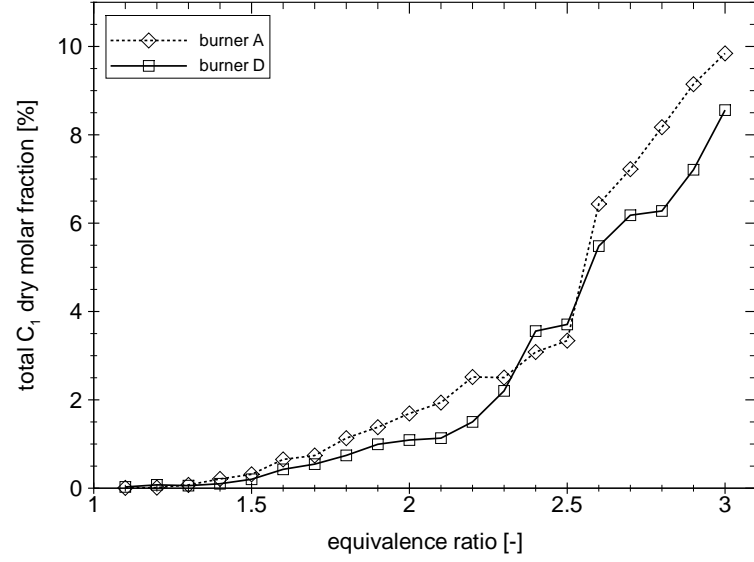
(c)

Figure 4.8: Experimental mole fractions (on a dry basis) of (a) H_2, (b) CO and (c) C_1 (contributions from CH_4, C_2H_2, C_2H_4 and C_2H_6) for burner A and D at conditions as in Fig. 4.4.
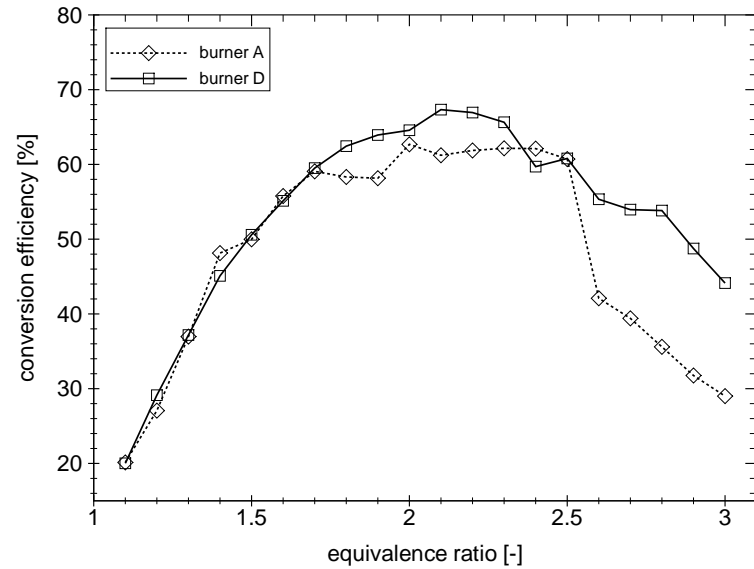
Figure 4.9: Conversion efficiency, as defined by Eq. 3.1, for burners A and D at condition as in Fig. 4.4.

4.1.4   Heat losses

The heat losses have been assessed using the syngas composition and exit temperature data from Section 4.1.1. The energy lost has been calculated through the difference between the energy stored in the reactants and the energy stored in the products, analogously to the procedure explained in Section 3.27. Fig. 4.10 outlines the percentage of heat losses versus the thermal power input. At low firing rate the heat losses are around 41% of the energy of the fuel, whereas at higher firing rates this ratio drops to 16%. The difference with the same investigation performed on n-heptane is maybe due to the less accurate carbon balance between reactants and products, as explained in Section 4.1.1. The missing species may account for the energy difference in the heat losses analyses between n-heptane and diesel.
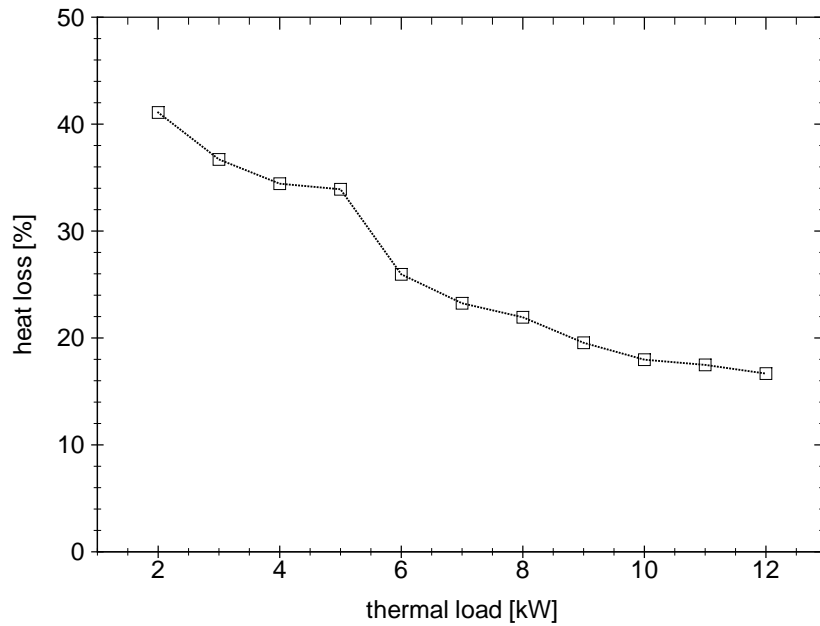
Figure 4.10: Heat losses for burner A for a thermal load ranging from P=2 to 12 kW and φ=2.0 at condition as in Fig. 4.4.

4.1.5 Endurance test

An endurance test has been carried out in burner A at P=7 kW and φ=2.0. The burner demonstrated a steady global behaviour over the test, showing no oscillation in flows and flame position. The test lasted 150 minutes and gas samples were extracted every 30 minutes, which is the time needed by the GC to process one sample. The results are shown in Fig. 4.11. The variation of hydrogen, carbon monoxide and carbon dioxide are limited to 8% from the average value. After 60 and 150 minutes the biggest divergence from the average value is detected. The hydrocarbons also presents a consistent trend, especially for methane and ethylene which are the main HC detected in the gas samples. Consequently, the conversion efficiency results stable around an average value of 63%, as displayed in Fig. 4.12.
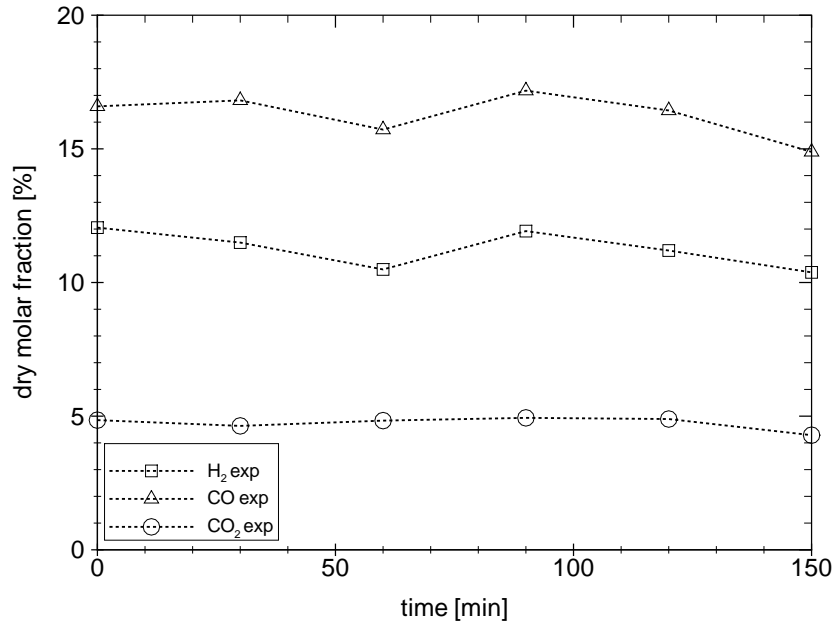
Figure 4.11: H_2, CO and CO_2 experimental dry molar fractions of diesel reforming at P=7 kW and φ=2.0 over time at condition as in Fig. 4.4.
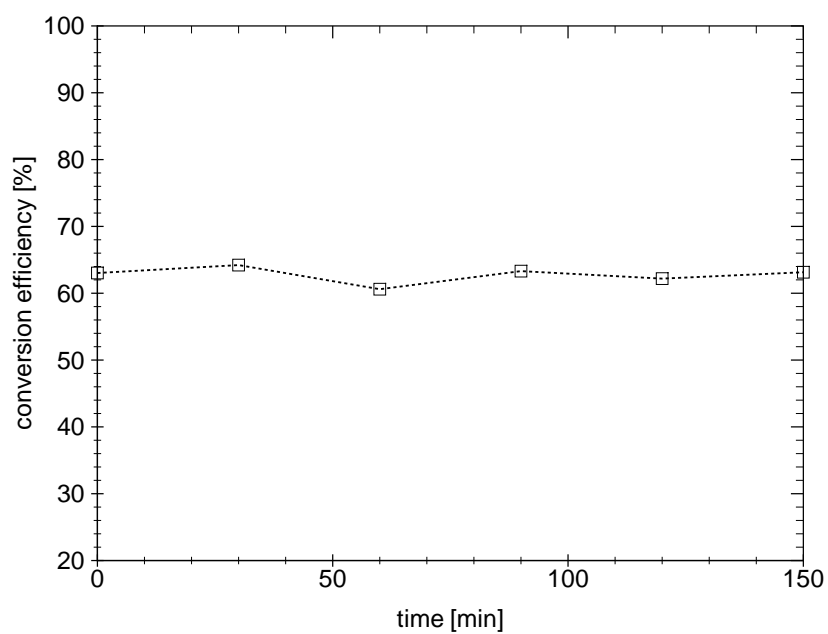
Figure 4.12: Conversion efficiency of diesel reforming at P = 7 kW and φ=2.0 over time at condition as in Fig. 4.4.

4.2   Biodiesel

RME biodiesel has also been tested. The equivalence ratio effect has been investigated up to φ=3.0 for a thermal load of P=7 kW in burner A. The results are shown in Fig. 4.13. Biodiesel data show a similar behaviour compared to diesel reforming. H_2 and CO dry molar fractions keep increasing up to φ=2.3 and then the performance decreases considerably. Consequently, the conversion efficiency resulted maximum at φ=2.2 with η_{LHV}=64.9% with H_2, CO and CO_2 experimental dry molar fractions reaching values of 14.0%, 19.1% and 4.4% respectively. The same test has been run in burner C. Fig. 4.14 shows the results, which are comparable with burner A. Burner A provided higher syngas quality between 2.2<φ<2.7 with conversion efficiencies higher than about 10% in this range (Fig. 4.15). The HCs presence in the reformate is different compared to diesel and n-heptane. The difference is the much higher molar fraction of hydrocarbons at very rich equivalence ratio but also the predominant presence of ethylene at φ higher than 2.7. This trend, together with the lower hydrogen and carbon monoxide yield compared to other fuels, shows the complexity in the reforming mechanism of heavy fuels.

The biodiesel test showed a shifted stability range towards richer equivalence ratios compared to the other fuels investigated. Specifically, the flame managed to penetrate the flame holder layer up to φ=1.7 in burner C and φ=1.8 in burner A. The mechanism leading to this differing behaviour is not clear and it may due to different kinetics paths taken by an oxygenated fuel like biodiesel compared to diesel or kerosene during the pre-ignition reactions.
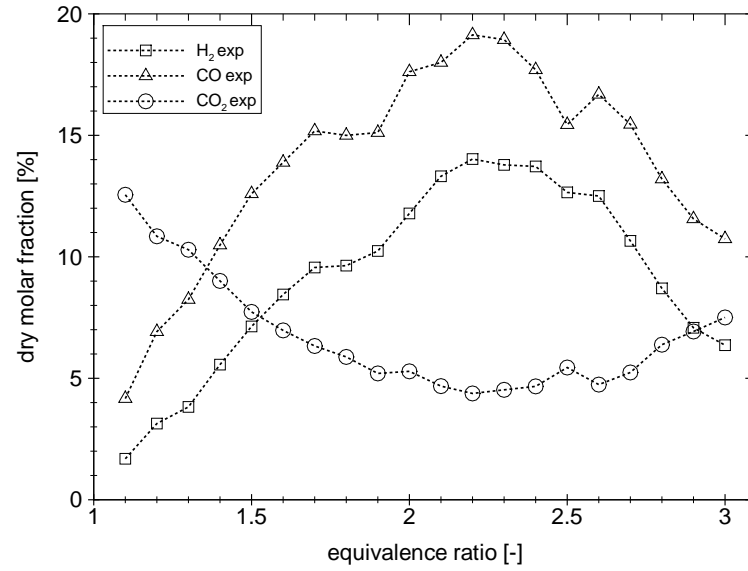
(a)
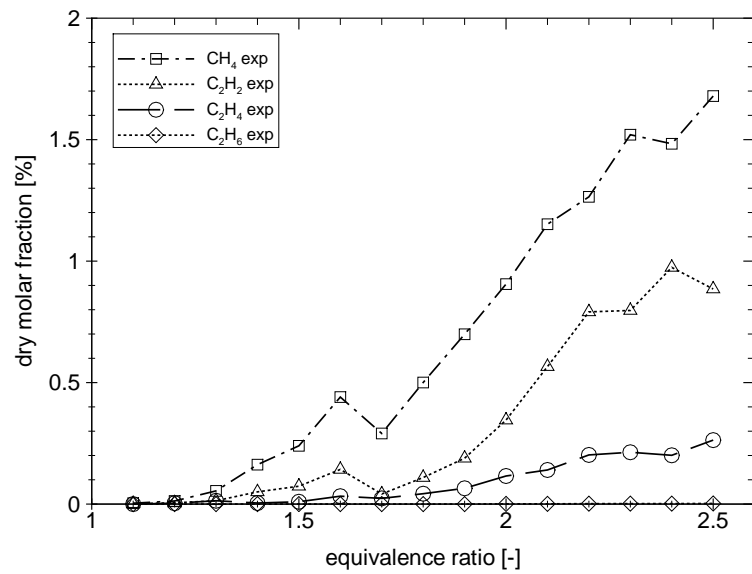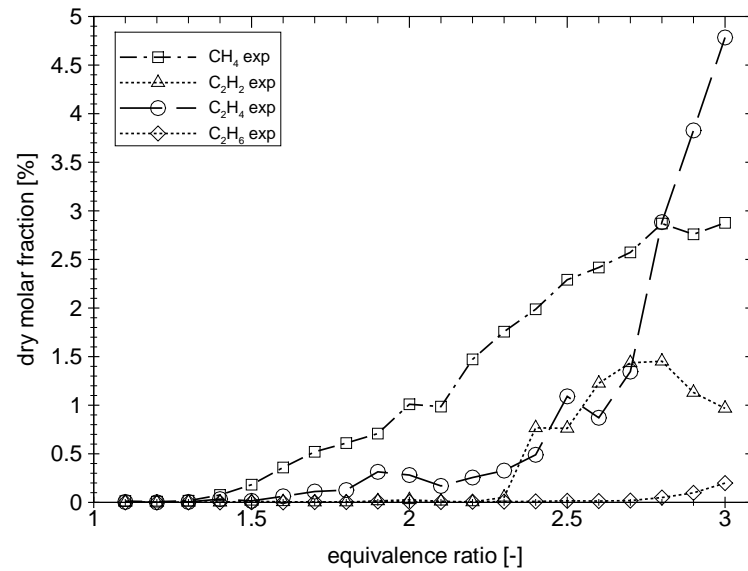

(b)

Figure 4.13: Experimental mole fractions (on a dry basis) for a inlet air/fuel temperature of 523 K at various equivalence ratio for RME biodiesel reforming at P=7 kW for burner A. (a) Hydrogen, carbon monoxide and carbon dioxide. (b) Methane, acetylene, ethylene and ethane.
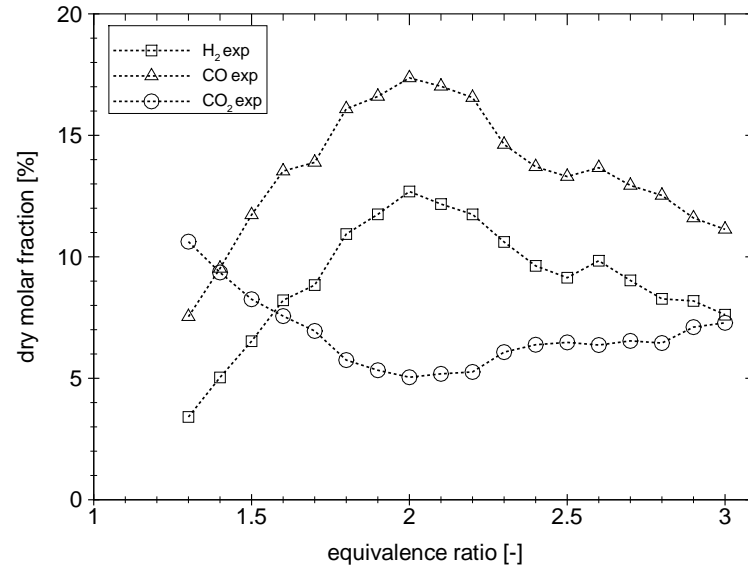
(a)
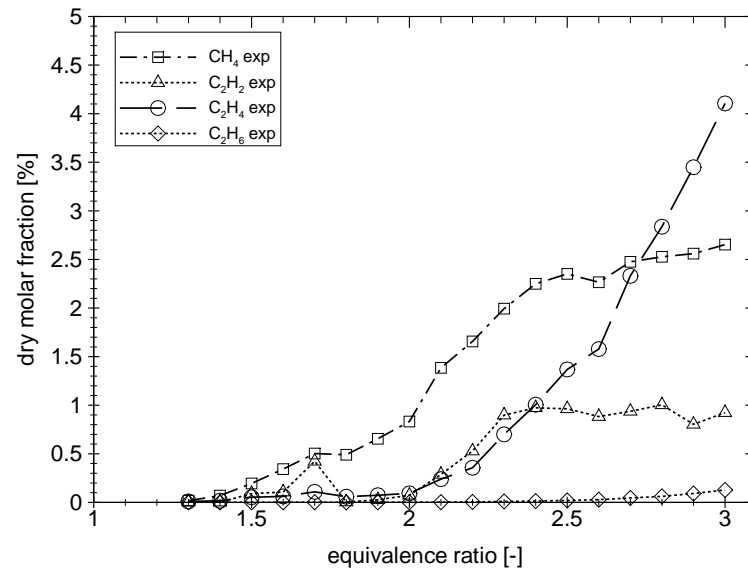
(b)

Figure 4.14: Experimental mole fractions (on a dry basis) for a inlet air/fuel temperature of 523 K at various equivalence ratio for RME biodiesel reforming at P=7 kW for burner C. (a) Hydrogen, carbon monoxide and carbon dioxide. (b) Methane, acetylene, ethylene and ethane.
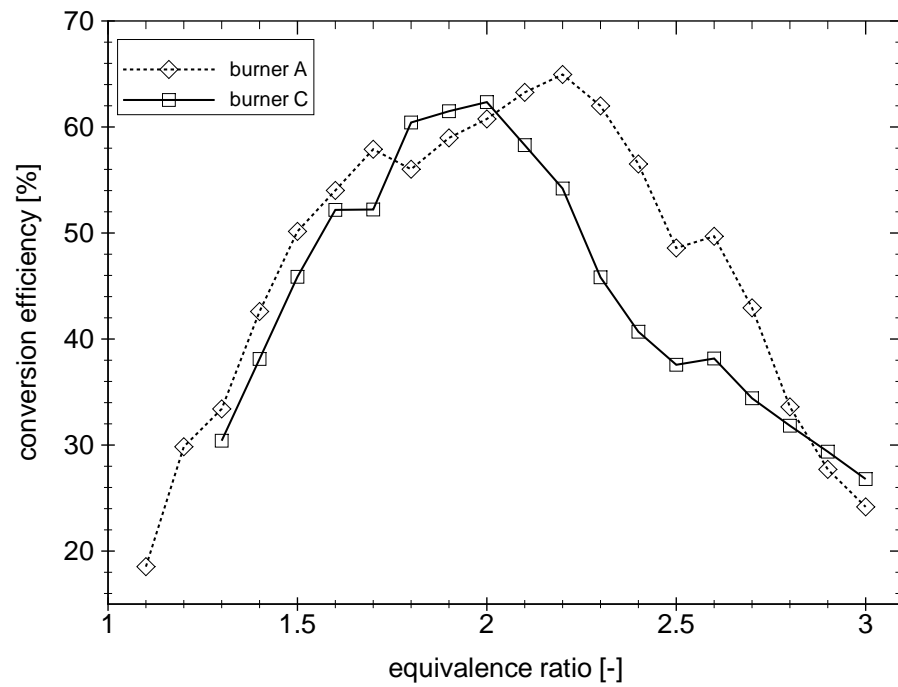
Figure 4.15: Conversion efficiency, as defined by Eq. 3.1, for biodiesel reforming in burners A and C at condition as in Fig. 4.13.

4.3   Kerosene

Finally kerosene has been reformed, at P=7 kW, up to an equivalence ratio of 3.0. For this fuel, only burner A has been tested. The conversion efficiency, shown in Fig. 4.16, peaks at φ=2.1 with the value of η_{LHV}=69.6% and H_2, CO and CO_2 experimental dry molar fractions reach values of 13.8%, 18.9% and 3.2% respectively. The reformate composition follows closely the calculated equilibrium data up to φ=2.0 and afterwards the presence of hydrocarbons in the experimental results lead to a divergence between the curves. It is noted that the experimental CO molar fraction follows equilibrium closely up to φ=2.3. After a peak of H_2 and CO at φ=2.5, the molar fractions start to decrease, as described also from the equilibrium calculations. The equilibrium calculations could not go beyond φ=2.9, because the adiabatic flame temperature of $C_{12}H_{24}$ with enthalpy of formation at 298.15 K of -383.894 kJ/mol [122] could not be calculated by the method used for this project [116].

This fuel presented a very low concentration of HCs in the reformate and most of the molecular hydrogen missing from the equilibrium calculation data is stored in CH_4, with very low concentration of C_2 species. Specifically, at φ=3.0 the maximum content of light hydrocarbons has been detected, with 2.9% methane, 0.12% of acetylene and 0.65% and 50 ppm of ethylene and ethane respectively. Also for this fuel ethylene is predominant over the acetylene molar fraction.
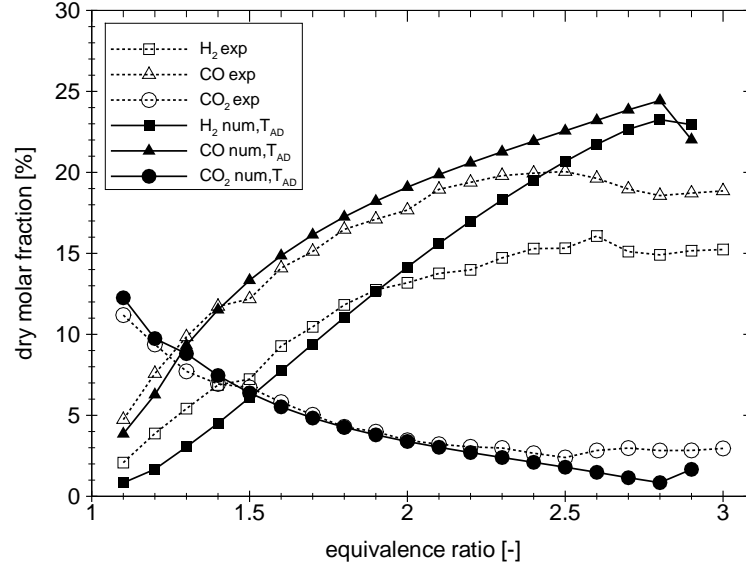
(a)
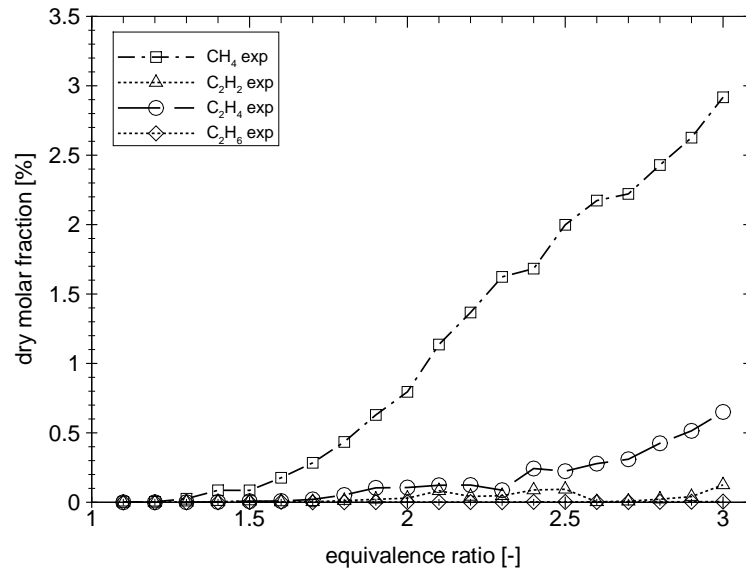
(b)

Figure 4.16: Calculated equilibrium at the adiabatic flame temperature and the experimental mole fractions (on a dry basis) for a inlet air/fuel temperature of 523 K at various equivalence ratio for Jet A-1 kerosene reforming at P=7 kW for burner A. (a) Hydrogen, carbon monoxide and carbon dioxide. (b) Methane, acetylene, ethylene and ethane.

4.4 Soot emission

Fig. 4.17 gives an indication of the soot content in the sample for the three different fuels described in this chapter, at P=7 kW for burner A at different equivalence ratios. The graph represents a qualitative comparison between the fuels and the soot emission trend, rather than a quantitative evaluation of the particulate properties (soot number and size) at the different conditions considered. The main considerations drawn from the graph are, first, that soot starts to appear in the sample above φ=2.0-2.1 for all fuels tested. Secondly, diesel presents the highest FSN value and hence the largest particulate emission, as expected. Finally, note the low soot generation observed in biodiesel reforming. This trend is maybe due to the presence of oxygen atoms in the fuel molecule, which lowers the rate of particulate formation.
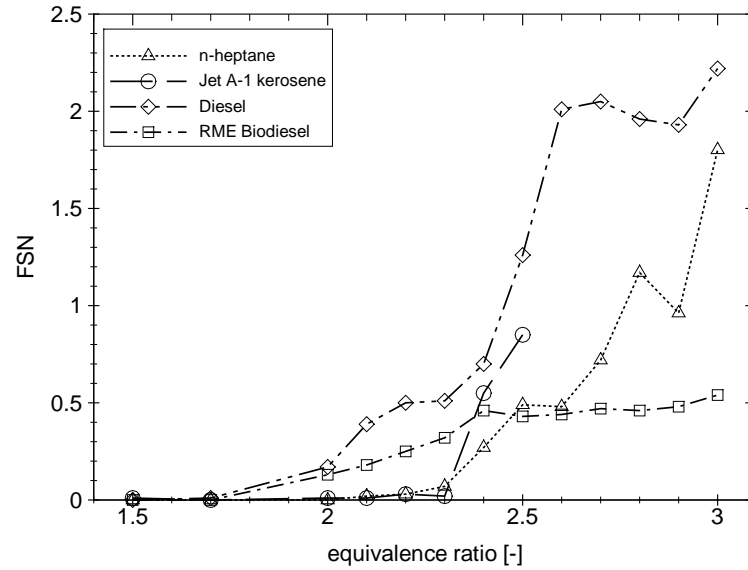
Figure 4.17: Soot emissions measured by a filter-method machine (FSN defined by Eq. 2.1) for n-heptane, Diesel oil, Jet A-1 Kerosene and Biodiesel over a range of equivalence ratio for burner A at P=7 kW.

4.5   Discussion

Comparing the results from the three fuels tested in this Chapter, the following comments can be drawn. The total C_1 molar fraction, as contribution from CH_4, C_2H_2, C_2H_4 and C_2H_6 of diesel, kerosene and biodiesel is shown in Fig 4.18. The trend is similar for the three fuels up to φ=2.3. From this value onwards, higher presence of HC is observed in biodiesel reformate. The complexity of the fuel molecule seems to play the major role in the reforming mechanism, probably because of the different components present in the fuel molecule as previously shown in the GC-MS outputs (Figs. 2.8, 2.9 and 2.10), leading to a high sensitivity of the reformate composition to the process temperature. Consequently, the conversion efficiency is slightly different for the three fuels. η_{LHV} of the three fuels is compared in Fig. 4.19. The graph shows similar trends and values, with kerosene demonstrating a higher performance compared to diesel and biodiesel. As demonstrated previously, the higher hydrogen and carbon monoxide yield is in kerosene reforming, together with a low HCs emission, lead to the highest performance among the fuels over all the equivalence ratio investigated.
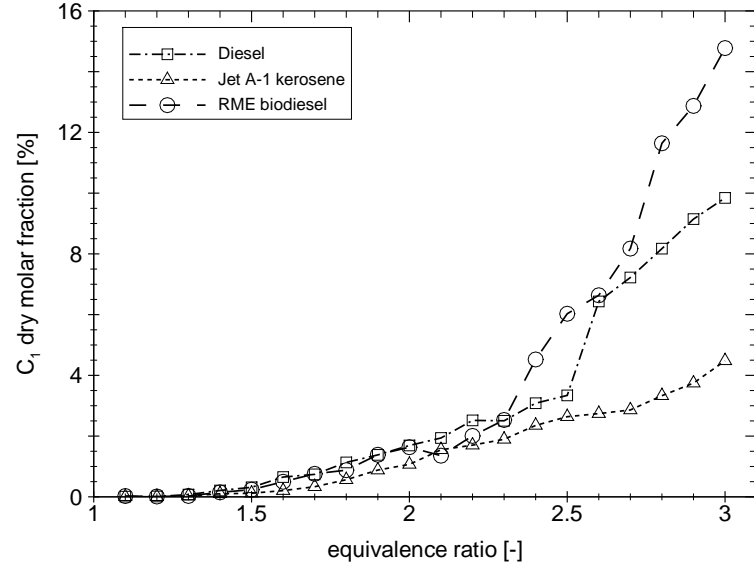
Figure 4.18: Experimental mole fractions (on a dry basis) of C_1 (contributions from CH_4, C_2H_2, C_2H_4 and C_2H_6) for burner A at P=7 kW for diesel, biodiesel and kerosene.
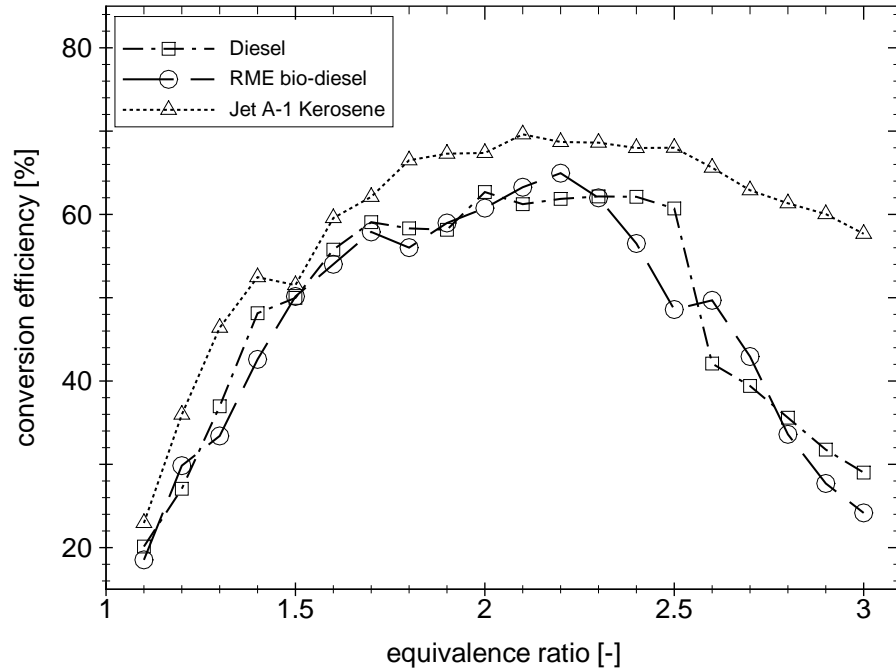
Figure 4.19: Conversion efficiencies of kerosene, diesel and RME biodiesel reforming, as defined by Eq. 3.1, at P=7 kW for burner A.

Diesel thermal partial oxidation has been studied experimentally in Ref. [123]. That experimental setup differs in the vaporization stage, reforming stage and in the ignition strategy. The vaporizer in [123] is a separated section from the rest of the reactor, the porous matrix is a single layer and the igniter is on the top of the burner. A ZrO_2-10 ppi foam has been implemented in [123], whereas different dimensions and a porosity of 30 ppi was used in this paper. The operational differences occur in the preheat temperature and the thermal load (873.15 K and P= 10.5 kW in [123]). Despite these differences, comparable results were achieved: the maximum H_2 and CO concentration was obtained at φ=2.2 with a molar fraction of 16.0% and 18.5% respectively. As previously shown in Section 3.2, we obtained maximum hydrogen and carbon monoxide molar fraction at φ=2.5 with values of 14.5% and 18.4% respectively. The small difference from the results of [123] is possibly due to the lower thermal load and the lower preheat temperature used in this investigation, which lead to slower reaction rates of the reforming process.

A catalytic partial oxidation reformer has been developed by [124] for an APU system embedded with a SOFC. The authors obtained a conversion efficiency of 78% for a thermal load of 6 kW and φ=2.5, compared to 60% efficiency obtained in this project for reforming in burner D at P=7 kW and at the same equivalence ratio. A staged injection (a first lean oxidation followed by a second fuel stream injected in the hot off-gas without any additional air) is implemented to provide the system with the heat necessary to the fuel evaporation and catalytic bed heating. Another experimental demonstration of CPOX of ethanol, isooctane, hexadecane, synthetic JP8, desulfurized kerosene and desulfurized diesel for solid oxide fuel cell applications has been performed by [59]. The results obtained by desulfurized diesel reforming at φ=2.2 are H_2=25%, CO= 18% and CO_2=3%. It can be noted that, apart from hydrogen, the results are similar to the results obtained by burner D. The catalytic activity may enhance the production of hydrogen, which in this research resulted being "trapped" in the light hydrocarbons and water.

Many other published works on diesel reforming focus on ATR of diesel oil and its surrogates, highlighting the sensitivity of catalysts to the temperature profile of the reactor and to the poisoning species (sulfur) and the degradation of the

catalytic bed with time. In [125], a noble metal catalyst has been used to reform hexadecane and commercial diesel in an ATR reformer. The experimental results show molar fractions of H_2, CO, CO_2 and CH_4 of 53%, 25%, 18% and 3.2% respectively, for commercial diesel reforming in a furnace kept at 850 °C. Further energy was needed to produce the large amount of steam used to run the steam reforming stage of the autothermal process and the WGS reaction. Synthetic diesel (sulfur-free) and JP-8 (1000 ppmw S) have been reformed in an ATR reactor in [126]. The effect of H_2S, which is produced from the sulfur content of the fuel at low temperatures (300 °C-400 °C) and of SO_2, formed at higher temperatures (>600 °C) is assessed separately and results to affect dramatically and irreversibly the hydrogen yield, which dropped from 75% to 40% and 55% respectively. For this reason, in a similar work [127] a ZnO desulfurizer bed has been implemented in a 5 kW reactor before the reforming stage. The degradation of noble catalyst activity has been demonstrated in [128], in which the yield of H_2 dropped from 39% to 30% and CO increased from 6% to 10% after 20 hours of operation in the oxidative steam reformer of low sulfur (15 ppm) diesel. A good example of integration of an ATR reformer, a WGSR stage and a PROX carbon monoxide remover is [72], in which high importance has been attributed to the homogeneity of the diesel/air/steam mixture. Before the clean-up stages, the syngas composition obtained by the authors was 38% H_2, 10% CO and 14% CO_2.

Steam reforming of desulfurized diesel has been carried out by [129]. Even if short-run experiments showed good results with over 70% hydrogen concentration in volume, shortly degradation of the catalyst and heavy deposits on the catalyst surface have been observed. Lower temperature steam reforming operations were also demonstrated by [130], by using supercritical water which enhance the solubility of heavy liquid fuels.

Kerosene and bio-diesel non-catalytic reforming results are not available in the open literature, to the author's knowledge. The majority of experimental investigations in this field focused on the autothermal [131; 132; 133] and steam reforming approach, which resulted in higher performance than the technique presented here. For example, in [131], dry molar fractions of 38% H_2 and of 17% of CO have been obtained by autothermal reforming of desulphurised Jet

A-1. In [134], steam reforming of kerosene led to hydrogen molar fraction over 70% and carbon monoxide molar fraction at around 10%. Similarly, autothermal reforming of biodiesel has been achieved by [74] with a dry gas composition after the ATR reactor of 41.65% hydrogen and 8.62% carbon monoxide.

The slightly poorer performance of the present non-catalytic reformer compared to the catalytic reformer is balanced, in practical applications, by the lower cost expected by the absence of a catalyst and the more robust behaviour by the capability to use a great variety of fuels in the same burner.

4.6 Chapter summary

The 70 mm ID burner has been tested for commercial fuel reforming in ceramic foams and beads (diesel) porous layers. Diesel reforming has been tested for the thermal load, equivalence ratio and porous material effect with similar general results as for n-heptane reforming. The diesel reformate proved to be sensitive to the process temperature and to the equivalence ratio, which cannot be decoupled in the thermal POX technique used in this project. High thermal loads led to high reforming temperatures, leading to conversion efficiency up to 71.1% at the maximum thermal load tested and at φ=2.0, conditions for which, the reformer also showed the lowest heat losses. At this point the hydrogen balance between reactants and products is matching better than at lower thermal loads. Further tests demonstrated that the maximum conversion efficiency is achieved at φ=2.0 and the use of alumina beads for the reforming layer (burner D) improved the hydrogen and carbon monoxide fraction for φ higher than 2.5. Finally, an endurance test has demonstrated a syngas composition fluctuating around the 8% of the mean molar fraction values.

Biodiesel has been successfully reformed to syngas in burner A and C, matching the behaviour showed by the diesel tests at different equivalence ratios. Hydrogen and carbon monoxide reach a peak and then start to decrease steeply, along with a substantial formation of light hydrocarbons, in the highest percentage among the four fuel tested in this research. The top conversion efficiency obtained was at φ=2.2 with a value of 64.9%.

Kerosene reforming has showed the highest conversion efficiency over the fuels tested. This is due mainly to the low presence of hydrocarbons in the reformate, with significant presence only of methane. The conversion efficiency was maximum at φ=2.1 with a value of 69.6%. Finally, the soot emission analysis highlighted the low particulate formation of biodiesel reforming compared to the other fuel outcome.

Of particular interest are (a) the different pathways taken by the hydrocarbon formations (ethylene compared to acetylene in n-heptane and diesel, biodiesel, kerosene reforming), (b) the presence of deposits and sooty flames at φ>2.5 in diesel reforming and (c) the ease of flash-back demonstrated by rich biodiesel flames compared to the other fuels. These issues require further studies by means of experimental and numerical investigations to achieve a fuller understanding of the chemistry involved.

An attempt to reform crude rapeseed oil has been made, but tests failed for coking of the burner, high deposits and ignition failure. A potential alternative may be the reforming of a blend of crude oil and kerosene or biodiesel, examining the stability and the functionality of the reformer. Nevertheless, the reforming of a carbon neutral feedstock such as RME Biodiesel in a robust and reliable device has been demonstrated in this Chapter, showing only minor drawbacks in comparison to the major benefits obtained.

Chapter 5

Syngas clean-up

In this chapter, some experiments concerning syngas clean-up have been undertaken. The target was to test the possibility of reducing the carbon monoxide content and transforming the remaining hydrocarbons to extra hydrogen in order to approach the requirements of a high-temperature PEM a fuel cell.

5.1 n-heptane

Single steps were undertaken to assess the improvement obtained by implementing each stage and they are described by Fig. 5.1. The columns represent the experimental mole fractions of hydrogen, carbon monoxide, carbon dioxide and the total C_1 (contributed from methane, acetylene, ethylene and ethane), while the symbols represent the corresponding calculated equilibrium results at the adiabatic flame temperature.

The first set of data depicts the results for the previously described n-heptane for burner E (a). The second set is the syngas composition with water injection ($\dot{m}_{H_2O}/\dot{m}_{C_7H_{16}}$=1) without any catalyst (b). The experimental data show a slight increase in H_2 dry molar fraction associated with an increase in CO_2 and decrease of CO molar fraction for this configuration in agreement with a "thermal" water-gas shift reaction of the reformate.

Afterwards, the SR catalyst has been inserted in the reactor and, firstly, the reaction has been driven by the water produced by the partial oxidation process only (no extra water injected - configuration (c) in Fig. 5.1). In this case, the

molar fraction of HCs is significantly reduced (from 4.5% to 1% C_1) through the reaction (5.1):

$$C_mH_n + mH_2O = mCO + (n/2 + m)H_2 \qquad (5.1)$$
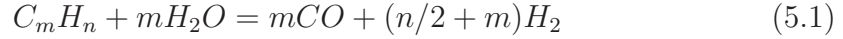
while H_2 molar fraction increased from 12.9% to 17.9%. A similar improvement has been observed by injecting extra water (d), but in this case the G-90 catalyst acted also as a WGSR: H_2 reached 20.8% and CO_2 achieved 12% whereas CO dropped to 7.3% while the HC presence is only moderately reduced.

Eventually, the high temperature water-gas shift reaction stage has also been implemented injecting a H_2O/C_7H_{16} mass flow ratio of 1 (configuration (e)) and subsequently raised to 2 (f). The final composition of the syngas is 22.3% H_2, 5.4% CO and 15.6% CO_2 with only 0.39% of CH_4, 70 ppm of C_2H_2 and 10-20 ppm of C_2H_4 and C_2H_6 left un-reformed.

The same operation has been carried out for n-heptane reforming in the same burner at the same thermal load but at φ=2.5. The results displayed in Fig. 5.2 illustrate similar trends as those at φ=2.0, with the sole difference of higher levels of the molar fractions of the syngas components over all the different steps. In more detail, the final syngas composition for configuration (f) is: 27.1% H_2, 8.7% CO, 11.8% CO_2, 0.98% CH_4, 0.02% C_2H_2, 40 ppm of C_2H_4 and 16 ppm of C_2H_6.

From the comparison with the equilibrium calculations it can be noted that the experimental and the calculated molar fractions of hydrogen differ by less than 2% for conditions (c), (d), (e) and (f). In particular, at condition (f) the experimental H_2 dry molar fraction is 22.3% and the equilibrium value is 22.6%. The biggest gap is observed at condition (b), in which the experimental H_2 dry molar fraction is 12.9% and the equilibrium value is 19.1%. This is possibly due to the lack of energy (resulting in lower temperature) to run the steam reforming process (endothermic reaction). When the catalyst is added, the steam reforming process is enhanced since the catalytic effect consists in the acceleration of the rates of the chemical reactions at low temperatures. Experimental CO and CO_2 dry molar fractions in the configurations involving a catalytic activity (configurations (c), (d), (e) and (f)) are respectively lower and higher compared to the calculated equilibrium. Moreover, the equilibrium calculation carried out at T_3 instead of the

adiabatic temperature shows an opposite behaviour, with experimental hydrogen molar fraction far from the calculated value and CO and CO_2 experimental results comparable with the calculated data. This disparity can be observed also in Fig. 5.2, for configurations (c), (d) and (e).

At φ=2.5, the experimental hydrogen molar fraction is again very close to the calculated equilibrium for configurations (c), (d), (e) and (f), in which the catalytic bed is implemented. The best match is achieved for configuration (e) with an experimental H_2 dry molar fraction of 27.7% and a calculated equilibrium value of 27.4%.

Photographs of the syngas flame ignited on top of the burner are displayed in Fig. 5.3, 5.4 and 5.5. The colour of the flame gives a qualitative indication of the species present in the syngas produced by the reformer. Passing from Fig. 5.3 to Fig. 5.4, the flame in configurations (c) and (d) is less sooty and it starts to be slightly blue because of the substantial reduction of hydrocarbons present in the off-gas. Eventually, with the implementation of the WGSR (Fig. 5.5) in configurations (e) and (f), the major component is hydrogen and hence the flame assumes a pale blue colour, difficult to visually detect. Furthermore, in configurations (e) and (f), the almost sole presence of hydrogen as species makes the flame much shorter than the flame of the other configurations. This occurs because H_2 diffuses more rapidly than most other hydrocarbon fuels do and in a laminar non-premixed flame (as the one in Fig. 5.5) molecular diffusivity plays the major role [135], together with the higher flame speed of hydrogen/air flames [136].
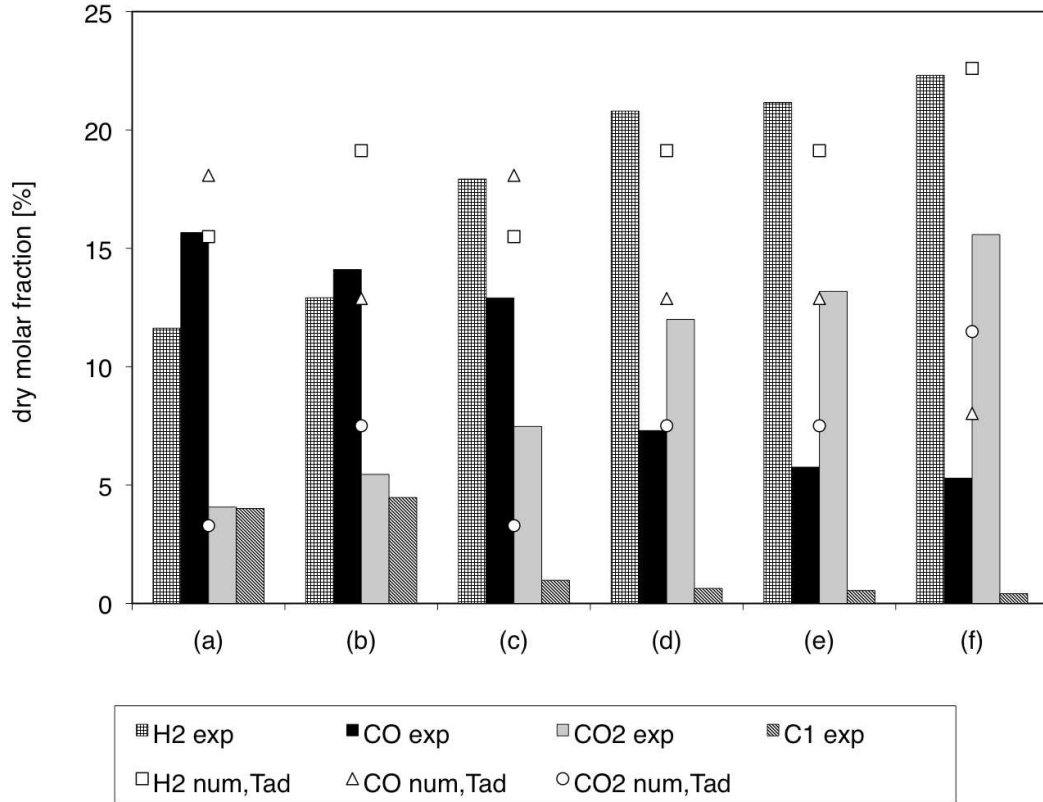
Figure 5.1: Calculated equilibrium at the adiabatic flame temperature and the experimental mole fractions (on a dry basis) for steam reforming and water-gas shift reaction experimental results of _n_-heptane reformate obtained at P=7 kW and φ=2.0 in burner E. (a) ceramic inert foam only; (b) water injection ($\dot{m}_{H_2O}/\dot{m}_{C_7H_{16}}$=1); (c) steam reforming with no extra water injected; (d) steam reforming with water injection $\dot{m}_{H_2O}/\dot{m}_{C_7H_{16}}$=1); (e) steam reforming and WGSR with water injection ($\dot{m}_{H_2O}/\dot{m}_{C_7H_{16}}$=1); (f) steam reforming and WGSR with water injection ($\dot{m}_{H_2O}/\dot{m}_{C_7H_{16}}$=2).
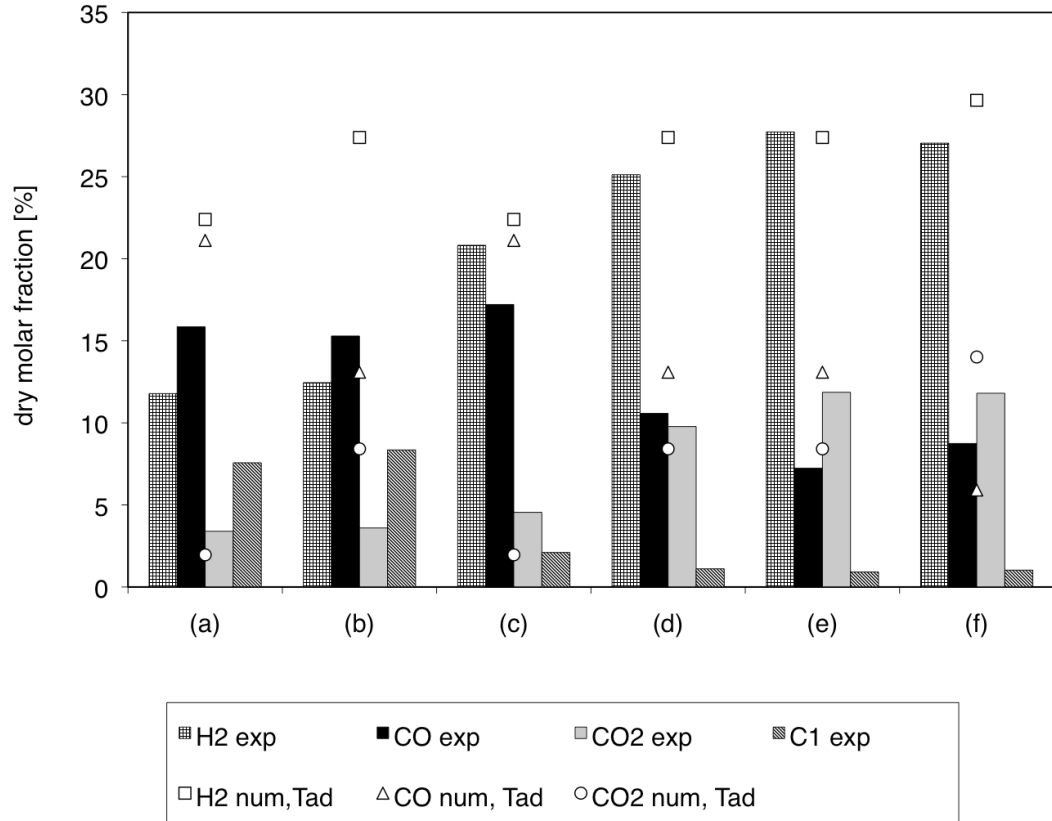
Figure 5.2: Calculated equilibrium at the adiabatic flame temperature and the experimental mole fractions (on a dry basis) for steam reforming and water-gas shift reaction experimental results of *n*-heptane reformate obtained at P=7 kW and φ=2.5 in burner E. (a) ceramic inert foam only; (b) water injection ($\dot{m}_{H_2O}/\dot{m}_{C_7H_{16}}$=1); (c) steam reforming with no extra water injected; (d) steam reforming with water injection $\dot{m}_{H_2O}/\dot{m}_{C_7H_{16}}$=1); (e) steam reforming and WGSR with water injection ($\dot{m}_{H_2O}/\dot{m}_{C_7H_{16}}$=1); (f) steam reforming and WGSR with water injection ($\dot{m}_{H_2O}/\dot{m}_{C_7H_{16}}$=2).
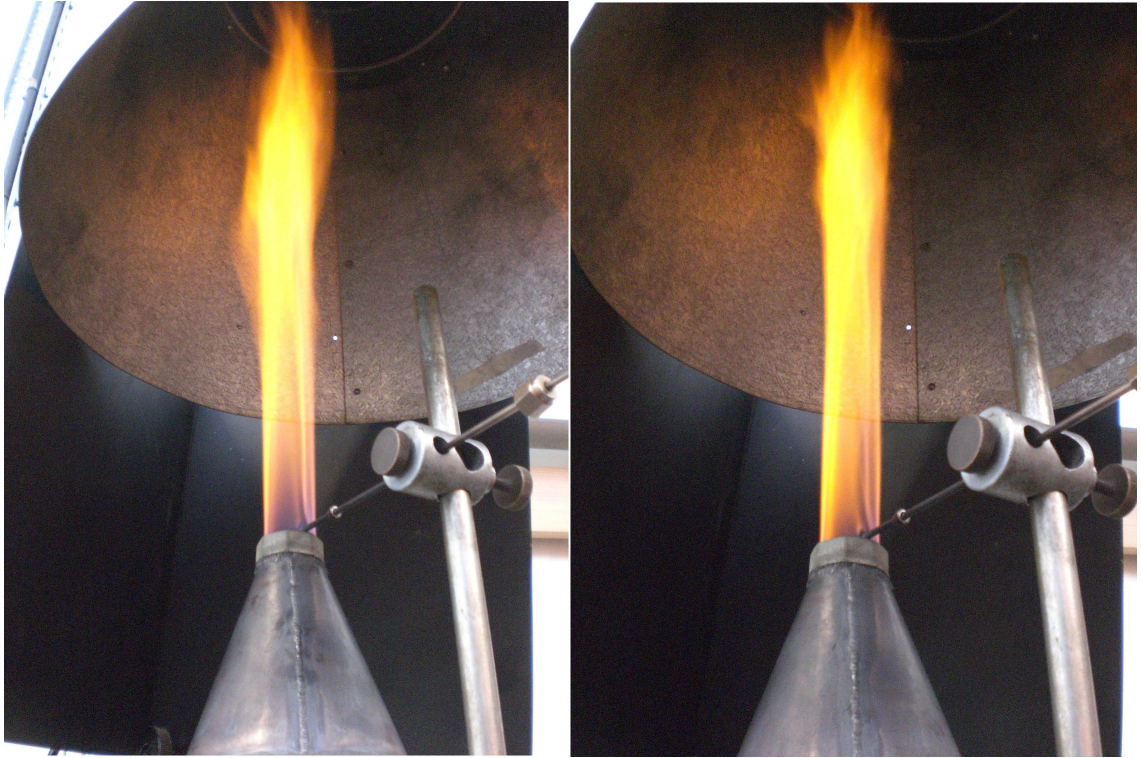
Figure 5.3: Off-gas flame at the burner's outlet for *n*-heptane at P=7 kW and φ=2.0 in burner E at configuration (a) and (b).
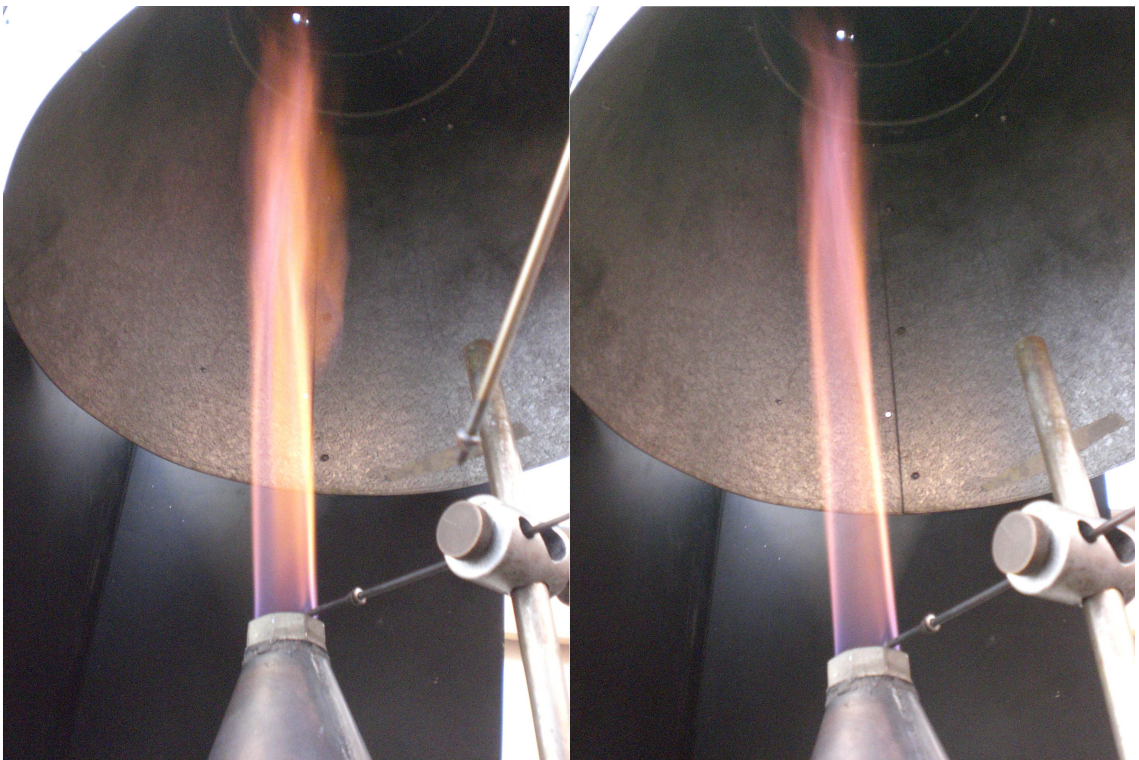
Figure 5.4: Off-gas flame at the burner's outlet for *n*-heptane at P=7 kW and φ=2.0 in burner E at configuration (c) and (d).
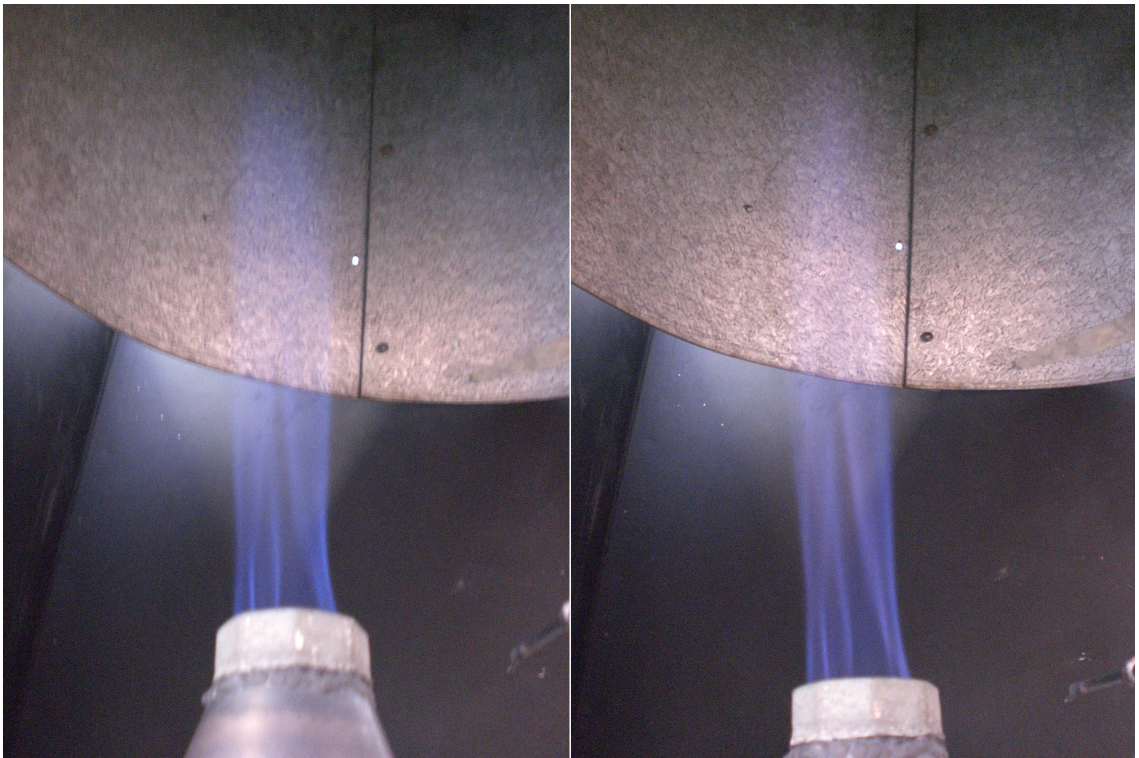
Figure 5.5: Off-gas flame at the burner's outlet for *n*-heptane at P=7 kW and φ=2.0 in burner E at configuration (e) and (f).

5.1.1 Endurance test

The functionality of the SR catalyst (Süd-chemie G 90-EW) has been also assessed over time for configuration (c). The flow conditions have been set to thermal load P=7 kW and equivalence ratio φ=2.5. Gas samples were analyzed every 15 minutes and the data are displayed in Fig. 5.6. The result is that the hydrogen molar fraction reduced from 20.8% to 19.4%, carbon monoxide passes from 17.2% to 16.9% and carbon dioxide stayes constant around 4.5% after 75 minutes of running showing a slight degradation of the catalyst with time.
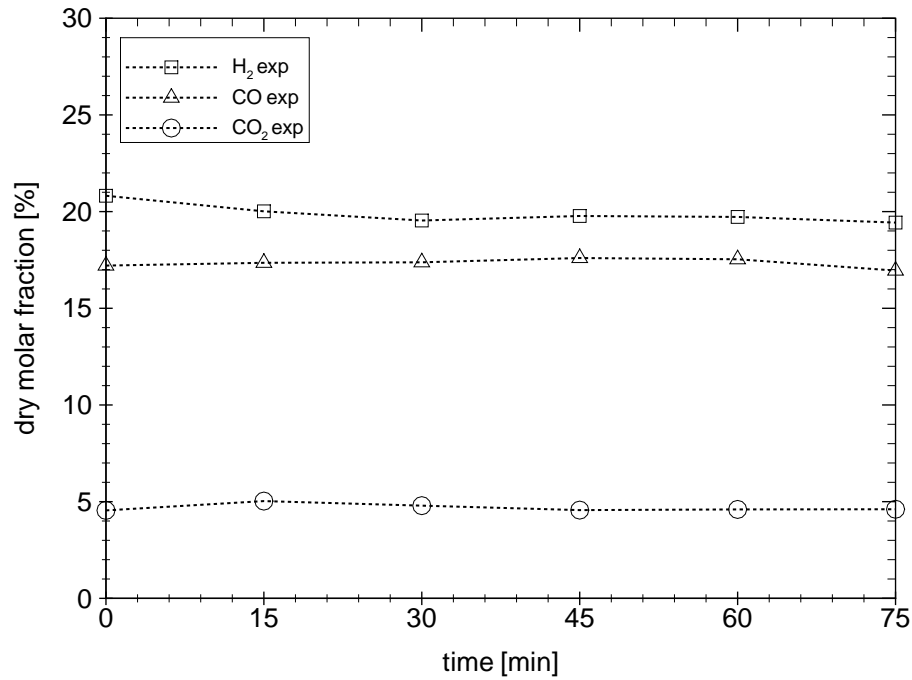
Figure 5.6: Experimental mole fractions (on a dry basis) over time for steam reforming (configuration (c) in Fig. 5.1) of *n*-heptane at P=7 kW and φ=2.5 in burner E.

5.2 Biodiesel

An attempt of syngas clean-up has been also made on the RME biodiesel reformate. The main issue concerns in the water injection. It has been noted that with the current configuration, the injection of water together with the fuel at the nozzle level, as explained in Section 2.1.4, caused the reduction of the temperature T_1 below the necessary evaporation temperature for biodiesel, resulting in high oil condensation on the burner's walls. However, transitory results have been achieved for configuration (f). For 1-2 minutes the gas samples demonstrated the functionality of the catalyst stages, before the first stage temperature dropped. Specifically, in Fig. 5.7 three different steps in the clean-up process are displayed. For the configurations (a) and (c), the flame is stable since no water was injected. The first one is the syngas composition obtained in burner E at P=7 kW and φ=2.5. Hydrogen molar fraction is around 12.6%, carbon monoxide and carbon dioxide 15.4% and 5.4% respectively and the total contribution from the hydrocarbons reached 6.03%. By adding the steam reforming catalyst only without any extra water injection, as in configuration (c), the hydrocarbon presence significantly decreased to a 0.53%. Also, hydrogen molar fraction reached almost 15% and carbon monoxide and carbon dioxide shifted to 13.3% and 6.02% respectively, demonstrating a WGSR operation of that catalytic bed. Eventually, the WGSR catalyst has been added as in configuration (f). The final composition obtained is 18.9% H_2, 4.5% CO, 16.4% CO_2, 0.34% CH_4, 0.002% C_2H_2, 40 ppm of C_2H_4 and 20 ppm of C_2H_6.
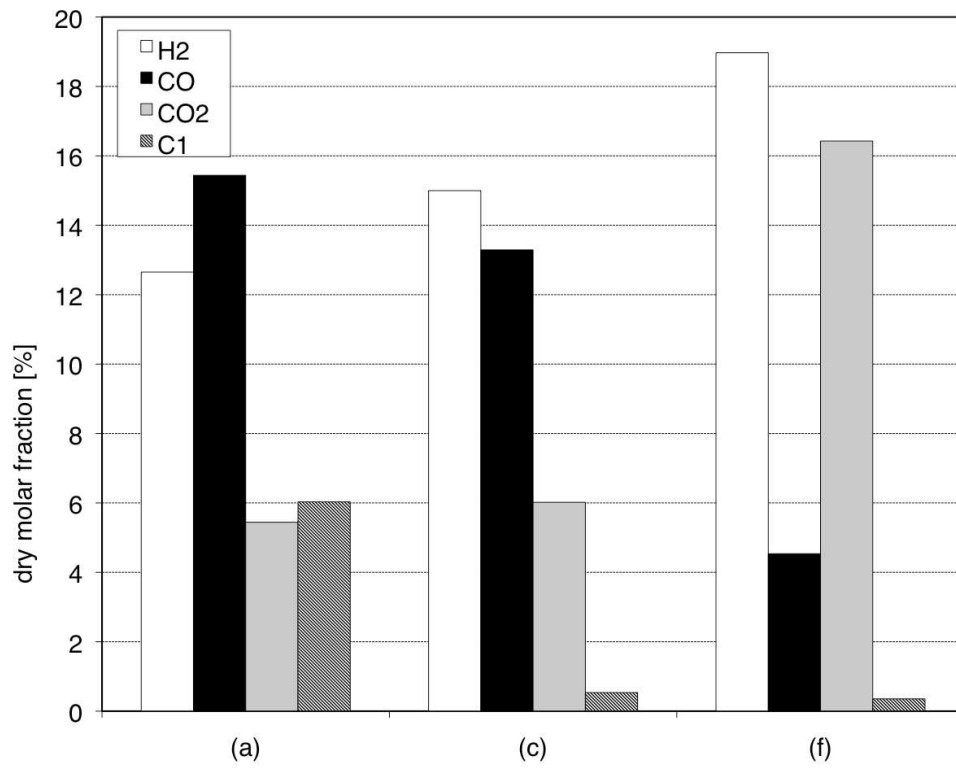
Figure 5.7: Experimental mole fractions (on a dry basis) for steam reforming and water-gas shift reaction experimental results of biodiesel reformate obtained at P=7 kW and φ=2.5 in burner E. Configurations (a), (c) and (f), as defined in Fig. 5.1.

5.3 Chapter summary

The implementation of SR and WGSR stages along with water injection has been experimentally demonstrated for n-heptane reformate clean-up. Moreover, the potential of biodiesel syngas clean-up in the reformer has been introduced, even if more work is needed to obtain stable operation and better thermal integration to avoid oil condensation. The experimental results obtained by processing n-heptane showed consistency with the calculated equilibrium data, especially for hydrogen molar fraction. Eventually, a slight degradation of the G-90 EW steam reforming catalyst activity has been observed over 75 minutes of operation.

Chapter 6

Conclusions

6.1 Summary

The objectives of this thesis were to design a reactor based on the two-layer porous inert medium partial oxidation, to study the behaviour of the reformer varying the characteristic parameters of the system (equivalence ratio, thermal load, materials) and to demonstrate the flexibility of the reactor with different heavy liquid commercial fuels. In order to achieve these targets, a compact reactor has been designed and investigated by means of temperature detectors and of a gas analyser. A vapouriser based on a commercial air-assisted nozzle fed with hot air has been designed and embedded in the reactor and an automotive spark-plug system has been implemented for the ignition of the air/fuel mixture. Temperatures were measured at three different stages with K-type and R-type thermocouple to monitor the temperature of the pre-vapouriser, of the porous medium interface and of the gas samples and a Gas Chromatograph calibrated for H_2, O_2, N_2, CO, CO_2, CH_4, C_2H_2, C_2H_4 and C_2H_6 measured the species present in the reformate. Different fuels have been successfully reformed.

First of all, n-heptane has been processed in several burner setups with different material, diameter and length. The most successful configuration was the alumina bead packed bed burner, which displayed the highest conversion efficiencies over the equivalence ratio values investigated. Specifically, the conversion efficiency peaked at 75% at φ=2.5 for P=7 kW with H_2, CO and CO_2 experimental dry molar fractions of 19.3%, 19.9% and 2.3%. Preliminary tests have

been carried out for this fuel to assess the homogeneity of the air/fuel mixture and demonstrated a good uniformity of fuel vapour, especially for the 70 mm ID burner. Moreover, the reformate over the 100 mm ID burner surface was quite uniform in composition. The operating range of burner C was explored and the equivalence ratio of 2 displayed the broadest range of flame speed that could be stabilised in the two-layer porous medium reactor. At this equivalence ratio, the reformate composition approached very closely the equilibrium data, calculated by means of the NASA CEA database. Composition closer to the equilibrium were achieved with high thermal loads, which also demonstrated low heat losses - approximately 10% - calculated from the energy balance between the products and the reactants. A particulate emission investigation has been performed, pointing to φ=2.0 as the soot limit; above this equivalence ratio soot was generated.

The reforming investigation has been extended to commercial heavy liquid fuels and diesel, kerosene and biodiesel have been successfully converted to hydrogen-enriched gas. These fuels demonstrated a similar beahaviour to n-heptane, but diesel and biodiesel exhibited lower conversion efficiency and hydrogen content due to their low $H_2 : C$ ratio and the complexity of the fuel molecule, which led to slow kinetics, sensitive to the process temperature and leading to significant light hydrocarbon formation at rich equivalence ratios. Diesel conversion efficiency peaked at φ=2.0 for P=7 kW in burner A with a value of η_{LHV}=62.7% and H_2, CO and CO_2 experimental dry molar fractions reach values of 12%, 16.6% and 4.8% respectively. Biodiesel conversion efficiency resulted to a maximum at φ=2.2 for P=7 kW in burner A with η_{LHV}=64.9% with H_2, CO and CO_2 experimental dry molar fractions reaching values of 14.0%, 19.1% and 4.4% respectively. Kerosene was the only fuel which could be compared to equilibrium calculations and demonstrated close results to the calculated fractions up to an equivalence ratio of 2. Its efficiency peaked at φ=2.1 for P=7 kW in burner A with the value of η_{LHV}=69.6% and H_2, CO and CO_2 experimental dry molar fractions reach values of 13.8%, 18.9% and 3.2% respectively. The soot investigation showed that biodiesel has the lowest particulate emissions out of the three fuels, most likely due to the oxygen content in the molecule.

Finally, steam reforming and water-gas shift reactions have been applied to the reformate obtained from n-heptane and biodiesel in order to remove light hydrocarbons and carbon monoxide from the syngas obtained by the partial oxidation process. Commercial catalysts have been inserted in the reactor and different configurations involving water injection have been tested. The experimental results gave confidence in the feasibility of the process by approaching equilibrium calculations and for n-heptane a H_2 mole fraction of 27.1% has been achieved with 8.7% CO and around 1% C_1 at φ=2.5. Better thermal integration in order to avoid sharp temperature drops due to the water injections must be adopted in potential further research, but the "pale blue" off-gas flame and the gas analysis demonstrated the functionality of the concept with hydrogen as the main component of the syngas obtained.

6.2 Suggestion for further research

Further research may focus on experimental and modelling work. On the experimental side, research on better use of the heat produced by the partial oxidation process would help to improve the global efficiency of the system. Moreover, more resistant material to thermal cycles should be found and tested and maybe a combination of foams and beads may lead to use the benefits given by the two solutions (quick response for the foam and high efficiency for the bead layer). A very important step forward would be a more detailed analysis of the syngas composition, which would allow to detect all the species which in this research were missing from the carbon balance, especially high hydrocarbons. Eventually, a clean-up stage based on the results here obtained may be implemented and a integration with a fuel cell system should be attempted.

On the modelling side, a study of the structure of the flame for n-heptane and possibly for a real fuel (kerosene) would be beneficial in the understanding of the reforming mechanisms and in the main step controlling the reactions. The experimental data described in this thesis may help validating a potential computational model.

References

[1] U.S. DOE. *Annual energy review 2009*. Energy Information Administration, 2010. xi, 2

[2] C. Song. Fuel processing for low-temperature and high-temperature fuel cells: Challenges, and opportunities for sustainable development in the 21st century. *Catalysis Today*, 77:17–49, 2002. xi, 5, 6, 11, 14, 15

[3] A.J. Barra, G. Diepvens, J.L. Ellzey, and M.R. Henneke. Numerical study of the effects of material properties on flame stabilization in a porous burner. *Combustion and Flame*, 134:369–379, 2003. xi, 16

[4] M.J. Dixon, I. Schoegl, C.B. Hull, and J.L. Ellzey. Experimental and numerical conversion of liquid heptane to syngas through combustion in porous media. *Combustion and Flame*, 154:217–231, 2008. xi, 17, 19, 20, 89

[5] G. Vourliotakis, G. Skevis, M.A. Founti, Z. Al-Hamamre, and D. Trimis. Detailed kinetic modelling of the T-POX reforming process using a reactor network approach. *International Journal of Hydrogen Energy*, 33:2816–2825, 2008. xi, 20, 21

[6] Paul Smith Customer relations. Private communication. xii, 46

[7] Thomas Starke Sales manager. Private communication. xii, 47

[8] Conoco Phillips. Product information. `http://www.conocophillips.co.uk/EN/fuels/productinfo/pages/index.aspx`. xii, 48

[9] Rotexo. COSILAB. `http://www.rotexo.com/cms/index.php`. xiii, 60

[10] M. Chaos, A. Kazakov, Z.W. Zhao, and F.L. Dryer. A high-temperature chemical kinetic model for primary reference fuels. *International Journal of Chemical Kinetics*, 39:339–414, 2007. xiii, 19, 39, 60

[11] EIA. Greenhouse gases, climate change, and energy. `http://www.eia.doe.gov/oiaf/1605/ggccebro/chapter1.html`. 1

[12] P. Moriarty and D. Honnery. Hydrogen's role in an uncertain energy future. *International Journal of Hydrogen Energy*, 34:31–39, 2009. 1

[13] N.Z. Muradova and T.N. Veziroglu. "Green" path from fossil-based to hydrogen economy: An overview of carbon-neutral technologies. *International Journal of Hydrogen Energy*, 33:6804–6839, 2008. 2

[14] J. Wee. Contribution of fuel cell systems to CO_2 emission reduction in their application fields. *Renewable and Sustainable Energy Reviews*, 14:735–744, 2010. 2

[15] A. Brooks. Why hydrogen? *CARB Hydrogen Highway Network Workshop*, 2005. 3

[16] M. Balat. Potential importance of hydrogen as a future solution to environmental and transportation problems. *International Journal of Hydrogen Energy*, 33:4013–4029, 2008. 3

[17] IEA. *Hydrogen Production and Distribution*. IEA Energy Technology Essentials, 2007. 3, 7

[18] T.E. Lipman. What will power the hydrogen economy? Analysis and report prepared for the natural resources defense council., 2004. 3

[19] J. Brouwer. On the role of fuel cells and hydrogen in a more sustainable and renewable energy future. *Current Applied Physics*, 10:9–17, 2010. 4

[20] L. Barreto, A. Makihira, and K. Riahi. The hydrogen economy in the 21st century: a sustainable development scenario. *International Journal of Hydrogen Energy*, 28:267–284, 2003. 4

[21] P. Agnolucci. Economics and market prospects of portable fuel cells. *International Journal of Hydrogen Energy*, 32:4319–4328, 2007. 4

[22] S. Carnot. *Reflexions sur la Puissance Motrice du Feu*. Paris, 1824. 4

[23] IEA. Fossil fuel-fired power generation., 2007. 4

[24] M. Jones. Hybrid vehicles the best of both worlds. *Chemistry and Industry*, 15:589–592, 1995. 4

[25] F. Barbir and T. Gomez. Efficiency and economics of proton exchange membrane (PEM) fuel cells. *International Journal of Hydrogen Energy*, 22:1027–1037, 1997. 4

[26] R. Farrauto, S. Hwang, L. Shore, W. Ruettinger, J. Lampert, T. Giroux, Y. Liu, and O. Ilinich. New material needs for hydrocarbon fuel processing: Generating hydrogen for the PEM fuel cell. *Annual Review of Materials Research*, 33:1–27, 2003. 5, 7

[27] A. Naidja, C.R. Krishna, T. Butcher, and D. Mahajan. Cool flame partial oxidation and its role in combustion and reforming of fuels for fuel cell systems. *Progress in Energy and Combustion Science*, 29:155–191, 2003. 5, 11

[28] A.L. Dicks. Hydrogen generation from natural gas for the fuel cell systems of tomorrow. *Journal of Power Sources*, 61:113–124, 1996. 5

[29] L.J. Pettersson and R. Westerholm. State of the art of multi-fuel reformers for fuel cell vehicles: problem identification and research needs. *International Journal of Hydrogen Energy*, 26:243–264, 2001. 6

[30] C.N. Satterfield. *Heterogeneous Catalysis in Industrial Practice*. Krieger Publishing Company, 1996. 6

138

[31] J.C. Amphlett, K.A.M. Creber, J.M. Davis, R.F. Mann, B.A. Peppley, and D.M. Stokes. Hydrogen production by steam reforming of methanol for polymer electrolyte fuel cells. *International Journal of Hydrogen Energy*, 19:131–137, 1994. 6, 8

[32] S. Ahmed and M. Krumpelt. Hydrogen from hydrocarbon fuels for fuel cells. *International Journal of Hydrogen Energy*, 26:291–301, 2001. 7, 13, 14

[33] Q. Ming, T. Healey, L. Allen, and P. Irving. Steam reforming of hydrocarbon fuels. *Catalysis Today*, 77:51–64, 2002. 7, 14

[34] D.L. Trimm and Z.I. Onsan. Onboard fuel conversion for hydrogen-fuel-cell-driven vehicles. *Catalysis Reviews*, 43:31–84, 2001. 7, 10

[35] D. Dalle Nogare, P. Baggio, C. Tomasi, L. Mutri, and P. Canu. A thermodynamic analysis of natural gas reforming processes for fuel cell application. *Chemical Engineering Science*, 62:5418–5424, 2007. 7

[36] A. Ristori, P. Dagaut, and M. Cathonnet. Production of hydrogen by steam reforming of methanol on CeO_2 promoted Cu/Al_2O_3 catalysts. *Journal of Molecular Catalysis A: Chemical*, 194:99–105, 2003. 8

[37] J. Sun, X. Qiu, F. Wu, W. Zhu, W. Wang, and S. Hao. Hydrogen from steam reforming of ethanol in low and middle temperature range for fuel cell application. *International Journal of Hydrogen Energy*, 29:1075–1081, 2004. 8

[38] P. Yaseneva, S. Pavlova, V. Sadykov, E. Moroz, E. Burgina, L. Dovlitova, V. Rogov, S. Badmaev, S. Belochapkin, and J. Ross. Hydrogen production by steam reforming of methanol over $CuCeZrYO_x$-based catalysts. *Catalysis Today*, 138:175–182, 2008. 8

[39] S. Patel and K.K. Pant. Experimental study and mechanistic kinetic modeling for selective production of hydrogen via catalytic steam reforming of methanol. *Chemical Engineering Science*, 62:5425–5435, 2007. 8

[40] A. Iulianelli, T. Longo, and A. Basile. Methanol steam reforming reaction in a Pd-Ag membrane reactor for CO-free hydrogen production. *International Journal of Hydrogen Energy*, 33:5583–5588, 2008. 8

[41] T. Huang and H.M. Chen. Hydrogen production via steam reforming of methanol over $Cu/(Ce,Gd)O_{2-x}$ catalysts. *International Journal of Hydrogen Energy*, 35:6218–6226, 2010. 8

[42] T.H. Yen, W.T. Hong, W.P. Huang, Y.C. Tsai, H.Y. Wang, C.N. Huang, and C.H. Lee. Experimental investigation of 1 kW solid oxide fuel cell system with a natural gas reformer and an exhaust gas burner. *Journal of Power Sources*, 195:1454–1462, 2010. 8

[43] J. Mathiak, A. Heinzel, J. Roes, T. Kalk, H. Kraus, and H. Brandt. Coupling of a 2.5 kW steam reformer with a 1 kW_{el} PEM fuel cell. *Journal of Power Sources*, 131:112–119, 2004. 9

[44] D.G. Lffler, K. Taylor, and D. Mason. A light hydrocarbon fuel processor producing high-purity hydrogen. *Journal of Power Sources*, 117:84–91, 2003. 9

[45] P.C. Hulteberg, H. Burford, K. Duraiswamy, B. Porter, and R. Woods. A cost effective steam reformer for a distributed hydrogen infrastructure. *International Journal of Hydrogen Energy*, 33:1266–1274, 2008. 9

[46] J.M. Sohn, Y.C. Byun, J.Y. Cho J. Choe, and K.H. Song. Development of the integrated methanol fuel processor using micro-channel patterned devices and its performance for steam reforming of methanol. *International Journal of Hydrogen Energy*, 32:5103–5108, 2007. 9

[47] J.G.M. Furtado, G.C. Gatti, E.T. Serra, and S.C.A. de Almeida. Performance analysis of a 5 kW PEMFC with a natural gas reformer. *International Journal of Hydrogen Energy*, In Press, 2010. 9

[48] M. Prettre, C. Eichner, and M. Perrin. The catalytic oxidation of methane to carbon monoxide and hydrogen. *Transactions of the Faraday Society*, 43:335–340, 1946. 10

[49] D.A. Hickman and L.D. Schmidt. Synthesis gas formation by direct oxidation of methane over Pt monoliths. *Journal of Catalysis*, 138:267–282, 1992. 10

[50] P.D.F. Vernon, M.L.H. Green, A.K. Cheetham, and A.T. Ashcroft. Partial oxidation of methane to synthesis gas, and carbon dioxide as an oxidising agent for methane conversion. *Catalysis Today*, 13:417–426, 1992. 10

[51] S.S. Bharadwaj and L.D. Schmidt. Catalytic partial oxidation of natural gas to syngas. *Fuel Process Technology*, 42:109–127, 1995. 10, 14

[52] S.A. Seyed-Reihani and G.S. Jackson. Catalytic partial oxidation of n-butane over Rh catalysts for solid oxide fuel cell applications. *Catalysis Today*, In Press, 2009. 11

[53] I. Aartun, B. Silberova, H. Venvik, P. Pfeifer, O. Grke, K. Schubert, and A. Holmen. Hydrogen production from propane in Rh-impregnated metallic microchannel reactors and alumina foams. *Catalysis Today*, 105:469–478, 2005. 11

[54] P. Corbo and F. Migliardini. Hydrogen production by catalytic partial oxidation of methane and propane on Ni and Pt catalysts. *International Journal of Hydrogen Energy*, 32:55–56, 2007. 11

[55] S.N.K.K. Aki and M.A. Abraham. Catalytic partial oxidation of methane in supercritical water. *The Journal of Supercritical Fluids*, 7:259–263, 1994. 11

[56] M. Dajiang, C. Yaoqiang, Z. Junbo, W. Zhenlinga, M. Di, and G. Maochu. Catalytic partial oxidation of methane over Ni/CeO_2 -ZrO_2 -Al_2O_3. *Journal of Rare Earths*, 25:311–315, 2007. 11

[57] R. Subramanian, G.J. Panuccio, J.J. Krummenacher, I.C. Lee, and L.D. Schmidt. Catalytic partial oxidation of higher hydrocarbons: reactivities and selectivities of mixtures. *Chemical Engineering Science*, 59:5501–5507, 2004. 11

[58] D.J. Haynes, A. Campos, D.A. Berry, D. Shekhawat, A. Roy, and J.J. Spivey. Catalytic partial oxidation of a diesel surrogate fuel using an Ru-substituted pyrochlore. *Catalysis Today*, In Press, 2009. 11

[59] P.K. Cheekatamarla and C.M. Finnerty. Synthesis gas production via catalytic partial oxidation reforming of liquid fuels. *International Journal of Hydrogen Energy*, 33:5012–5019, 2008. 11, 117

[60] H. Pedersen-Mjaanes, L. Chan, and E. Mastorakos. Hydrogen production from rich combustion in porous media. *International Journal of Hydrogen Energy*, 30:579–592, 2005. 11, 18

[61] A. Pastore and E. Mastorakos. Hydrogen production from rich combustion in porous media. *Experimental Thermal and Fluid Science*, 34:359–365, 2010. 11, 18, 89

[62] M.K. Drayton, A.V. Saveliev, L.A. Kennedy, A.A. Fridman, and Y. Li. Syngas production using superadiabatic combustion of ultra-rich methane-air mixtures. *Proceeding of the Combustion Institute*, 27:1361–1367, 1998. 11, 17, 59, 89

[63] I. Schoegl, S.R. Newcomb, and J.L. Ellzey. Ultra-rich combustion in parallel channels to produce hydrogen-rich syngas from propane. *International Journal of Hydrogen Energy*, 34:5152–63, 2009. 11, 59

[64] Z. Al-Hamamre, S. Voß, and D. Trimis. Hydrogen production by thermal partial oxidation of hydrocarbon fuels in porous media based reformer. *International Journal of Hydrogen Energy*, 34:827–832, 2009. 11, 20

[65] F.J. Weinberg, T.G. Bartleet, F.B. Carleton, P. Rimbotti, J.H. Brophy, and R.P. Manning. Partial oxidation of fuel-rich mixtures in a spouted bed combustor. *Combustion and Flame*, 72:235–239, 1988. 11

[66] D. Trimis, K. Wawrzinek, O. Harzfeld, K. Lucka, A. Rutsche, F. Haase, K. Krüger, and C. Küchen. High modulation burner for liquid fuels based

on porous media combustion and cool flame vaporization. *6th International Conference on Technologies and Combustion for a Clean Environment (Clean Air VI)*, 2001. 11

[67] S.C. Reyes, J.H. Sinfelt, and J.S. Feeley. Evolution of processes for synthesis gas production: Recent developments in an old technology. *Industrial & Engineering Chemistry Research*, 42:1588–1597, 2003. 12, 14

[68] M. Krumpelt, T.R. Krause, J.D. Carter, J.P. Kopasz, and S. Ahmed. Fuel processing for fuel cell systems in transportation and portable power applications. *Catalysis Today*, 77:3–16, 2002. 12

[69] A. Docter and A. Lamm. Gasoline fuel cell systems. *Journal of Power Sources*, 84:194–200, 1999. 12, 13

[70] B.J. Bowers, J.L. Zhao, M. Ruffo, R. Khan, D. Dattatraya, N. Dushman, J.C. Beziat, and F. Boudjemaa. Onboard fuel processor for PEM fuel cell vehicles. *International Journal of Hydrogen Energy*, 32:1437–1442, 2007. 13

[71] C. Severin, S. Pischinger, and J. Ogrzewalla. Compact gasoline fuel processor for passenger vehicle APU. *Journal of Power Sources*, 145:675–682, 2005. 13

[72] B. Lindström, J.A.J. Karlsson, P. Ekdunge, L. De Verdier, B. Häggendal, J. Dawody, M. Nilsson, and L.J. Pettersson. Diesel fuel reformer for automotive fuel cell applications. *International Journal of Hydrogen Energy*, 34:3367–3381, 2009. 13, 118

[73] S. Yoon and J. Bae. A diesel fuel processor for stable operation of solid oxide fuel cells system: I. Introduction to post-reforming for the diesel fuel processor. *Catalysis Today*, In Press, 2010. 13

[74] G.J. Kraaij, S. Specchia, G. Bollito, L. Mutri, and D. Wails. Biodiesel fuel processor for APU applications. *International Journal of Hydrogen Energy*, 34:4495–4499, 2009. 13, 119

[75] Y.S. Seo, A. Shirley, and S.T. Kolaczkowski. Evaluation of thermodynamically favourable operating conditions for production of hydrogen in three different reforming technologies. *Journal of Power Sources*, 108:213–225, 2002. 14

[76] J.M. Ogden. Review of small stationary reformers for hydrogen production, 2001. IEA report-UC Davies. 14

[77] E. Almqvistt. *History of Industrial Gases*. Plenum Publishers, 2003. 14

[78] J.D. Holladay, J. Hu, D.L. King, and Y. Wang. An overview of hydrogen production technologies. *Catalysis Today*, 139:244–260, 2009. 15

[79] C.D. Dudfield, R.Chen, and P.L. Adcock. A compact CO selective oxidation reactor for solid polymer fuel cell powered vehicle application. *Journal of Power Sources*, 86:214–222, 2000. 15

[80] A. Rehmat and S.S. Randhava. Selective methanation of carbon monoxide. *Industrial & Engineering chemistry product research and development*, 9:512–515, 1970. 15

[81] S. Gottesfeld and J. Pafford. A new approach to the problem of carbon monoxide poisoning in fuel cells operating at low temperatures. *Journal of the Electrochemical Society*, 135:2651–2652, 1988. 15

[82] Johnson Matthey. Palladium membrane hydrogen purifiers: outside-in or inside-out flow - which design is best for compound semiconductors? Tech bulletin. 15

[83] D.R. Hardesty and F.J. Weinberg. Burners producing large excess enthalpies. *Combustion Science and Technology*, 8:201–214, 1974. 16

[84] Y. Kotani and T. Takeno. An experimental study on stability and combustion characteristics of an excess enthalpy flame. *Proceeding of the Combustion Institute*, 19:1503–1509, 1982. 16

[85] F.J. Weinberg. Combustion temperatures: the future?, 1971. Nature. 16

[86] W.A. Bone. Surface combustion. *J. Franklin Inst. State Penn.*, 173:101–131, 1912. 16

[87] Y.M. Laevskii and V.S. Babkin. Stabilized gas combustion wave in an inert porous medium. *Combustion, Explosion, and Shock Waves*, 44:502–508, 2008. 16

[88] V.S. Babkin, V.I. Drobyshevich, Y.M. Laevskii, and S.I. Potytnyakov. Filtration combustion of gases. *Fizika Goreniya i Vzryva*, 19:17–26, 1983. 16

[89] K. Hanamura, R. Echigo, and S.A. Zhdanok. Superadiabatic combustion in a porous medium. *International Journal of Heat and Mass Transfer.*, 36:3201–3209, 1993. 16

[90] D.J. Diamantis, E. Mastorakos, and D.A. Goussis. Simulations of premixed combustion in porous media. *Combustion Theory and Modeling*, 6:383–411, 2002. 16, 59

[91] J.P. Bingue, A.V. Saveliev, A.A. Fridman, and L.A. Kennedy. Hydrogen production in ultra-rich filtration combustion of methane and hydrogen sulfide. *Journal of Hydrogen Research*, 27:643–649, 2002. 17

[92] V.S. Babkin, A.A. Korzhavin, and V.A. Bunev. Propagation of premixed gaseous explosion flames in porous media. *Combustion and Flame*, 87:182–190, 1991. 17, 18, 59

[93] Z. Al-Hamamre and A. Al-Zoubi. The use of inert porous media based reactors for hydrogen production. *International Journal of Hydrogen Energy*, 35:1971–1986, 2010. 17

[94] D. Trimis and F. Durst. Combustion in a porous medium-advances and applications. *Combustion Science and Technology*, 121:153–168, 1996. 18

[95] W.M. Mathis and J.L. Ellzey. Flame stabilization, operating range, and emissions for a methane/air porous burner. *Combustion Science and Technology*, 175:825–839, 2003. 18

[96] S. Wood and A.T. Harris. Porous burners for lean-burn applications. *Progress in Energy and Combustion Science*, 34:667–684, 2008. 18

[97] V. Khanna, R. Goel, and J.L. Ellzey. Measurement of emissions and radiation for methane combustion within a porous medium burner. *Combustion Science and Technology*, 133:133–142, 1994. 18

[98] R. Mital, J.P. Gore, and Viskanta. A study of the structure of submerged reaction zone in porous ceramic radiant burners. *Combustion and Flame*, 111:175–184, 1997. 18

[99] F. Von Issendorff, V. Stamatov, A. Mach, and D. Trimis. Application of porous burners in industrial furnaces for glass production. *Proceedings of the Eighth International Conference on Technologies Combustion for a Clean Environment (Clean Air VIII)*, 2005. 19

[100] S. Mößbauer, O. Pickenäcker, and D. Trimis. Application of the porous burner technology in energy- and heat-engineering. *Proceedings of the Fifth International Conference on Technologies Combustion for a Clean Environment (Clean Air V)*, 1999. 19

[101] A. Ristori, P. Dagaut, and M. Cathonnet. The oxidation of n-hexadecane: experimental and detailed kinetic modeling. *Combustion and Flame*, 125:1128–1137, 2001. 20

[102] Sigma-Aldrich Co Ltd. Alumina Oxide for drying properties. `http://www.sigmaaldrich.com`. 28

[103] Lanik. Vukopor HT and Vukopor S properties. `http://www.lanik.cz/`. 29, 30

[104] H. Freund, T. Zeiser, F. Huber, E. Klemm, G. Brenner, F. Durst, and G. Emig. Numerical simulations of single phase reacting flows in randomly packed fixed-bed reactors and experimental validation. *Chemical Engineering Science*, 58:903–910, 2003. 30

[105] Almatis. T-162 Tabular Alumina balls Data sheet. `http://www.almatis.com`. 30

[106] A. Petzold and J. Ulbricht. *Feuerbeton und betonartige feuerfeste Massen und Materialien.* Verlag Deutscher Verlag für Grundstoffindustrie, 1994. 30

[107] TC Ltd. Guide to Thermocouple and Resistance Thermometry. `http://www.tc.co.uk/`. 36, 37

[108] D.J. Cookson, P. Iliopoulos, and B.E. Smith. Composition-property relations for jet and diesel fuels of variable boiling range. *Fuel*, 74:70–78, 1995. 39, 40

[109] A. Sarioglan, H. Olgun, M. Baranak, A. Ersoz, H. Atakul, and S. Ozdogan. Diesel evaporation as the first step of hydrogen production. *International Journal of Hydrogen Energy*, 32:2895–2901, 2007. 39

[110] S. Jugjai and N. Polmart. Enhancement of evaporation and combustion of liquid fuels through porous media. *Experimental Thermal and Fluid Science*, 27:901–909, 2003. 40

[111] T. Hoshino, Y. Iwata, and H. Koseki. Oxidation stability and risk evaluation of biodiesel. *Thermal Science*, 11:87–100, 2007. 40

[112] K. Arisoy. Oxidative and thermal instability of biodiesel. *Energy Sources A*, 30:1516–1522, 2008. 40

[113] T.A. Foglia, K.C. Jones, A. Nunez, J.G. Phillips, and M. Mittelbach. Comparison of chromatographic methods for the determination of bound glycerol in biodiesel. *Chromatographia*, 60:305–311, 2004. 40

[114] A.H. Lefebvre. *Gas Turbine Combustion.* McGraw-Hill, 1999. 50

[115] NASA. Computer Program CEA (Chemical Equilibrium with Applications). `http://www.grc.nasa.gov/WWW/CEAWeb/ceaHome.htm`. 51

[116] Turns. HPFLAME - module for adiabatic flame temperature calculation. 51, 112

[117] P.F. Hsu, W.D. Evans, and J.R. Howell. Experimental and numerical study of premixed combustion within nonhomogeneous porous ceramics. *Combustion Science and Technology*, 90:149–172, 1993. 59

[118] C.Y. Nah and S. Palanki. Analysis of heptane autothermal reformer to generate hydrogen for fuel cell applications. *International Journal of Hydrogen Energy*, 34:8566–8573, 2009. 67

[119] B.S. Haynes and H.G. Wagner. Soot formation. *Progress in Energy and Combustion Science*, 7:229–273, 1981. 88

[120] A.B. Mhadeshwar and D.G. Vlachos. Hierarchical multiscale mechanism development for methane partial oxidation and reforming and for thermal decomposition of oxygenates on Rh. *Journal of Physical Chemistry B*, 109:16819–16835, 2005. 89

[121] K.V. Dobrego, N.N. Gnesdilov, S.H. Lee, and H.K. Choi. Overall chemical kinetics model for partial oxidation of methane in inert porous media. *Chemical Engineering Journal*, 144:79–87, 2008. 89

[122] V.A. Levin, G.D. Smekhov, and A.N. Khmelevskii. Modeling of equilibrium combustion of kerosene by a mixture of gaseous hydrocarbons. *Combustion, Explosion, and Shock Waves*, 43:373–377, 2007. 112

[123] Z. Al-Hamamre, S. Deizinger, A. Mach, F. Von Issendorff, and D. Trimis. Thermal partial oxidation of diesel in porous reactors for synthesis gas production. *Clean Air*, 7:391–407, 2006. 117

[124] A. Lindermeir, S. Kah, S. Kavurucu, and M. Muhlner. On-board diesel fuel processing for an SOFC-APU-technical challenges for catalysis and reactor design. *Applied Catalysis B: Environmental*, 70:488–497, 2007. 117

[125] I. Kang and J. Bae. Autothermal reforming study of diesel for fuel cell application. *Journal of Power Sources*, 159:1283–1290, 2006. 118

[126] P.K. Cheekatamarla and A.M. Lane. Catalytic autothermal reforming of diesel fuel for hydrogen generation in fuel cells I. Activity tests and sulfur poisoning. *Journal of Power Sources*, 152:256–263, 2005. 118

[127] S. Roychoudhury, M. Lyubovsky, D. Walsh, D. Chub, and E. Kallio. Design and development of a diesel and JP-8 logistic fuel processor. *Journal of Power Sources*, 160:510–513, 2006. 118

[128] F. Rosa, E. Lopez, Y. Briceno, D. Sopena, R.M. Navarro, M.C. Alvarez-Galvan, J.L.G. Fierro, and C. Bordons. Design of a diesel reformer coupled to a PEMFC. *Catalysis Today*, 116:324–333, 2006. 118

[129] C. Mengel, M. Konrad, R. Wruck, K. Lucka, and H. Kohne. Diesel Steam Reforming for PEM Fuel Cells. *Journal of Fuel Cell Science and Technology*, 5, 2008. 118

[130] K. Pinkwart, T. Bayha, W. Lutter, and M. Krausa. Gasification of diesel oil in supercritical water for fuel cells. *Journal of Power Sources*, 136:211–214, 2004. 118

[131] B. Lenz and T. Aicher. Catalytic autothermal reforming of jet fuel. *Journal of Power Sources*, 149:44–52, 2005. 118

[132] J. Pasel, J. Meissner, Z. Pors, R.C. Samsun, A. Tschauder, and R. Peters. Autothermal reforming of commercial Jet A-1 on a 5 kWe scale. *International Journal of Hydrogen Energy*, 32:4847–4858, 2007. 118

[133] B.J. Dreyer, I.C. Lee, J.J. Krummenacher, and L.D. Schmidt. Autothermal steam reforming of higher hydrocarbons: n-decane, n-hexadecane, and JP-8. *Applied Catalysis A: General*, 307:184–194, 2006. 118

[134] X. Yu, S. Zhang, L. Wang, Q. Jiang, S. Li, and Z. Tao. Hydrogen production from steam reforming of kerosene over Ni-La and Ni-La-K/cordierite catalysts. *Fuel*, 85:1708–1713, 2006. 119

[135] A.R. Choudhuria and S.R. Gollahalli. Characteristics of hydrogen-hydrocarbon composite fuel turbulent jet flames. *International Journal of Hydrogen Energy*, 28:445–454, 2003. 123

[136] F. Halter, C. Chauveau, and I. Gökalp. Characterization of the effects of hydrogen addition in premixed methane/air flames. *International Journal of Hydrogen Energy*, 32:2585–2592, 2007. 123